

MIE UNIVERSITY
Doctor of Engineering

Load and Power Control of Horizontal Axis Wind Turbine

Le Quang SANG

March, 2018

TABLE OF CONTENTS

Chapter 1 Introduction	1
1.1 Development of Wind Energy in the World	1
1.1.1 Historical uses of wind energy.....	1
1.1.2 Wind electric generation.....	1
1.1.3 Current status and future trend of wind power.....	2
1.2 Wind Power in Japan	3
1.2.1 Current status of wind energy.....	3
1.2.2 Development trend of wind energy.....	3
1.3 Wind Turbine Technology	4
1.3.1 Vertical axis wind turbine.....	4
1.3.2 Horizontal axis wind turbine.....	4
1.4 Previous Studies of Control Method of Horizontal Axis Wind Turbine	5
1.5 Research Purpose of Thesis	6
Chapter 2 Nomenclature	15
Chapter 3 Control of Wind Turbine	17
3.1 Review Load of Wind Turbine	17
3.2 Explanations of Blade Pitch Angle and Attack Angle	17
3.3 Cyclic Pitch Control Method	18
3.4 QBlade Software	18
3.5 FAST Simulation Capability	19
Chapter 4 Effect of turbulence intensity on performance of HAWT	25
4.1 Experimental Apparatus	25
4.1.1 Wind tunnel.....	25
4.1.2 Active turbulence grid.....	25
4.2 Experimental Methods	26
4.2.1 Experimental conditions.....	26
4.2.2 Sectional performance of the test blade.....	26
4.3 Results of Experiment and Simulation	27
4.3.1 Lift and drag coefficients.....	27
4.3.2 Power and thrust coefficients.....	28
Chapter 5 Load fluctuation on HAWT for extreme wind direction change	40
5.1 Experimental Apparatus and Conditions	40
5.1.1 Wind tunnel and model wind turbine.....	40
5.1.2 Sudden wind direction change equipment.....	40
5.1.3 Experimental conditions.....	40
5.2 Experimental Results	41
5.2.1 Extreme wind direction change simulation.....	41
5.2.2 Wind turbine performance in steady wind.....	42
5.2.3 Load measurement of two-bladed and three-bladed wind turbines.....	42
Chapter 6 Investigation of cyclic pitch control on HAWT	54
6.1 Experimental Apparatus and Conditions	54
6.1.1 Wind tunnel and model wind turbine.....	54
6.1.2 Model wind turbine.....	54
6.1.3 Swash plate and pitch control actuator.....	54
6.1.4 Experimental conditions.....	55

6.2 Rotor Aerodynamic Load and Performance Characteristics for Front Inflow Wind.....	55
6.2.1 Steady pitch control.....	55
6.2.2 Cyclic pitch control.....	56
6.3 Rotor Aerodynamic Load and Performance Characteristics for Yawed Inflow Wind.....	58
6.3.1 Yawed inflow wind condition.....	58
6.3.2 Steady pitch control.....	60
6.3.3 Cyclic pitch control.....	60
Chapter 7 Simulation results.....	92
7.1 Input and Output Data of FAST Code.....	92
7.2 Simulation Results and Experimental Data.....	93
Chapter 8 Conclusions.....	106
Acknowledgments.....	108
References	109

Chapter 1 Introduction

1.1 Development of Wind Energy in the World

1.1.1 Historical uses of wind energy

Human do the many efforts to harness the wind power for their life from the ancient times. For example, they used sails to propel ships and boats. Later, the wind power was used as the mechanical power to pump water or to grind grain. The wind power technology supported various phases of human society.

The windmills were used by the Persians for grinding grain during 200 B.C. Those windmills were vertical axis machines which the blades were made from reeds or wood. The windmills had grinding stones which was connected to the output shaft. The blades were connected to the horizontal arm. The size of the blades was about length of 5 m and height of 9 m [1]. The windmills for grinding were popular in most of Europe on the 13th century. As opposed to the vertical axis windmill, the windmills of the European were horizontal axis type, for example in England around 1150, in Germany in 1222 and in Denmark in 1259 [2]. In order to improve efficiency of the windmill, the rotor direction was automatically controlled by the tail. In addition, when the wind speed is high, the windmill was protected to avoid damage by adjusting the rotor direction out of the wind direction.

The designer Jan Adriaenszoon (the Dutch) was one of the first persons for designing the windmills in Europe. His windmill had some advantage in efficiency. Specifically, the rotor efficiency is increased by improving the crude airfoil profile. In the middle of 1700s, these windmills were installed in America by Dutch settlers.

The other successful application of the windmills is water pumping purpose. In the middle of 1800s, the multi-bladed windmills were built by America for this purpose. The rotor radius of these windmills are from one to several meters. In that time, the metallic blades and engineering design were applied to those water pumping windmills, so they increased the performance of the windmills. These American windmills could be automatically controlled. It means that the windmills can be itself controlled the rotor following the main wind direction.

1.1.2 Wind electric generation

In 1890, the first modern wind turbine for electric generation was installed in Denmark. This wind turbine generated direct current for hydrogen gas storage and electrolysis. Also in 1890, there is an electric generating wind turbine with rotor diameter of 17 m (144 blades) was installed in Cleveland, Ohio [1]. This wind turbine had capacity 12 kW and generated electricity for 20 years.

In early 1900s, the engineering design of wind turbine was improved such as the low-solidity rotors and aerodynamically designed blades. Therefore, the performance of wind turbine was increased significantly. Due to the wind turbine performance improvement, several hundreds of the electric generating wind turbines were constructed to supply power to the villages in Denmark in 1910. Two-bladed or three-bladed wind turbines (with capacity from 0.2 to 3 kW) were built for charging batteries. In addition, in America, the wind turbines generating electric became commercialization in 1925.

Palmer C. Putman developed a large-scale wind turbine with capacity of 1250 kW. The wind turbine was constructed in Belgium in 1941 [3]. It had a rotor diameter of 53 m and was mounted on a tower with height of 34m. This wind turbine could control rotor speed by adjusting the blade pitch.

In 1920, Darrieus G.J.M. (a French engineer) introduced a design of Darrieus wind turbine [4]. The Darrieus wind turbines were vertical axis types and they had narrow curved blades. The issues about high tip speed ratio and low solidity were presented in 1950's.

In the later years, the wind energy was still studied and developed such as the vortex turbine, diffuser augmented design, Musgrove rotor. Several wind turbine models were built and tested for the research purpose. However, a little wind turbine model design shows success commercial.

1.1.3 Current status and future trend of wind power

The total wind power capacity has installed about 55 GW in 2016, increasing total global wind power capacity about 12% to nearly 487 GW. This addition was the second largest high in period 2006-2016 as shown in Fig. 1.1. In the end of 2016, there are over 90 countries that had seen commercial wind power market.

China installed 23.4 GW in 2016 as shown in Fig. 1.2, this is to increase the total installed wind power capacity of China approximating 169 GW, and it occupied one-third of total global capacity by the end of 2016. The United States was second for added capacities of 8.2 GW, the total installed wind power capacity of 82.1 GW and the wind power generation of 226.5 TWh during in 2016 [5]. Canada supplemented 0.7 GW, the total capacity of 11.9 GW [6]. In 2016, the wind energy section of Canada developed slower than in 2014 and 2015, but it was Canada's largest source to generate electricity [7]. Moreover, in 2008-2016, the Asia region is the largest capacities and the Pacific region is the smallest capacities as exhibited in Fig. 1.3.

The EU added nearly 12.5 GW of total capacity (12 GW net), this is 3% lower than the record high in 2015. The installed onshore wind energy were 11% up and about 50% down offshore wind energy. The total capacity in the end of year obtained 153.7 GW (about 92% onshore and 8% offshore wind energy) [8]. Germany was the largest European market, with increasing operating wind power capacity by 5 GW for a total capacity of 49.5 GW (about 45.4 GW onshore and 4.2 GW offshore wind energy) [9].

In recent years, many countries started developing wind energy such as in Asia, Africa, Latin America and the Middle East. Bolivia and Georgia constructed their first wind plants in 2016 [10]. For the eighth continuous year, Asia where was the largest developed wind energy section, exhibiting about half of added wind power capacity, with Europe and North America appropriating for most of the rest [11]. Specifically, China installed 23.4 GW in 2016, and increasing total capacity of 169 GW, and appropriated for one-third of the total global capacity in the end of year [12]. In the end of 2016, India added 3.6 GW and the total capacity was 28.7 GW, becoming up its fourth-place position for the total installed capacity in the world [13]. By late 2016, there is significant additional capacity in the Asia region, for example, Indonesia had the first utility-scale wind farm, and Vietnam had also other wind farms with capacity of 0.940 GW [14, 15]. For offshore wind energy, the installed capacity was about 2.2 GW connected to grids in 2016, and the total installed capacity in the world obtained 14.4 GW as described in Fig. 1.4.

In 2016, the levelized cost of electricity (LCOE) of the wind power continued to fall because of following reasons, the wind turbines were standardized, the size of blades and tower increased, efficiency and capacity factors of wind turbine increased much more. Therefore, many manufacturers completed for producing larger wind turbines during 2016 with several companies such as Enercon, GE, Nordex and Senvion for the onshore wind turbines, and Siemens and MHI Vestas for the offshore wind turbines. In addition, the capacity ratings also increased in 2016: the average size turbine delivered to market was up 6.4% over 2015, to 2.16 MW. By region, the average wind turbine sizes were installed in the Middle East and the Commonwealth of Independent States of 2.8 MW, followed by Europe's wind turbine of 2.7 MW, Latin America's of 2.3 MW, North America's of 2.2 MW, and Africa and Oceania's both below 2 MW. Wind turbine capacity in the 2-2.5 MW size range occupied about nearly two-thirds of wind turbine types in the world in 2016 [16].

For scale of the offshore wind power projects, it is important to reduce costs by scale and standardization. The wind turbine has increased size as well as scale of projects. The average capacity of new constructed wind turbines in Europe constructed in offshore was 4.8 MW. This capacity is 15% higher than the offshore wind turbines in 2015 and 62% larger than a decade ago. The average size of wind turbines required in the middle of 2016 was 7.7 MW [17]. In the end of 2016, the first wind turbine of 8 MW was installed offshore and grid-connected. In addition, some companies had also wind turbine of 8 MW such as Vestas, Siemens, GE and Adwen [18]. In early 2017, MHI Vestas Offshore Wind has up-rated wind turbine of 8 MW to 9 MW; the wind turbine's swept area is larger than the Ferris wheel of the London Eye [19].

1.2 Wind Power in Japan

1.2.1 Current status of wind energy

In 2015, the share of renewable energy power generation of Japan has increased to 14.5% over 2011. Because Fukushima nuclear power plant was accident in 2011, the nuclear power generation rapidly decreased to almost zero. Therefore, the renewable energy was developed to compensate that deficit. In the renewable energy power generation, the large hydro is the largest share of 7.1%, the solar energy has second share of 3.3%, the small share of 0.5% of wind power in Japan as shown in Fig. 1.5 [20].

Japan has very good wind power potential examined by the Ministry of the Environment (MOE-2011) [20] and the wind energy resources are concentrated in Hokkaido, Tohoku, and Kyushu regions [21]. Specifically, for onshore wind energy, the total of the wind energy potential is over 1,500 GW with the wind speed of 5.5 m/s. With the good wind speed is over 7.0 m/s, the energy potential is about 508 GW. For the offshore wind energy (the depth < 50 m), the wind energy potential is about 368.35 GW with the wind speed of 6.5 m/s. For the offshore wind energy (the depth from 50 m to 200 m), the wind energy potential is about 1,376.62 GW with the same wind speed of the offshore wind near coast. The detail of the wind energy potential is exhibited in Table 1.1 and Fig. 1.6.

For the onshore wind energy, Japan has installed 3.17 GW. For the offshore wind energy, in Japan has 0.06 GW in February, 2017. The offshore wind energy equals about 1.8% of total installed wind power in Japan. These offshore wind power projects (about 0.044 GW, 23 turbines) are commercial or local government owned projects [22]. These projects are closed to seashore and the offshore wind turbine foundations are dolphin type or mono-pile type. For the offshore projects which distance is more than 1km from seashore are national projects. Example, 2 floating wind turbines with capacities of 9 MW were installed by METI in Fukushima. The 5 MW advanced spar floating type has started official operation in March, 2017.

Japanese Government has an attractive feed in tariff (FIT) price for renewables since 2012. Example, for onshore wind energy, the FIT price is 22 JPY/kWh, the FIT price of the offshore wind energy is 36 JPY/kWh [22]. However, there are some obstacles in wind power field in Japan and divided into 2 terms: short term and middle term.

- In the short term, all wind farms over 10 MW have applied the Environment Impact Assessment (EIA) procedures since Oct. 2012. This EIA process needs about 4 years to complete, and this is long time to develop wind farm projects. In addition, many wind farm projects (about 82 projects of 5.2 GW) in the EIA process now.

- In the middle term, grid limitation is one of the reasons which restricted the wind power development. Japanese electric power systems is controlled by 9 companies (9 regions) and the electric transmission between these regions is difficult issue.

There are some ways to improve wind power field in Japan, for example, improve electric grid operation such as inter-regional grid operation for wind power collection, build new local grid lines at the northern rural area and sophisticated wind power output prediction system. In addition, the wind farm operation is also improved such as the wind farm power output control and power fluctuation reduction by using battery system.

1.2.2 Development trend of wind energy

According to Japan Wind Power Association, there are 5 issues for wind power field in Japan including reduce the levelized cost of electricity (LCOE), improve power grid infrastructure, promote repowering, develop offshore wind and establish domestic supply chain [22].

Fig. 1.7 shows the trend of wind power generation cost of Japan up to 2030. The expected electric generation cost is 8-9 JPY/kWh toward 2030. For onshore wind power, the Kyushu area has to accelerate at first because it has some margin. And next is the Hokkaido & Tohoku areas. Furthermore, the offshore wind power development is a good selection, but it needs attempts to remove the barrier such as the long-time of EIA process, electric grid system and law modification for general common sea area. The offshore wind power development areas are built as shown in Fig. 1.8. The schedule for expansion of offshore wind power up to 2030 is described in Fig. 1.9.

1.3 Wind Turbine Technology

For the wind turbine technology, several wind turbine type and shapes were designed and developed in the world. Some of specific designs were introduced to research experiment. There are several ways to categorize wind turbines such as axis type and/or power capacity. In this section, they are generally divided into horizontal axis machines and vertical axis machines. In addition, the horizontal axis machines are classified to upwind and downwind wind turbine.

1.3.1 Vertical axis wind turbine

The vertical axis wind turbine (VAWT) is shown in Fig. 1.10. The rotor of the VAWT rotates around a vertical axis. For the urban area, the generator set top of tower and near the ground, so the operation and maintenance of VAWT are easier than the HAWT. The VAWT can be used in low wind speed and city areas.

The advantages of the VAWT are:

- 1) The tower of VAWT may not need supporting the generator and gearbox.
- 2) The VAWT do not need a yaw mechanism to follow wind direction.

The disadvantages of the VAWT are:

- 1) Wind speed closes to the ground so it is low and high turbulence. The wind speed on the lower part of VAWT rotor is very low.
- 2) The general efficiency of the VAWT is low.
- 3) The VAWT is not self-starting, but it can use the generator as a motor to start.

1.3.2 Horizontal axis wind turbine

Almost all of the commercial wind turbines today are horizontal axis wind turbines (HAWT). The HAWT rotor rotates around horizontal axis which is almost parallel to the ground and the wind direction as shown in Fig. 1.11. The blades are assembled perpendicularly to the rotating axis. The most popular blade number of the HAWT usually is three. Some HAWT has 1 blade or 2 blade and so on, depending on the purpose.

The advantages of HAWT are:

- 1) The HAWT has a tall tower, so it can receive high wind speed.
- 2) The HAWT has high output capacity and high aerodynamic efficiency.
- 3) The blades of HAWT has twist angle, so the blades can obtain the best angle of attack.

The disadvantages of HAWT are:

- 1) There is a yaw control system on the HAWT to turn the rotor blades following the wind.
- 2) The HAWT is difficult to transport and install because of its weight compared with the VAWT.
- 3) The HAWT is difficult maintenance because of nacelle is installed on the top of high tower.

In addition, depending on the wind direction into the rotor plane, the HAWT is divided into upwind and downwind wind turbines as shown in Fig. 1.12.

1.3.2.1 Upwind wind turbine

An upwind wind turbine type which faces into the wind has the rotor blades rotate upstream of the nacelle and tower. The rotor blades of the upwind wind turbine usually stiffer because the wind force impacts on the rotor blades toward the tower. Therefore, the blades of the upwind wind turbines will be increase the rotor weight and the load applied to the wind turbine. Furthermore, the upwind wind turbines need a yaw control system to turn the rotor following the wind.

The upwind wind turbine type is the most popular in the world. The major advantage of this type is much less the tower shadow effect, so it can reduce dynamic loads on the rotor blades. However, this is also a disadvantage of the upwind wind turbine, the distance between the rotor blades and tower must be wide enough to avoid risk of the rotor blades and tower. Therefore, the prediction of blade vibration under complex turbulent wind conditions has to accuracy to avoid damage of rotor blades and tower.

The distance between the rotor blades and the tower is increased by tilting the low-speed shaft upwards or by raising the rotor overhang. In fact, the rotor overhang was kept the small distance from rotor blade to minimize low-speed shaft to reduce cost of wind turbine. Therefore, the low-speed shaft is tilted upwards about 5° or 6° to ensure the distance of the blades and tower.

1.3.2.2 Downwind wind turbine

A downwind wind turbine type has the rotor blades rotate downstream of the nacelle and tower. If the rotor blades and nacelle is designed suitably, the downwind does not need the yaw control system. The rotor of downwind turbine is operated the turbulent wind produced by the velocity deficit of the tower shadow. A significant advantage of the downwind wind turbine is light rotor. The downwind turbine can accept the large displacement of blade tip without the risk of tower strike. So the blade can reduce the stiffness and weight. The blade bending-moments can be reduced by the centrifugal forces. Because the rotor blades rotate generating a cone shape, so the moments by the centrifugal force act as counteracting moments by the thrust.

From the other point of view, the tower wake effect is the disadvantage of the downwind wind turbine. As the rotor passes through the tower shadow, the fatigue load fluctuation on the turbine is higher. The performance of wind turbine decreases because of lower wind speed. A noise is also higher due to the wake.

1.4 Previous Studies of Control Method of Horizontal Axis Wind Turbine

Wind turbines are operated in the natural wind with many complex conditions such as the wind speed fluctuation, gust wind and turbulence wind. It is important to understand the interaction between this complex wind and wind turbines. The turbulent wind has significant impact on load and performance of the wind turbine.

To reduce the cost of wind energy, the wind turbines are designed with larger dimensions and rated power, so the structural loads are also increased. Furthermore, the floating offshore wind turbine has complex motion by the aerodynamic forces of the wind and the hydrodynamic forces of the waves. Therefore, it is necessary to decrease loads and increase power coefficient for the offshore wind turbines.

The wind turbine control focus on the maximum energy production, safe operation and minimum operation and maintenance costs. In addition, in order to control wind turbine exactly, the control method is based on the operating regime of the wind turbine. Specifically, the wind speed is less than the rated, the control method efforts to product maximum energy. On the other hand, the wind speed is more than the rated, the control keeps the rated power and protecting wind turbine. To keep the rated power, the pitch-regulated or stall-regulated wind turbines are controlled by the wind speed and the other input signal. The wind turbine control methods are divided into 4 types:

- For the passive-stall control: The main feature of this control method is a special blade design. It provides a stall effect to protect wind turbine and to limit the power.
- For the active-stall control: The blades are turned follow the stall to decrease the aerodynamic power. The pitch angle is negative.
- For the passive-pitch control: The self-operated controllers modify the blade pitch angle at the higher wind speed.
- For the active-pitch control: The key feature is a power limitation by adjusting the pitch angle.

For each the control method, many previous researches have been studied to experiment and practice into the wind turbine. Many control methods were performed by simulation algorithms, controllers and wind tunnel experiments to increase power generation and decrease load of wind turbine.

For increasing power generation, maximizing the power capture from the wind is one of the main tasks in the design of the wind turbine control system. Boukhezzar et al. [23] proposed a non-linear approach to control a variable-speed turbine to maximize power in the presence of generator torque considerations. Munteanu et al. [24] applied a linear-quadratic stochastic approach to solve the power optimization model, and tested it using an electromechanical wind turbine simulator. A trade-off between the efficiency of energy conversion and input variability was studied in the simulation experiments. Muljadi and Butterfield [25] developed a pitch control strategy to maximize power and minimize turbine loads for different wind speed scenarios. Bossanyi [26] reviewed

some recent developments in control algorithms for pitch control and generator torque control for variable speed turbines. He discussed that in addition to improving the control design, it is also possible to add some additional sensors to achieve its objectives effectively. These additional actuators are implementing individual pitch controllers for each blade and then control performance can be improved by making trade-off between energy capture and loads.

In addition, to reduce these asymmetric loads, active load-reduction methodologies can be applied. Bottasso et al. showed that the cyclic pitching of the blades induced a reduction of the average loading of a wind turbine, at least for some components such as the main bearing, the yaw bearing, or the tower [27]. Houtzager studied and developed individually pitch-controlled blades by proposing a lifted repetitive controller that can reject these periodic load disturbances for modern fixed-speed wind turbines and modern variable-speed wind turbines operating above-rated [28]. Furthermore, Menon and Ponta focused on the use of rapid pitch control for handling short-term variations in wind conditions and load fluctuations within one cycle of rotation, with special attention to the prognosis of the aeroelastic response of the rotor [29]. Van Solingen et al. used linear individual pitch control method to significantly reduce the wind turbine loads for both below-rated and above-rated operation [30]. The wind tunnel tests performed by Velte et al. [31] also showed that in some cases the maximum load reduction could be large by properly controlling the trailing edge. Bottasso et al. [32] introduced passive control method using aeroelastic devices.

A control method is to use a technology originally known from helicopter control, cyclic pitch control, and later adapted to wind turbine control as reported in [33-35]. This type of regulator is based on the local blade load measurement, which is well-known as state-of-the-art technology. In the last decade, the ability of cyclic pitch control systems to lower fatigue loading on wind turbines has been thoroughly investigated and quantified of literature devoted to this subject [36-38]. Traditionally, the cyclic pitch control is used for the three-bladed turbines to reduce the blade loads by varying the 1P sinusoidal pitch angle of 120° between each blade.

1.5 Research Purpose of Thesis

There are three types of loads acting on wind turbine such as steady aerodynamic loads, cyclic aerodynamic loads and random aerodynamic loads. The load fluctuation decreases the wind turbine performance and their life. Therefore, the control of wind turbines is a task with multiple objectives as load reduction, power production increase and reliable operation. The main purpose of this thesis is to develop a control method to reduce load of rotor blade for steady wind condition in the ocean. The cyclic pitch control method is used to moderate the effect of fluid force generated on rotor blade of the HAWT. The HAWT is assumed that installed in the ocean. Floating offshore wind turbines (FOWTs) are sensitive to oscillations due to the aerodynamic force of the wind and the hydrodynamic force of the wave. These factors may have undesirable effects on the performance and structural stability of FOWTs.

The originality of the cyclic pitch control used to research for the offshore wind turbine. Because the offshore wind turbine load is effected by the wind and wave forces on wind turbine. Therefore, this control method need apply to decrease load fluctuation of offshore wind turbine. The previous study focused on onshore wind turbine and there is not yet particular estimation about it [39].

In this research, in order to efficiently suppress the movement of the floating offshore wind turbine, the construction of a control method of fluid force generated on the rotor plane is aimed during wind turbine operation. The movement of the floating platform due to external force such as wind and wave is considered. They include swaying in the pitch direction oscillating in the main flow direction around the center of gravity and yawing motion in the yaw direction rotating around the vertical axis from the water surface. For the fluid force control, two control methods called "steady pitch control" and "cyclic pitch control" were used.

Steady pitch control is a control method in which the pitch angle is constant at all azimuth angle positions. With this control method, it is possible to actively change the magnitude of the fluid force acting on the rotor plane, and the magnitude of the thrust can be changed. Cyclic pitch control is a control method that periodically changes the pitch angle depending on azimuth angle position. With this control method, the different fluid forces can be generated depending on azimuth angle position, and the magnitude and direction of the moment acting on the rotor

plane can be changed. In this research, the force and moment acting on the rotor plane in steady pitch and cyclic pitch controls are considered.

A pitch angle control in a general wind turbine is performed by a motor installed inside the hub. Therefore, when performing cyclic pitch control, an excessive load is generated on the pitch angle changing motor. Therefore, in this research, to facilitate the cyclic pitch control method, the cyclic pitch angle adjustment was performed by using swash plate. The swash plate is described in detail in the next chapter. In principle, this method can also be used for real wind turbines. The existing wind turbine design concepts for controlling the individual rotor blades independently, by introducing the swash plate, there is a possibility of constructing a wind turbine can be more easily the cyclic pitch control. In this study, a wind tunnel experiment used the test wind turbine with the pitch control mechanism according to the swash plate. In order to measure the fluid force generated in the rotor plane, the six-component balance was used. In the cyclic pitch control test, the magnitude of the amplitude of the pitch angle fluctuation was considered. The relationship between the phase and the moment axis direction generated on the rotor plane is investigated. In addition, simulation analysis was performed by the aerodynamic elastic analysis code FAST. And then, the simulation results were compared with experimental values to verify the validity of numerical analysis.

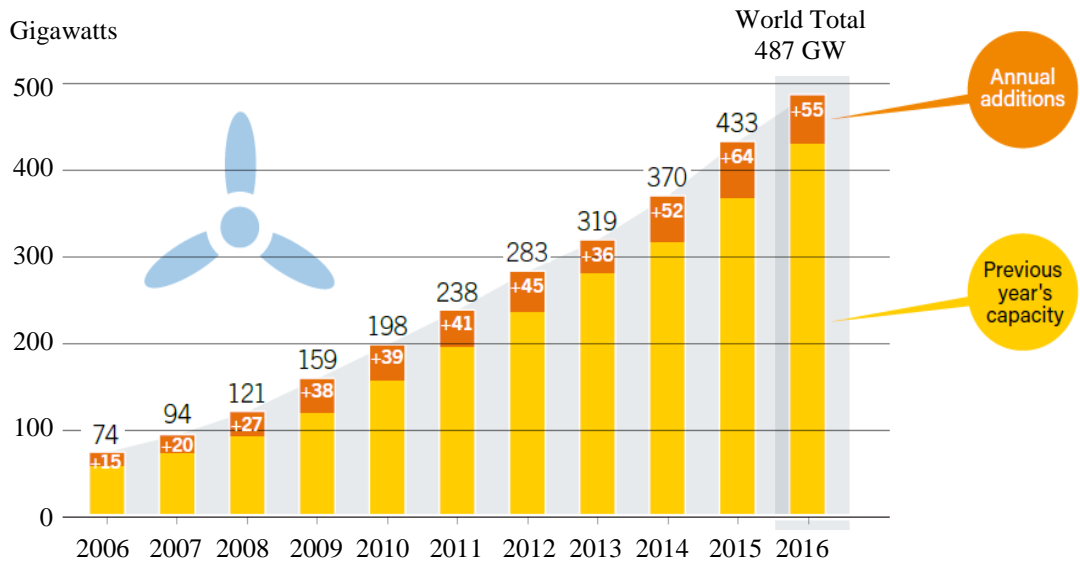


Fig. 1.1 Wind power global capacity and annual additions, 2006-2016
 (Source: http://www.ren21.net/wp-content/uploads/2017/06/17-8399_GSR_2017_Full_Report_0621_Opt.pdf)

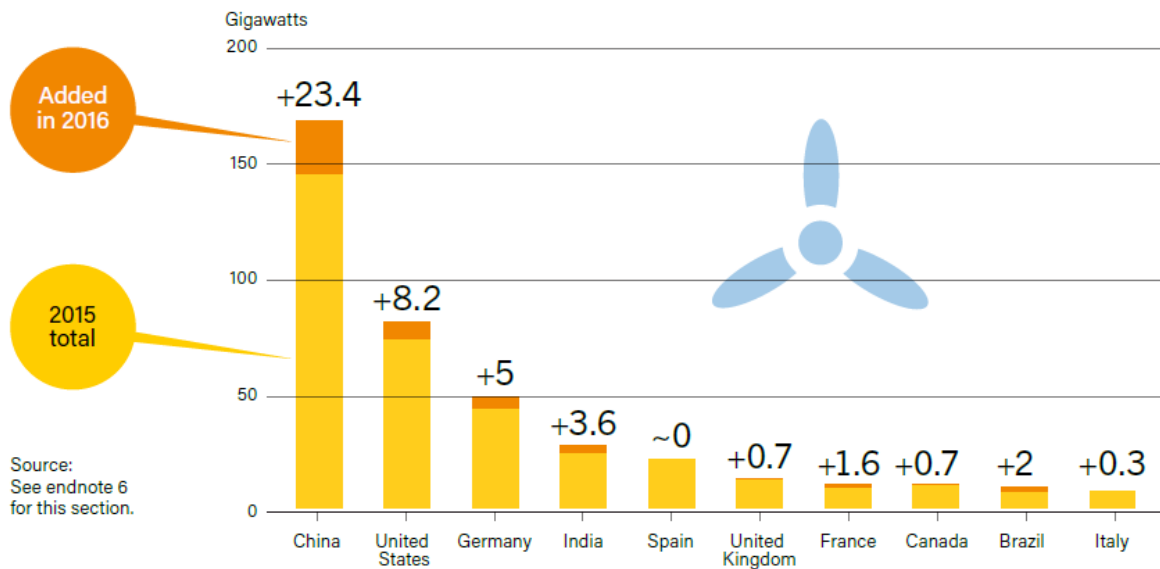


Fig. 1.2 Wind power capacity and additions, Top 10 countries, 2016
 (Source: http://www.ren21.net/wp-content/uploads/2017/06/17-8399_GSR_2017_Full_Report_0621_Opt.pdf)

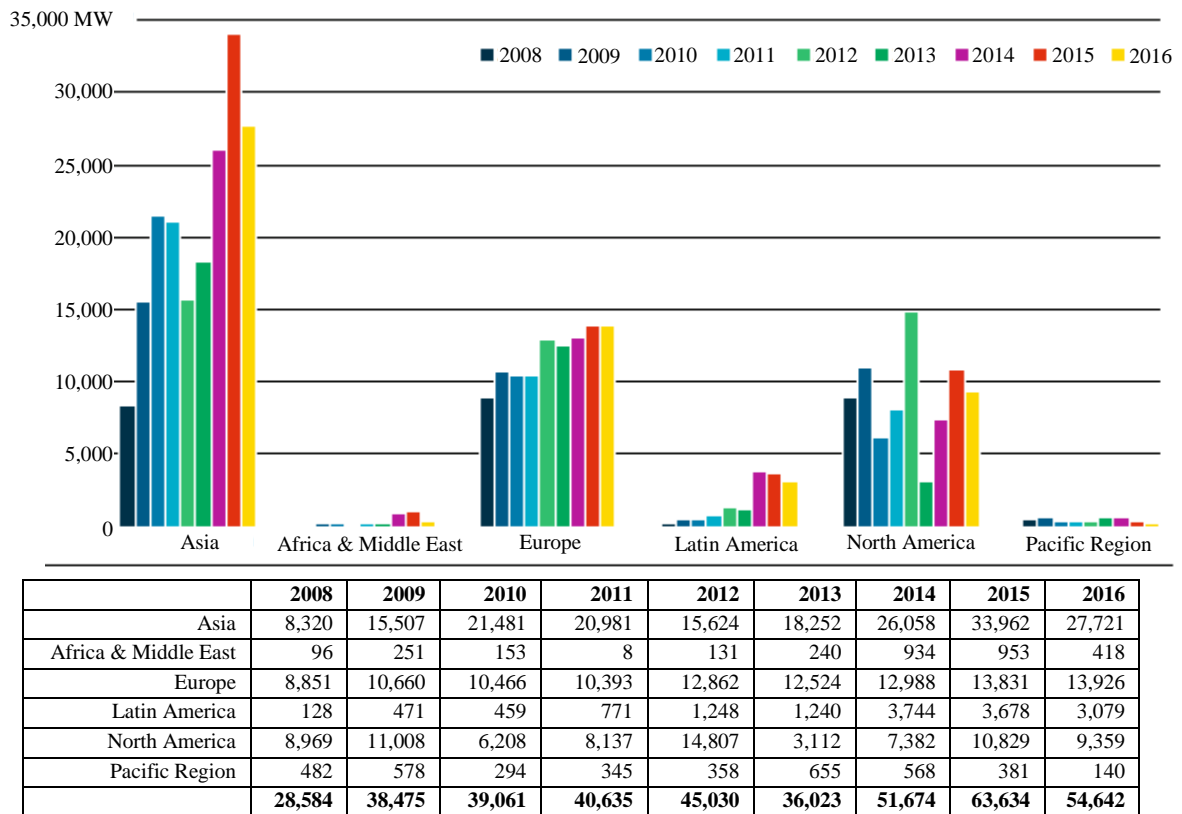


Fig. 1.3 Annual installed capacity by region 2008-2016
(Source: Global wind report annual market update 2016)

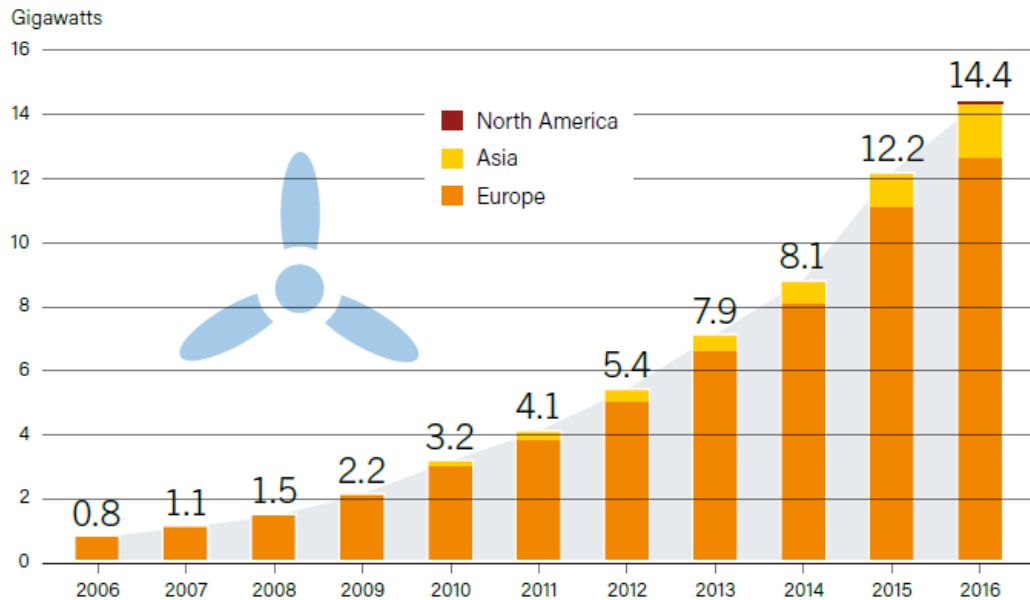


Fig. 1.4 Wind power offshore global capacity, by region, 2006-2016
(Source: http://www.ren21.net/wp-content/uploads/2017/06/17-8399_GSR_2017_Full_Report_0621_Opt.pdf)

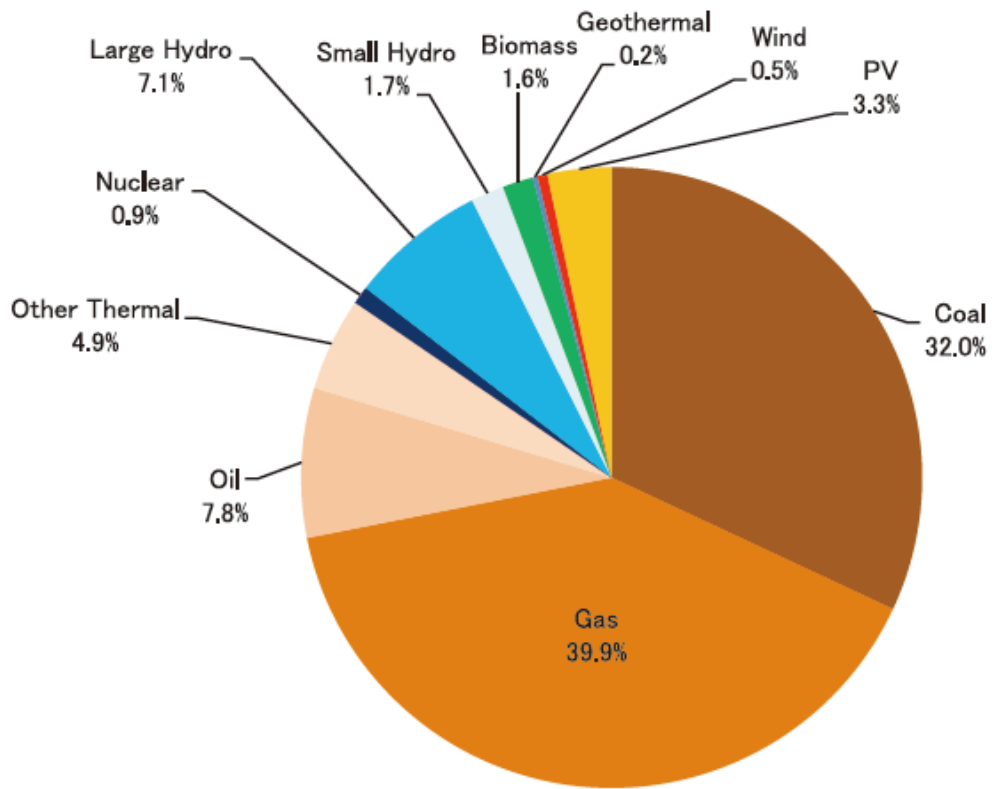


Fig. 1.5 Renewable energy power generation in Japan in the year 2015
 (Source: <http://www.iseip.or.jp/en/wp/wp-content/uploads/2016/10/JSR2016Summary-EN.pdf>)

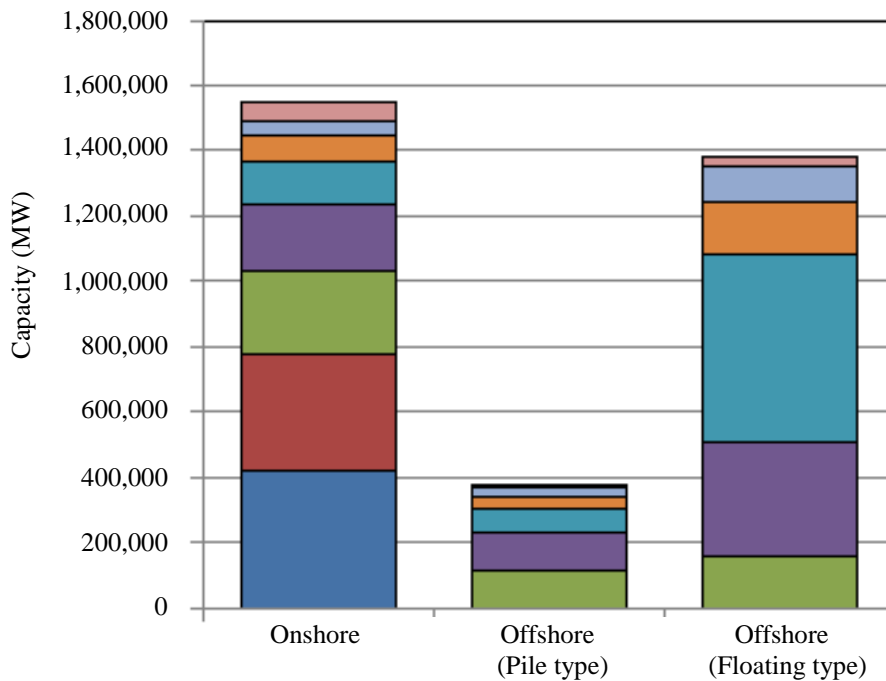


Fig. 1.6 Wind power offshore capacity of Japan by region, 2006-2016
 (Source: http://www.meti.go.jp/meti_lib/report/2011fy/E001771.pdf)

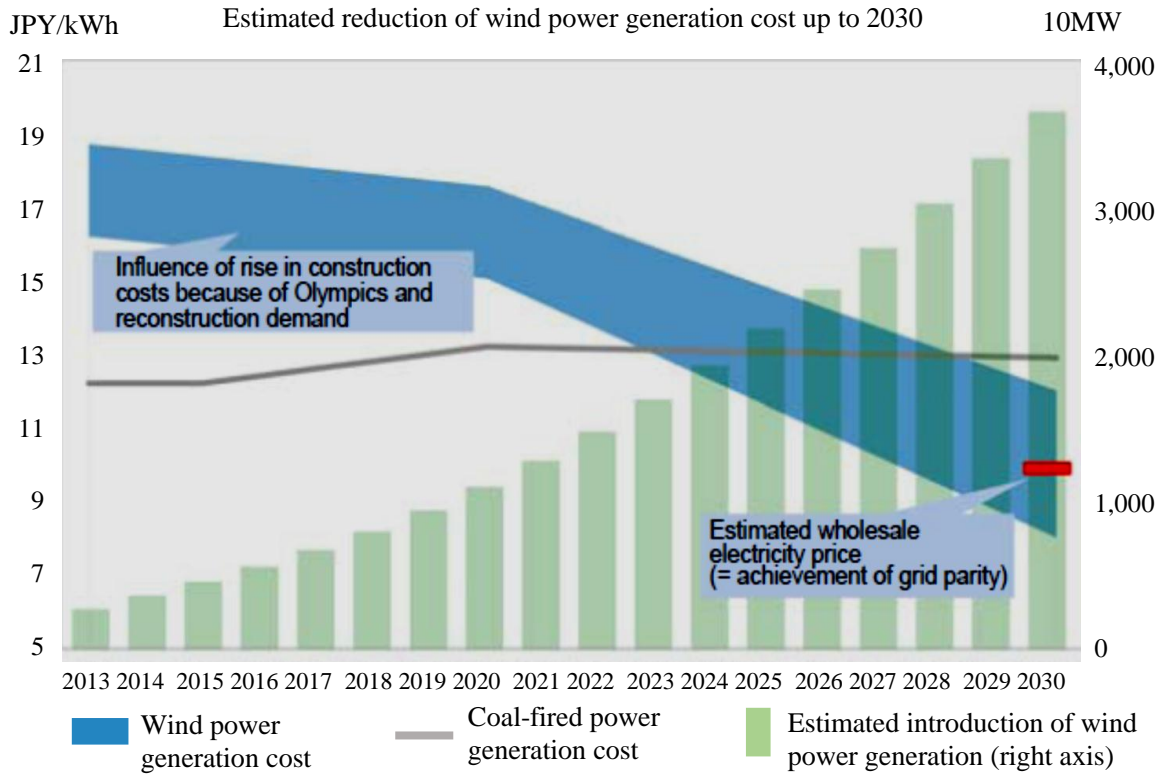


Fig. 1.7 Trend of wind power generation cost of Japan up to 2030
 (Source: http://jwpa.jp/pdf/JWPA_REvision2017_ExpertMTG.pdf)

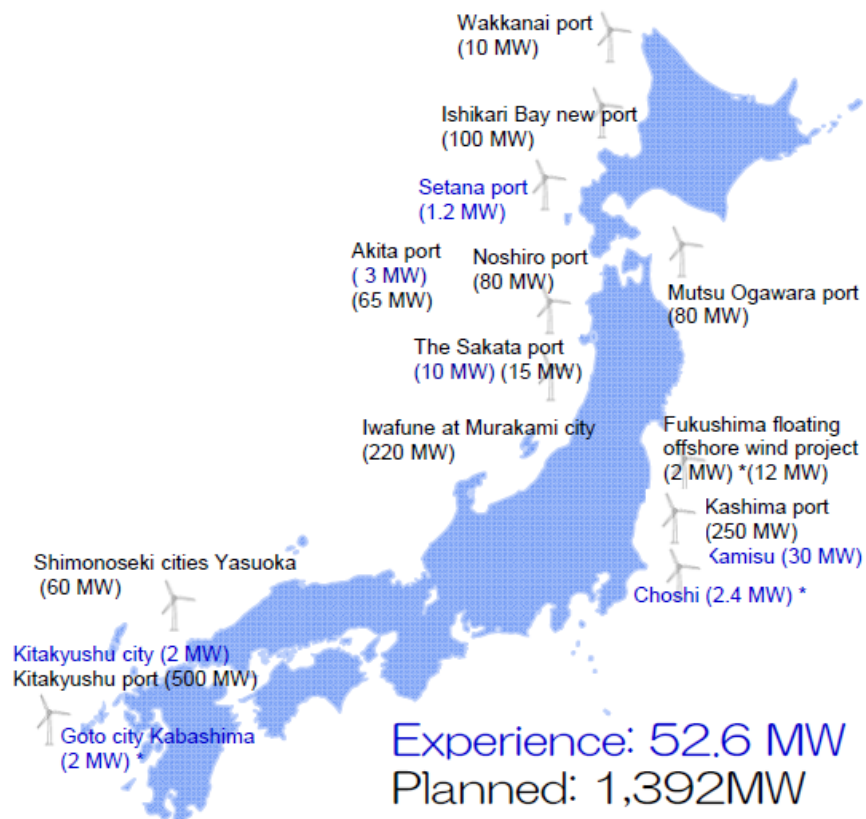


Fig. 1.8 The offshore wind power development in Japan
 (Source: http://jwpa.jp/pdf/JWPA_REvision2017_ExpertMTG.pdf)

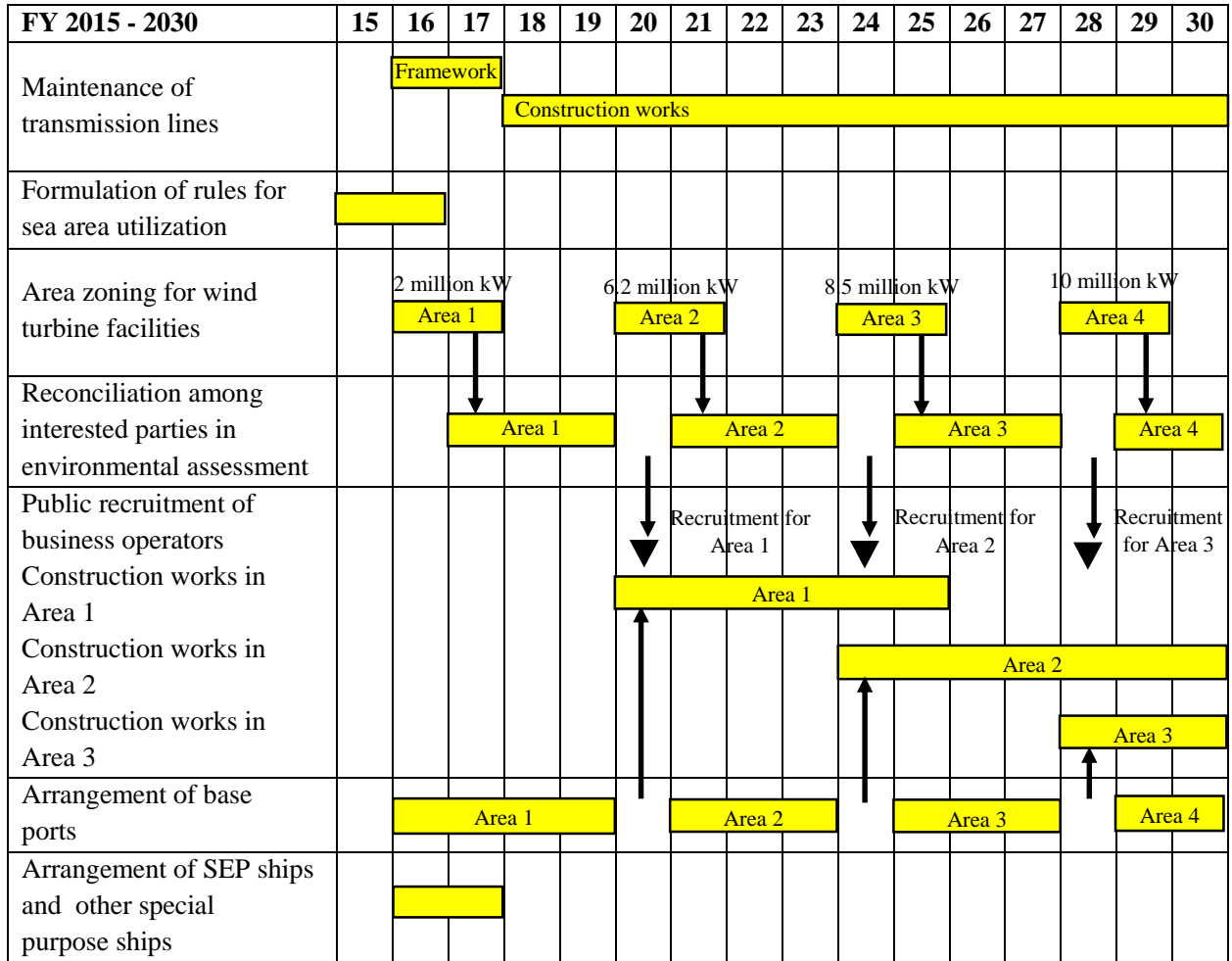


Fig. 1.9 Schedule for expansion of offshore wind power introduction in Japan
 (Source: JWPA, http://jwpa.jp/pdf/JWPA_REvision2017_ExpertMTG.pdf)



Fig. 1.10 Vertical axis wind turbine (VAWT)



Fig. 1.11 Horizontal axis wind turbines (HAWT)

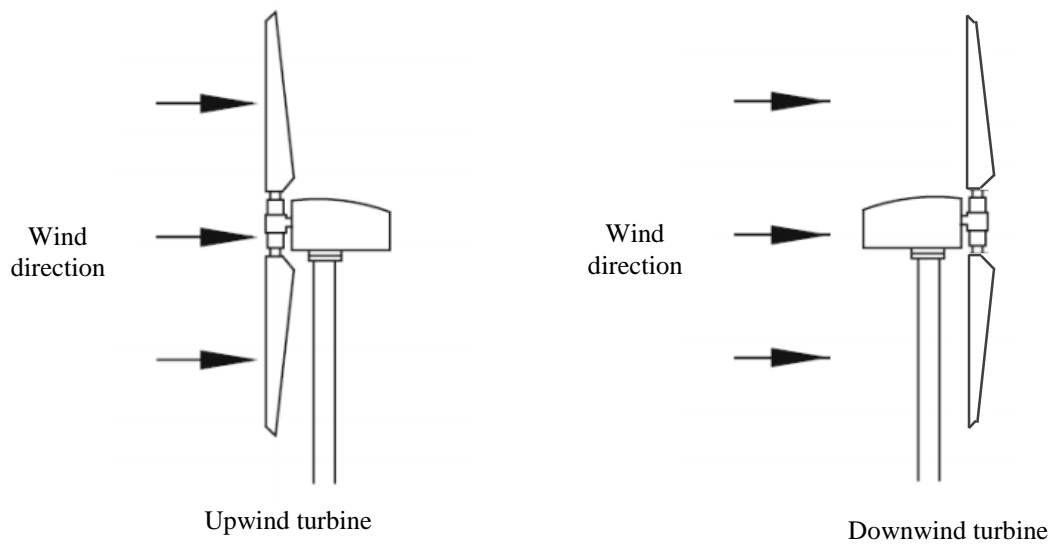


Fig. 1.12 Upwind turbine and Downwind turbine

Table 1.1 Wind energy potential of Japan
 (Source: http://www.meti.go.jp/meti_lib/report/2011fy/E001771.pdf)

	Wind Speed (m/s)	Area (km ²)	Power (MW)	Generated electric energy (Billion kWh)
Onshore	5.5	154,619	1,546,190	36,945
	6.0	112,841	1,128,410	29,626
	6.5	77,528	775,280	22,201
	7.0	50,888	508,880	15,901
	7.5	31,817	318,170	10,722
	8.0	18,265	182,650	6,567
	8.5	10,326	103,260	3,924
	9.0	5,696	56,960	2,261
Offshore (Pile type)	6.5	36,835	368,350	10,305
	7.0	24,996	249,960	7,505
	7.5	13,632	136,320	4,419
	8.0	6,466	64,660	2,222
	8.5	2,397	23,970	867
	9.0	315	3,150	119
Offshore (Floating type)	6.5	137,662	1,376,620	41,065
	7.0	121,183	1,211,830	37,167
	7.5	87,289	872,890	27,963
	8.0	29,525	295,250	10,252
	8.5	13,675	136,750	4,977
	9.0	2,710	27,100	1,038

Chapter 2 Nomenclature

a	Pitch angle change amplitude [°]
A	Rotor swept area [m ²]
b	Averaged pitch angle [°]
c	Chord length [m]
C_L	Lift coefficient [-]
C_D	Drag coefficient [-]
C_{Mx}	Pitching moment coefficient
C_{Mx}'	Corrected pitching moment coefficient
C_{Mz}	Yawing moment coefficient
C_{Mz}'	Corrected yawing moment coefficient
C_P	Power coefficient
C_T	Thrust coefficient
f	Frequency [Hz]
F	Fluid force [N]
F_X	X-direction force measured by 6-component balance [N]
F_Y	Y-direction force measured by 6-component balance [N]
F_Z	Z-direction force measured by 6-component balance [N]
N	Rotor blade revolution [min ⁻¹]
M_X	X direction moment measured by 6-component balance (pitching moment) [Nm]
ΔM_X	Pitching moment amplitude [Nm]
M_Y	Y direction moment measured by 6-component balance [Nm]
M_Z	Z direction moment measured by 6-component balance (yawing moment) [Nm]
ΔM_Z	Yawing moment amplitude [Nm]
Q	Rotor torque [Nm]
r	Rotor radial position [m]
R	Rotor radius [m]
Re	Reynolds number
t	Reference trigger time [s]
Δt_{WDC}	Time period between trigger and the beginning of wind direction change [s]
T	Thrust acting on rotor plane [N]
TI	Turbulence intensity [%]
U	Mainstream wind speed [m/s]
U_a	Axial velocity component in rotor plane [m/s]
U_r	Horizontal velocity component in rotor plane [m/s]
U_{ref}	Relative inflow wind speed [m/s]
U_{rot}	Rotor blade velocity component [m/s]
U_{st}	Mainstream wind speed velocity [m/s]
U_v	Wind velocity at blade tip position [m/s]
w_i	Induced velocity [m/s]
Δx	Correction of X-direction load point of 6-component balance [m]
Δy	Correction of Y-direction load point of 6-component balance [m]

Δz Correction of Z-direction load point of the 6-component balance [m]

Greek symbols

α	Angle of attack [°]
α_L	Angle of attack at the high tip speed ratio [°]
α_S	Angle of attack at the low tip speed ratio [°]
ϕ	Geometrical inflow angle [°]
λ	Tip speed ratio
ν	Kinematic viscosity of air [m ² /s]
θ	Pitch angle [°]
ρ	Air density [kg/m ³]
ω	Rotor angular velocity
$\theta(\psi)$	Pitch angle with azimuth angle [°]
θ_{twist}	Rotor blade twist angle [°]
σ_A	Actuator position [mm]
σ_{SW}	Displacement of swash plate [mm]
ξ	Phase angle of pitch angle [°]
ψ	Azimuth angle [°]
ψ_M	Azimuth angle of moment [°]
φ	Yaw angle [°]

Chapter 3 Control of Wind Turbine

In order to understand the load reduction of the floating offshore wind turbine by the cyclic pitch control method, the oscillation forces of the wind turbine motion have been studied. The pitching moment and the yawing moment are selected to measure and analysis. The steady load and cyclic load are focused on this study. The fluid force which is effected by angle of attack, pitch angle and azimuth angle is also considered. This research shows the aerodynamic characteristics of the wind turbine's rotor which operated in steady pitch control and cyclic pitch control by a wind tunnel experiment. The experimental data is compared with simulation results by FAST code. Therefore, this chapter shows some fundamental definitions.

3.1 Review Load of Wind Turbine

As the modern wind turbines have large size, they have many components and large fatigue load of component may lead to their failure [40]. During on power production, they have various types of loads acting on the rotor blades and the wind turbine with different sources [41-43] such as steady loads, cyclic loads and random aerodynamic loads as shown in Fig. 3.1.

- Steady loads are generated by mean wind speed, centrifugal forces on the blades and weight of the wind turbine on tower. The stable aerodynamic loads contribute to the long-term power production.
- Cyclic loads are generated in some cases such as rotation of the rotor, tower shadow and wind shear. The cyclic load at blade root appears because of the gravitation force. When the wind turbine rotor blade passed from the tower then wind speed acting on rotor will be decelerated which is known as tower shadow. In addition, yaw misalignment will also cause cyclic load on the wind turbine and the rotor blades.
- Random fluctuation of the wind speed in time is understood as turbulence which is the main source of random aerodynamic loads. The wind speed which is called a gust wind increases suddenly (last from 3 to 20 second) and generates random loads on the blades of the wind turbine [44].

In this thesis, we focused on steady load and cyclic load of wind turbine. The analysis results will be discussed in following chapters.

3.2 Explanations of Blade Pitch Angle and Attack Angle

The pitch angle θ is defined as the angle formed between the chord line and the rotation plane of the wind turbine and the direction of the pitch angle in which the leading edge of the blade inclines to the upstream side is defined as positive as shown in Fig. 3.2. The azimuth angle of the rotor is defined to be positive in the wind turbine rotation direction. The yaw angle is defined as the angle formed by the wind turbine rotation axis and the main flow direction, and clockwise around the center axis of the tower is positive looking from the sky. And the angle between the chord line and the geometric inflow wind is defined as the angle of attack α as:

$$\alpha = \phi - \theta \quad (3.1)$$

where ϕ is geometrical inflow angle.

The local pitch angle θ , is defined by the averaged pitch angle of the blade and the twist angle along the blade span, θ_{twist} as:

$$\theta = \theta_{\text{pitch}} + \theta_{\text{twist}} \quad (3.2)$$

Fig. 3.2 also defines the angle of attack of the blade, the pitch angle, the geometrical inflow angle and the fluid force. This figure shows the fluid force acting on the blade element at the blade tip. The incoming wind speed is constant. U_{rot} is the rotational velocity of blade. The magnitude of the lift and the drag generated on the blade

element are determined by the angle of attack, and each direction is determined by the inflow angle flowing into the rotor plane.

3.3 Cyclic Pitch Control Method

In the last decade, the ability of cyclic pitch control system has been investigated to reduce load on wind turbines [45, 46]. Although, some main results obtained by the simulation or the experiment show that the cyclic pitch control is quite beneficial for decreasing load. The cyclic pitch control method can significantly reduce the average pitching and yawing moments due to the yaw misalignment. The cyclic pitch control can be seen as a preventative control method that stops the wind turbine, so that, if an extreme event happens, the wind turbine will stop with smaller loads.

The cyclic pitch is adjusted by a swash plate system as shown in Fig. 3.3. The swash plate consists of two disks, a non-rotating part and a rotating part, via a bearing. The disk of the non-rotating part is connected to the three pitch control actuators mounted on the nacelle via the rod. The disk of the rotating part is connected to the pitch lever and rotates with the rotor. The control points of the three actuators in the non-rotating part are the azimuth angles of $\psi = 0^\circ, 120^\circ$ and 240° .

Fig. 3.3 (a) indicates the mechanism of the swash plate. As shown in this figure, the positions of the three connection points in the non-rotating part of the swash plate are determined by controlling the positions of the three actuators. This determination depends on the distance and the inclination of the swash plate with the rotor face. Fig. 3.3 (b) and (c) describe the cross-sectional views of the parallel movement and the tilt movement of the swash plate, respectively. When the swash plate is moved in parallel to the rotor plane, the pitch angle is constant with any azimuth angle. As a result, the steady pitch control can be performed. When the swash plate is tilted with respect to the rotor plane, the distance between the rotor plane and the outer edge of the rotating part of the swash plate varies depending on the azimuth angle position. Due to the change of distance, it becomes possible to change the pitch angle with respect to the azimuth angle, and the cyclic pitch control is achieved. The pitch angle change in the cyclic pitch control is given by the following expression:

$$\theta(\psi) = a \cos(\psi - \xi) + b \quad (3.3)$$

Here, ψ is the azimuth angle, ξ is the phase angle of the pitch angle θ with respect to the azimuth angle ψ , a is the pitch angle amplitude, and b is the average pitch angle.

3.4 QBlade Software

The aim of QBlade software helps users for rapid design, reliable, robust predictions of aerodynamic characteristics and effect of flow around a rotor blade [47]. For an airfoil, XFOIL is integrated to rapidly design custom airfoils or import directly data of airfoil and calculate their polars and extrapolate the polar data to 360° . For a horizontal axis wind turbine, the Blade Element Momentum Theory (BEMT) is used to predict the efficiency. For a vertical axis wind turbine, the Double-Multiple Streamtube (DMS) model is introduced to consider the rotation of the blade and the energy production in upstream and downstream of the rotational axis.

In the Table 3.1 shows the different modules, the related objects and the analysis types that can be performed by the QBlade software. The arrows suggest the dependencies between them. Some key functionalities of the QBlade software as follow:

- Extrapolation of XFOIL to 360° angle of attack.
- Advanced blade design and optimization, using XFOIL generated or imported profiles.
- Input of wind turbine data (rotor blade, turbine control, generator type, losses)
- Calculation of rotor performance with tip speed ratio
- Calculation of wind turbine performance with wind speed
- Using BEM and DMS correction algorithms
- Storing of projects, rotors, turbines and simulations in a runtime database

3.5 FAST Simulation Capability

In this study, horizontal axis wind turbine aerodynamic analysis was performed using aerodynamic elastic FAST (Fatigue, Aerodynamics, Structures and Turbulence). It was developed by the National Renewable Energy Laboratory (NREL) [48]. In an actual design, the experiment requires cost, time and effort. Therefore, numerical analysis is a useful tool. From the analysis results, we clarified rotor load fluctuation accompanying cyclic pitch control.

In this research, the FAST code is used for simulation of the wind turbine with the collective and cyclic pitch control. Additionally, it can simulate both two-bladed and three-bladed horizontal axis wind turbines. For the two-bladed wind turbine, the aerodynamic uses 15 degrees of freedom (DOFs) to simulate the wind turbine motion. For the three-bladed wind turbine, it is 24 DOFs. Both two-bladed and three-bladed wind turbine, depending on each specific research case which the number of DOFs are switched on or off. The aerodynamic loads of wind turbine are also modeled in FAST code. The 3D wind profile is generated by TurbSim for the simulation.

The TurbSim code is written in Fortran 90 by researchers in the NREL [49]. The process of TurbSim simulation is shown in Fig 3.4. The TurbSim can numerically simulate a full-field flow that has turbulence. It simulates time series of three component wind speed vectors (u , v and w). TurbSim reads all parameters from input file such as runtime options, wind turbine specifications, meteorological boundary conditions and non-IEC conditions. It will check which turbulence model is used (Kaimal model or Von Karman spectral model). After, it finds the correct standard deviations for each component for the turbulence model and spectral model. Then, TurbSim generates the random numbers, and calculates the spectral and transfer function matrices. An inverse fast fourier transform (IFFT) is carried out to achieve the wind speeds. And then, if a parameter is set to measure all the wind speeds to satisfy the target standard deviation and mean wind speed, it will perform the scaling that parameter. Finally, it calculates the mean wind speed through the grid and the turbulence intensity from the simulated data.

Fig. 3.5 shows the overview of FAST code. FAST performs coupled analysis by AeroDyn which performs structural calculation and aerodynamic calculation in FAST. AeroDyn is an aerodynamic analysis module, and it is based on Blade Elemental Momentum Theory. Using the AeroDyn aerodynamic calculation result as an input, the stress etc. acting on the structural system is calculated by FAST, and the behavior of the blade is fed back to the calculation of AeroDyn again. At the time of analyzing to output the time series data, this process is performed at each time. As the calculation result, time series data such as power generation output, load acting on each element and structural displacement are outputted. Also, in FAST, analysis by structural system and ADAMS capable of load analysis can be performed in parallel. ADAMS is a development of widely used multibody dynamics software for wind turbine analysis. We can analyze the behavior of wind turbine parts and the distribution of load and force

FAST, AeroDyn, ADAMS require their respective input files. Fig. 3.6 shows the input and output data file in the analysis. The FAST Primary file need many data as input analysis data such as test wind turbine control conditions, analysis initial condition and wind turbine design data. The wind turbine design data includes the size of the blade, the nacelle and the tower, the weight, and the specifications of the generator. In the FAST Tower file and Blade file, input the rigidity, damping coefficient, mode shape, etc. of each structure.

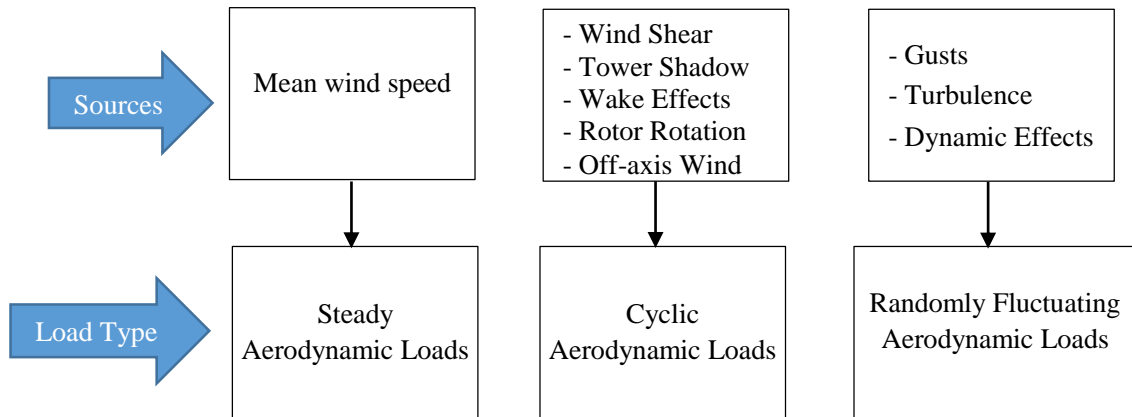


Fig. 3.1 Loads on wind turbine

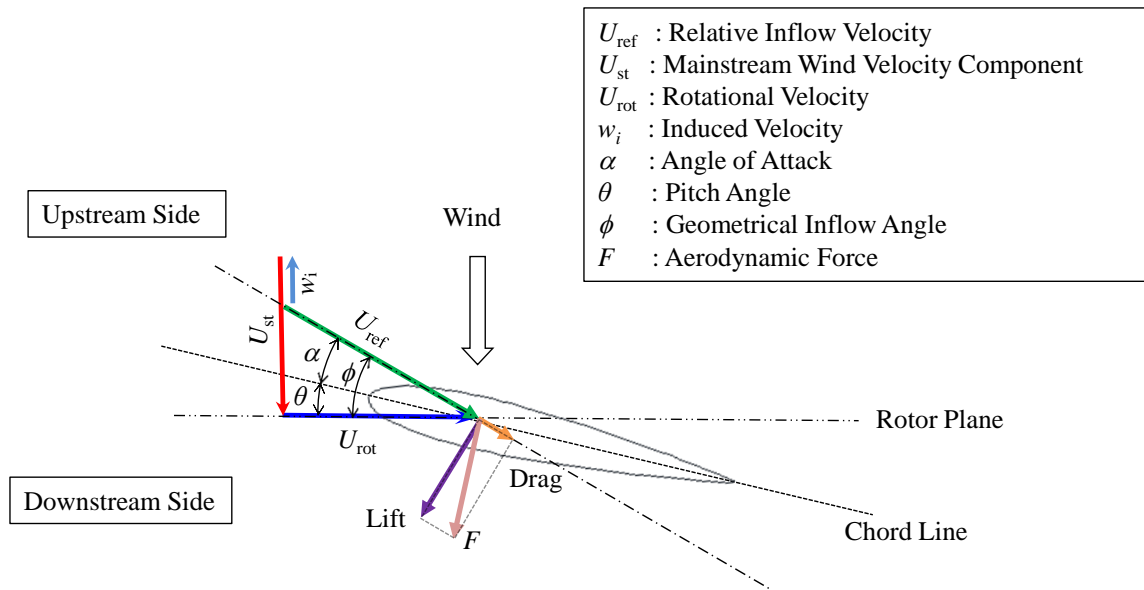
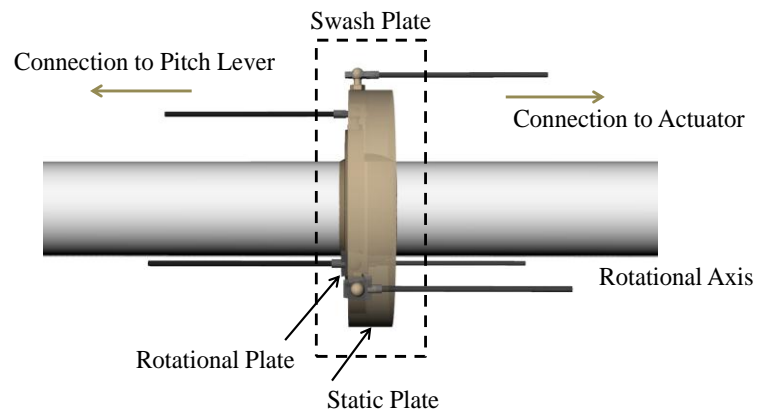
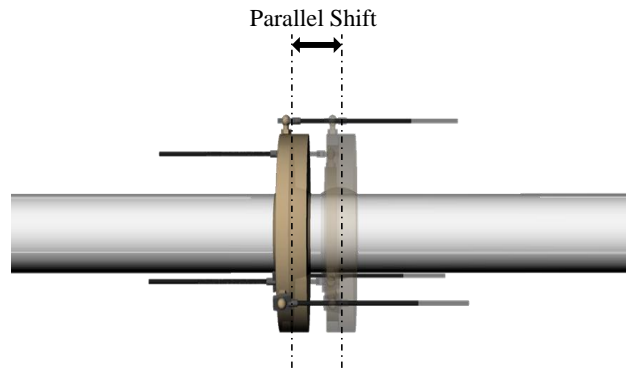


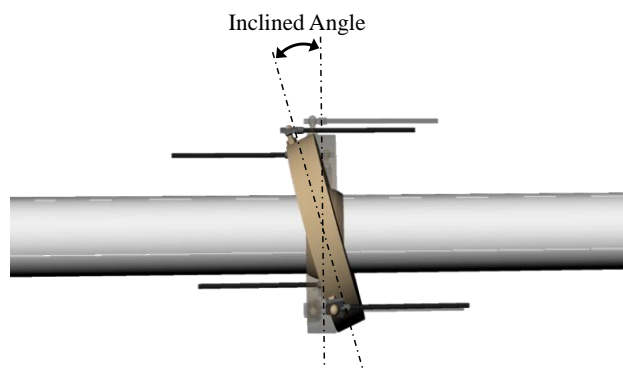
Fig. 3.2 Relation between relative inflow wind, pitch angle and angle of attack



(a) Mechanism of swash plate



(b) Parallel movement of swash plate



(c) Tilt movement of swash plate

Fig. 3.3 Simple diagram of swash plate system

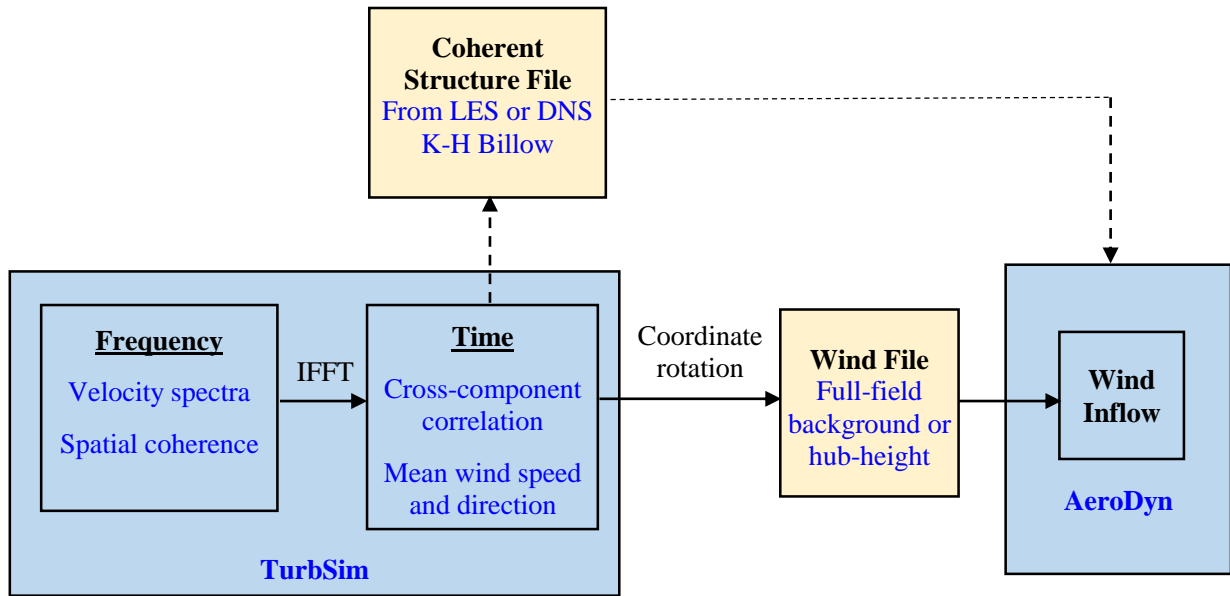


Fig. 3.4 TurbSim simulation process
(Source: TurbSim User's Guide: Version 1.06.00 [48])

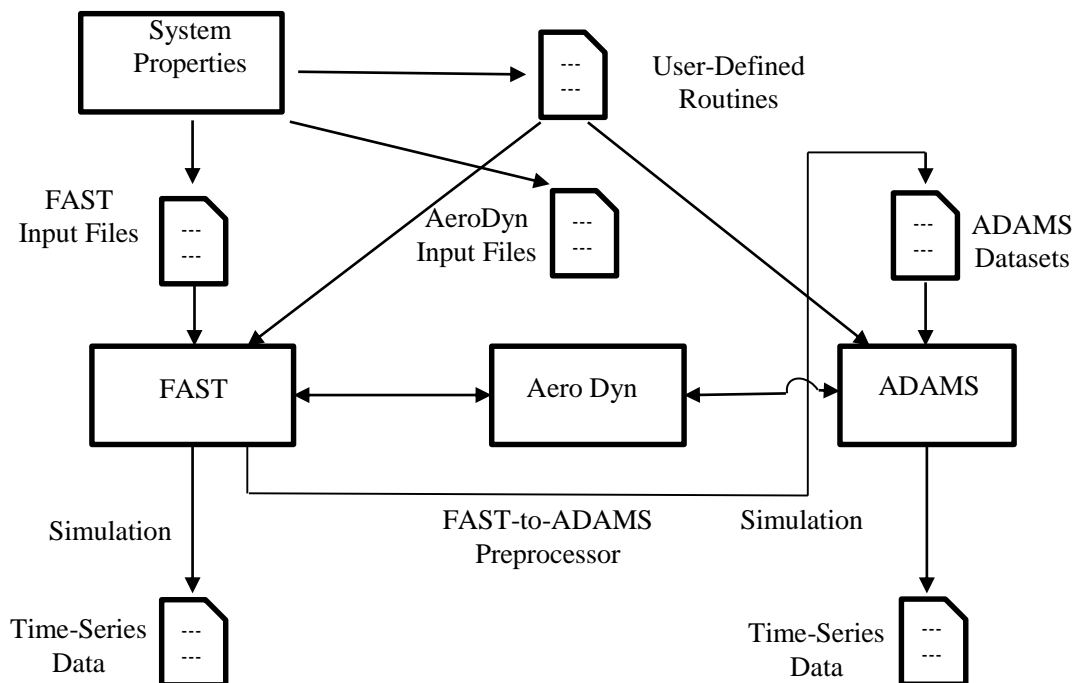


Fig. 3.5 Overview of FAST code
(Source: FAST User's Guide [47])

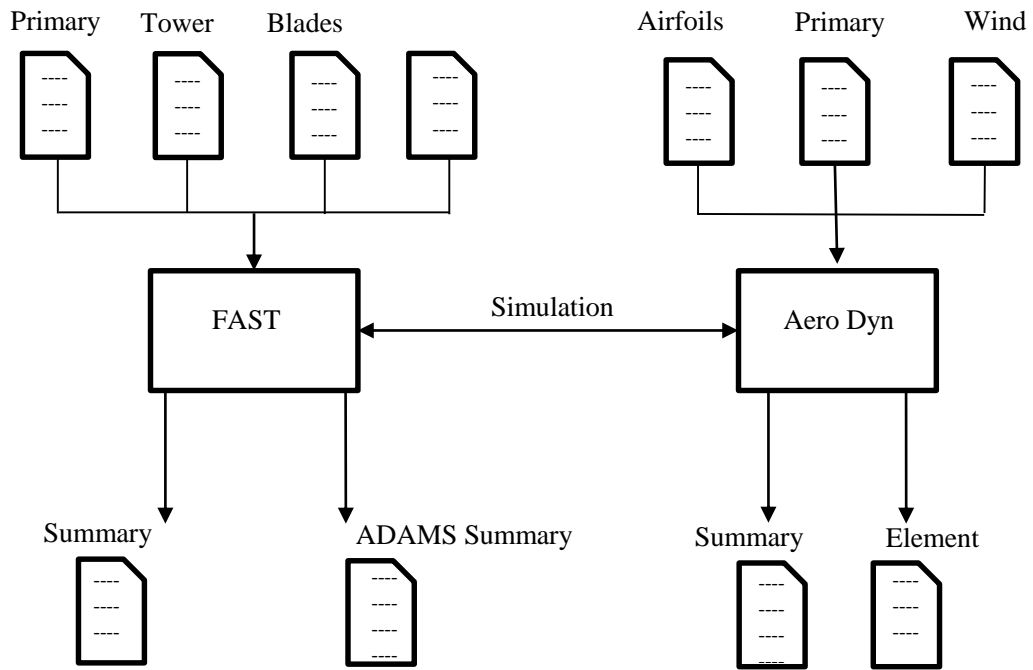


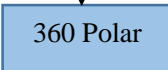

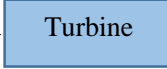
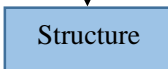


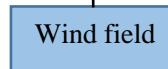


Fig. 3.6 Input and output data of the analysis process
(Source: FAST User's Guide [47])

Table 3.1 QBlades object structure, modules and analysis types
 (Source: QBlade Short Manual: Version 0.8 [46])

Modules	Objects	Analysis type
Airfoil design	 ↓	
XFoil analysis	 ↓	Viscous - Inviscid 2D Panel method
Polar extrapolation	 ↓	Flat plate extrapolation
Blade design	 ↓	Steady BEM simulation
Turbine design & Simulation	 ↓	Steady BEM simulation
Structural blade design	 ↓	Euler Beam modal analysis
Static blade loading	 ↓	Euler Beam static deflection
NREL FAST simulation	 ↓	Unsteady BEM and structural dynamics
Wind field generator	 ↑	Veers Sandia method correlated time series

Chapter 4 Effect of turbulence intensity on performance of HAWT

In the natural condition, wind always shows unsteady change both the direction and magnitude. Therefore, the wind turbine performance is affected by the turbulence and the wind condition. In this chapter, the performance change of the wind turbine in the low-turbulence flow and the simulated results of the high turbulent flow are discussed. The 3-bladed upwind wind turbine was used in this experiment. In order to generate the turbulent inflow, an active turbulence grid system was used and installed in the wind tunnel. The QBlade software was used to simulate turbulence wind field and effect of it on wind turbine performance.

4.1 Experimental Apparatus

4.1.1 Wind tunnel

The experiment was carried out in the wind tunnel of Fluid Engineering Laboratory for Energy and Environment of Mie University, as shown in Fig. 4.1 (a). The wind tunnel has an outlet diameter of 3.6 m with the inlet size of 4.0 m × 4.0 m and the test section length is a 6.2 m which is shown in Fig. 4.1 (b). In this experiment, the mainstream wind velocity is set at 7.5 m/s. The non-uniformity of flow at the inlet of the test section is about 1.2 % and the measured turbulence intensity is less than 0.5 %.

The model wind turbine is installed in the test section of the wind tunnel, as shown in Fig. 4.1 (b). The model wind turbine is a three-bladed upwind horizontal axis wind turbine with the rotor diameter of $D = 1.6$ m and the hub height is 1.535m as shown in Fig. 4.2 (a). The geometrical shape of blade are illustrated in Fig. 4.2 (b). The shape of the test blade is designed by the blade element momentum theory. The blade has the chord length and the twist angle distribution along the blade span. The maximum twist angle $\theta_{\text{twist}} = 16.6^\circ$ is at radial position $r/R = 0.2$. For the measurements, the blade pitch angle at the blade tip is set at 0° . The blade was proved that could maintain the power performance in low Reynolds number region of $Re \geq 1.0 \times 10^5$ as shown in Fig. 4.7. The rotor rotational speed is adjusted by a variable speed generator. It can be set set up to a maximum of 1200 rpm. This nacelle consists of a variable speed generator, an encoder, a slip-ring and a coupling. Considering the effects of blockage, local wind velocity without wind turbine was also measured at the same region. The blockage ratio is the ratio between the rotor swept area and the wind tunnel uniform flow area.

A 6-component balance system is installed in the region between the nacelle and the tower as shown in Fig. 4.3. This balance can measure simultaneously the forces and moments applied to the entire wind turbine in the three directions of x , y and z -axes. From this figure, the load forces acting on the rotor are calculated on the basis of the rotor centre, which is defined as the origin of the coordinate system in the measurement. The measurement values detected from the 6-component balance can be transmitted to the personal computer from the signal processor as a digital value as shown in Fig. 4.4.

4.1.2 Active turbulence grid

The active turbulence grid is composed of twelve horizontal and twelve vertical rotating shafts to which diamond-shaped winglets are attached as seen in Fig. 4.5. The turbulent flow is generated by the dynamic turbulence grating installed in the wind tunnel. Fig. 4.5 (a) shows a photograph of the dynamic turbulence grating, and Fig. 4.5 (b) shows a schematic view. This device consists of 288 agitating blades attached to 12 rotating shafts in each of vertical and horizontal directions, a frame, and 24 servomotors. The dynamic turbulence grating gives turbulence to the main flow wind by the rotational motion of the agitating blades attached to the rotating shaft assembled in a lattice with a lattice spacing $M = 300$ mm. In addition, each agitating blade is controlled by the command of a personal computer to change its angle and angular velocity. Blockage ratio parameter is used when designs the turbulence intensity. The installed position of the active turbulence grid is shown in Fig. 4.1 (b). The average turbulence intensities which are registered at the turbine rotor plane are $TI = 1.6\%$.

4.2 Experimental Methods

4.2.1 Experimental conditions

In this study, the experiment was carried out under the mainstream wind velocity of $U = 7.5$ m/s. Wind turbine power performance is measured at the turbulence intensity of $TI = 1.6\%$ (the low-turbulence flow).

4.2.2 Sectional performance of the test blade

The two-dimensional airfoil performance experiment was performed to consider the stable of the Avistar airfoil under low Re number condition. The wind tunnel composes of a blower, a rectification part, a contraction part and a measured part. The blower is a flow fan of 55 kW, and the wind speed can be set steadily by the inverter. The maximum wind speed is 52 m/s, the turbulent intensity is 0.20% at the wind speed 22 m/s. The experimental apparatus consists of a test airfoil, a servomotor, and a high-speed multipoint pressure measuring device. The test airfoil is attached to the center height of the measured part. Disks that can be rotated smoothly by bearings are installed on the left and right side walls of the measured part, and the test airfoil can be set to an arbitrary angle of attack.

Fig. 4.6 shows the distribution of pressure taps used for calculating the lift and drag forces. In order to measure pressure distribution applied to the blade surface, in the span of airfoil center height, one of the rotor blades is provided with pressure taps with a diameter of 0.4 mm and the total number of 23. As shown in Fig. 4.6, the red circles indicate the position of pressure measurement taps. The forces acting on the characteristic length s_i are obtained by $(p_i - p_0)s_i$. The lift force L and the drag force D per unit blade width, together with all the forces acting in the lift direction and drag direction, are obtained by integrating over the entire blade surface. They can be determined as follows:

$$L = \sum (p_i - p_0) \cdot s_i \cdot \sin(\theta_i + \alpha) \quad (4.1)$$

$$D = \sum (p_i - p_0) \cdot s_i \cdot \cos(\theta_i + \alpha) \quad (4.2)$$

Here, p_0 and p_i are the reference pressure point and measured pressure at the i -th tap of airfoil, respectively, θ_i is an inclination angle against the blade chord line at the i -th of the measured pressure tap, and α is an angle of attack.

The lift and drag coefficient are defined:

$$C_l = \frac{L}{(1/2)\rho U^2 c} \quad (4.3)$$

$$C_d = \frac{D}{(1/2)\rho U^2 c} \quad (4.4)$$

where, L is lift force, D is drag force, c is chord length, U is mainstream wind velocity

The Reynolds number is defined as follow:

$$Re = \frac{cU}{\nu} \quad (4.5)$$

here, ν is a kinematic viscosity of air, ρ is the density of air, A is the rotor swept area.

The output power from a wind turbine is shown as a power coefficient C_P , and it is defined as follow:

$$C_P = \frac{P}{0.5\rho AU^3} \quad (4.6)$$

$$C_T = \frac{T}{0.5\rho AU^2} \quad (4.7)$$

where, C_P is the power coefficient, C_T is the thrust coefficient, P is the power output and T is the thrust force acting on wind turbine.

The tip speed ratio is the ratio of the blade tip velocity and the mainstream wind velocity U , which is shown as follows:

$$\lambda = \frac{R\omega}{U} \quad (4.8)$$

where, R is rotor radius, ω is the thrust coefficient,

4.3 Results of Experiment and Simulation

4.3.1 Lift and drag coefficients

The low Re number decreases performance of blade due to separation of boundary layer. Therefore, the low Re number will affect experimental results. Rotor blades were designed using the blade element momentum theory. The blade profile shape used Avistar airfoil for full span of the blade. The airfoil performance is checked when Re number changed. The two-dimensional airfoil performance experiments are carried out at the different Reynolds numbers.

In this case, the design conditions of the model wind turbine are rotor diameter of 1.6 m, mainstream wind velocity of 8 m/s, and the optimal tip speed ratio $\lambda = 8$ and the Reynolds number of rotor blades is calculated as $Re = 1.5 \times 10^5$. Therefore, a two-dimensional airfoil performance test was conducted under the condition of $Re = 0.5 \times 10^5$, 1.0×10^5 , 1.5×10^5 and 2.0×10^5 , it means that the Reynolds number range of the experiment includes the experimental conditions of the model wind turbine.

Fig. 4.7 shows the lift coefficient with the angle of attack when the Re number changed. As seen in this figure, the horizontal axis is the angle of attack α , and the vertical axis represents the lift coefficient C_L , respectively. In these experiments, the blade surface pressure distribution and the downstream velocity distribution of the test blade were measured at the angle of attack from -20° to $+50^\circ$ at 1° intervals. The lift coefficient was calculated only from the blade surface pressure distribution, whereas the drag coefficient was calculated from the comb-type pitot tube. The Re number was changed respectively 0.5×10^5 , 1.0×10^5 , 1.5×10^5 and 2.0×10^5 . From obtained results, for $Re = 0.5 \times 10^5$, the lift coefficient is different trend with remain cases at the low angle of attack ($-10^\circ < \alpha < +13^\circ$) because the influence of viscous are remarkable and momentum of the flow unable to move downstream and adverse pressure gradient causes the laminar flow to separate. The separated flow attach again to the surface due to the transition. The laminar separation vortex region appears between laminar separation and turbulent reattachment region. The vortex region has adverse effects such as decreased lift coefficient, increased drag coefficient, so the lift coefficient is lower. For three Re numbers of $Re = 1.0 \times 10^5$, 1.5×10^5 and 2.0×10^5 , the lift coefficient shows a similar trend regardless of the Reynolds number in a wide angle of attack range including a stall region. Therefore, it proves that when the Re number is more than from $Re = 1.0 \times 10^5$, the lift characteristics is a stable. The stable characteristic means did not change when the Re number changed. So, the low Re numbers don't have a significant effect on the blade performance or experimental results.

Fig. 4.8 indicates the drag coefficient with the angle of attack when the Re number changed. As seen in this figure, the horizontal axis is the angle of attack α , and the vertical axis is the drag coefficient C_D , respectively. The drag coefficient shows the similar trend to the lift coefficient, for three Re numbers of $Re = 1.0 \times 10^5$, 1.5×10^5 and 2.0×10^5 , the drag coefficient indicates stable characteristics in the wide angle of attack range. Therefore, the airfoil section for model blade is selected as the the Avistar airfoil.

Fig. 4.9 and Fig. 4.10 describe the simulated lift coefficient comparing with measurement data at the Re number of 1.5×10^5 and 2.0×10^5 under non-turbulence condition, respectively. The XFOIL is integrated into QBlade

software was used to simulate effect of the low Re number on the blade performance. In this simulation, the pressures acting on the airfoil surface are simulated at the angle of attack from -20° to $+30^\circ$ at 1° intervals. As described in these figures, the horizontal axis is the angle of attack α , and the vertical axis represents the lift coefficient C_L , respectively. From these figures, they can be seen that there is similar tendency between the measured data with the simulated result. Moreover, the simulated result is a little lower than the measurement data in the range of $-20^\circ < \alpha < 10^\circ$. The difference between the measured data and the simulation result for $Re = 2.0 \times 10^5$ is smaller than that for $Re = 1.5 \times 10^5$. This is because of the viscous drag.

Fig. 4.11 and Fig. 4.12 show the simulated drag coefficient comparing with measurement data at the *Reynolds* number of 1.5×10^5 and 2.0×10^5 . The horizontal axis is the angle of attack α , and the vertical axis represents the drag coefficient C_D , respectively. From these figures, there is similar trend between the measured data with the simulated result. The drag coefficient data of QBlade simulation is slightly lower than measured data that of in the range of $-5^\circ < \alpha < 30^\circ$. For the $Re = 2.0 \times 10^5$, the difference of the measured data and the simulation result is also smaller.

From some above results show that the QBlade software can simulate almost agree with measurement data.

4.3.2 Power and thrust coefficients

Fig. 4.13 describes the power coefficient against tip speed ratio at the turbulent intensity of 1.6%. As shown in this figure, the horizontal axis shows the angle of attack α , and the vertical axis is the power coefficient C_P . For the measurement data, the optimum tip speed ratio is $\lambda = 6.47$ with the optimum power coefficient of $C_P = 0.391$. The optimum tip speed of $\lambda = 6.74$ and the optimum power coefficient of $C_P = 0.406$ from QBlade simulation are higher than measurement data. There is a disagreement between experimental data and simulated result in the low tip speed ratio and the high tip speed ratio regions. Because in these regions, there are a flow separation and stall on the blade surface. However, around the optimum tip speed ratio region, the simulated result is a quite similar with the measured data, because there is not the flow separation.

Fig. 4.14 shows the thrust coefficient with the tip speed ratio. Thrust coefficient shows similar tendency between measurement data and simulated result. The two curves crossed at the value of the optimal tip speed ratio of the measurement data, $\lambda=6.47$, this is an interesting coincidence.

Fig 4.15 and Fig. 4.16 show the simulation of turbulence wind at $TI = 1.6\%$ and 10.5% . The mainstream velocity is 7.5 m/s. The maximum wind speed of $TI=1.6\%$ is 7.88 m/s and $TI=10.5\%$ is 9.78 m/s. Sandia simulation method is integrated into the QBlade software to simulate turbulent wind field [46]. This method uses the power spectral densities and coherences to simulate a mesh of correlated time series.

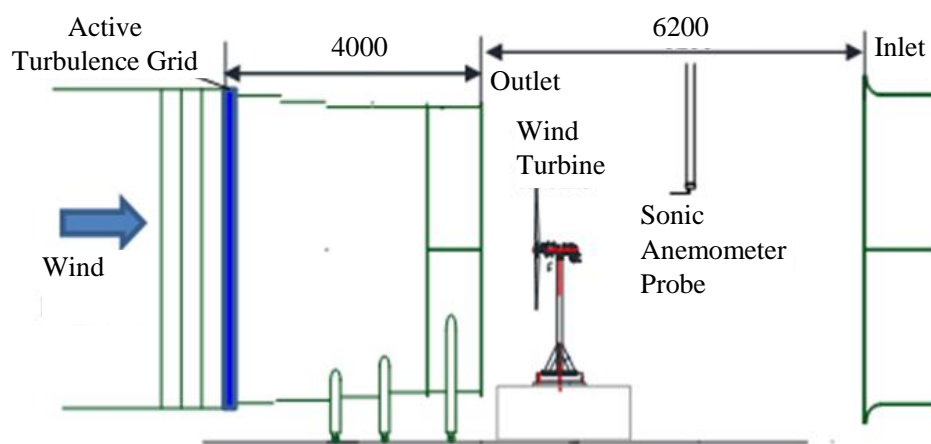
Fig 4.17 indicates the simulation of effect of turbulent intensity on power coefficient. The red curve is the measurement data at $TI=1.6\%$, the open violet curve presents the simulated results at $TI=1.6\%$ and the open blue curve is the simulated results at $TI=10.5\%$. From this figure, the power coefficient of the simulated result at $TI=10.5\%$ obtains $C_P = 0.484$ and $\lambda=7.78$, they are higher than the measurement data at $TI=1.6\%$. This is explained as following:

One of the reasons the wind turbine performance decreased under low turbulence is the flow separation around the wind turbine blades from the suction side of it. Because, for the low turbulence flow case, momentum exchange takes insufficient strong, the flow is unable to modify to the going up pressure and there is a flow separation from the surface of the blade. The flow separation of the low turbulence is large for the boundary layer, so the wind turbine performance is low. While for the high turbulence wind case, the increased transport of momentum from the free-stream to the blade surface increases the streamwise momentum in the boundary layer. This permits the free-stream to overcome the pressure gradient of the rotor blade surface, so the separation region is much smaller and the performance of the wind turbine becomes larger. But the flow still separates in the further downstream on blade surface. Therefore, for the high turbulence case, the power coefficient is higher than the low turbulence case.

From that above results, the turbulence level has significant impact on wind turbine performance.

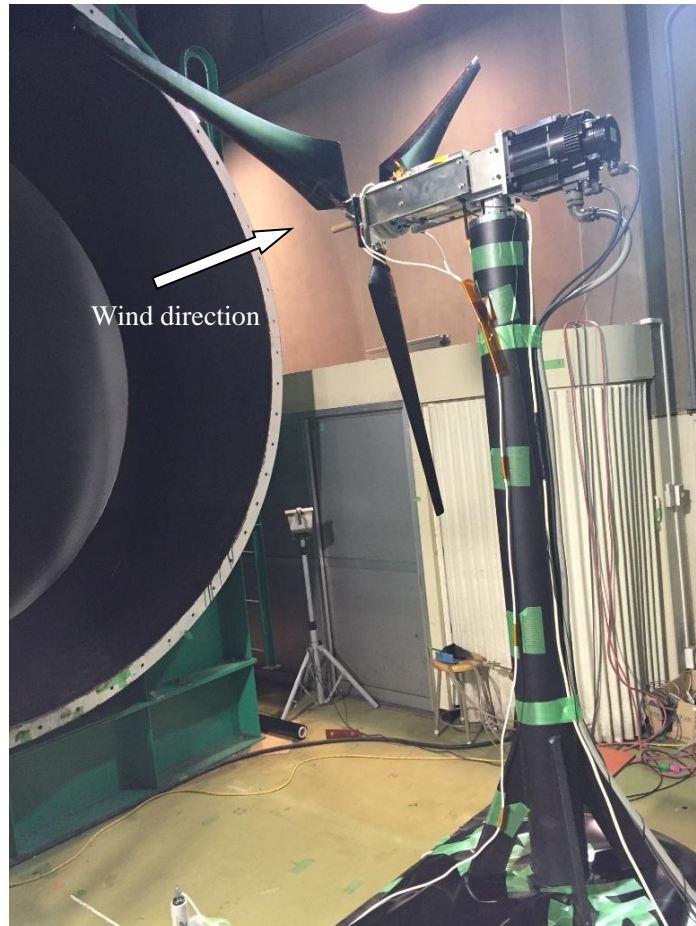


(a) Outside view of the wind tunnel laboratory



(b) Overall view of the large wind tunnel

Fig. 4.1 Simple diagram of experimental equipment.



(a) Three-bladed upwind wind turbine model (seen from back side)

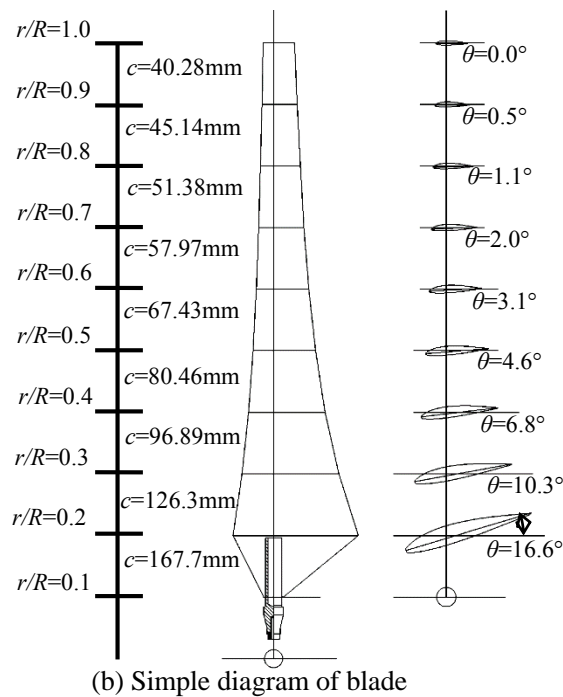


Fig. 4.2 Wind turbine model and the blade structure

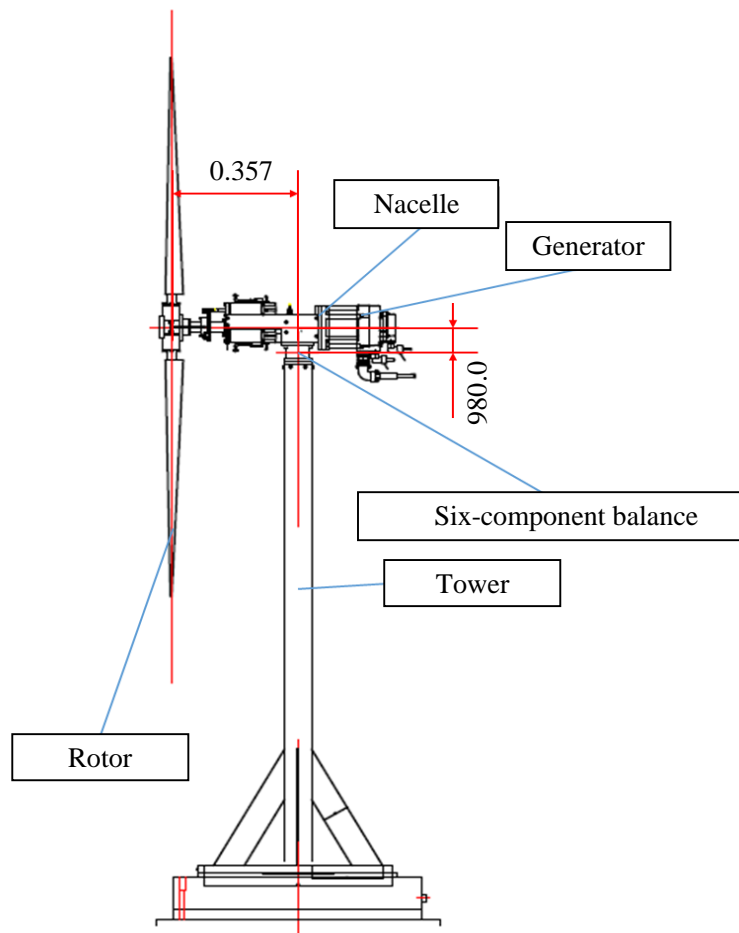


Fig. 4.3 Schematic drawing of wind turbine and six-component balance

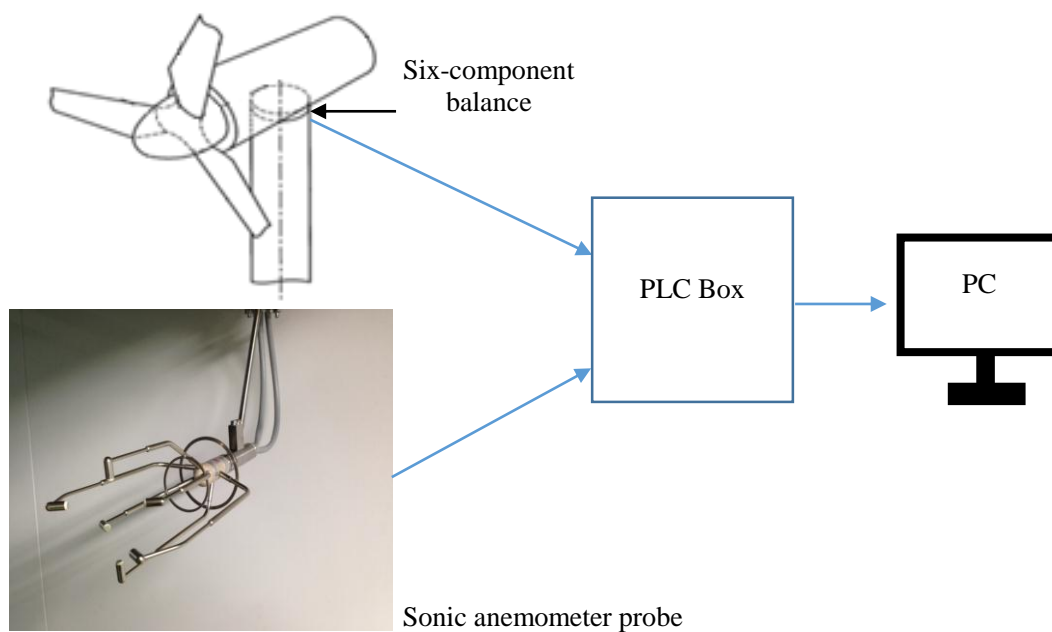


Fig. 4.4 Simple diagram of signal flow of measurement devices

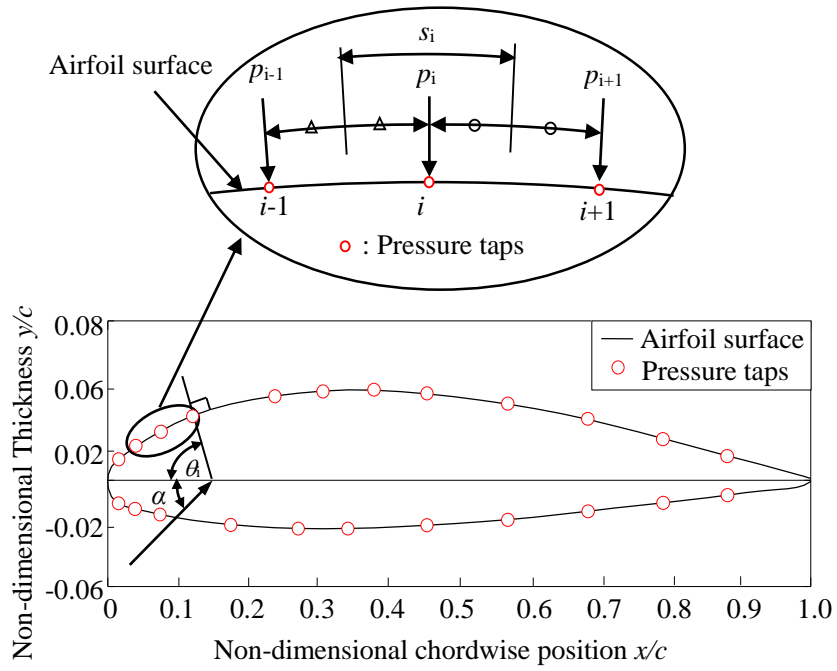


Fig. 4.6 Geometry of Avistar airfoil and the pressure tap positions

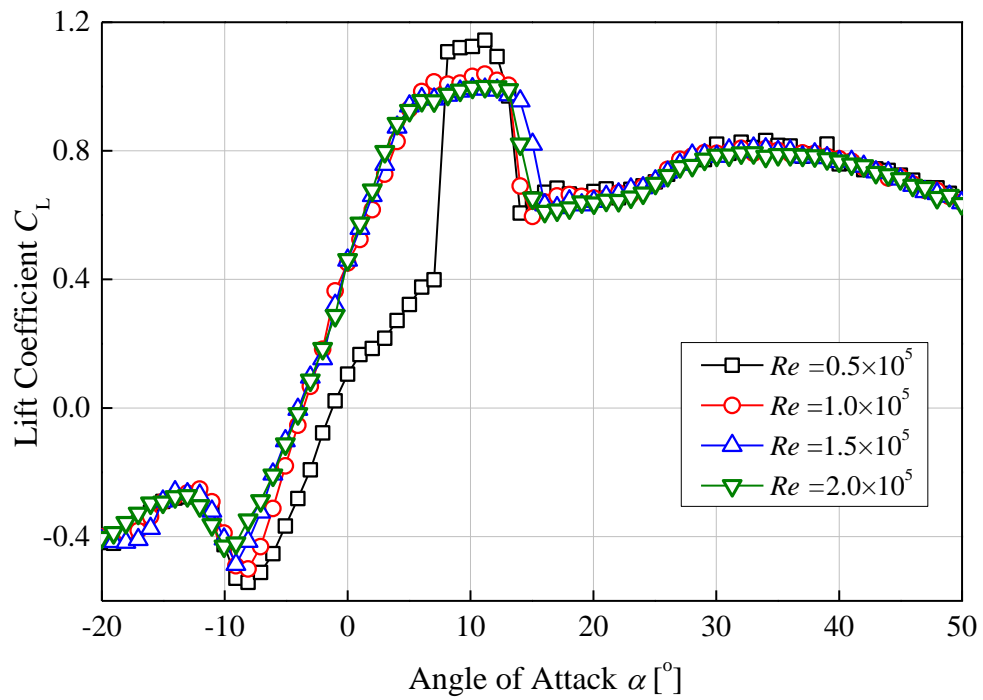


Fig. 4.7 Lift coefficient with angle of attack at Re number change

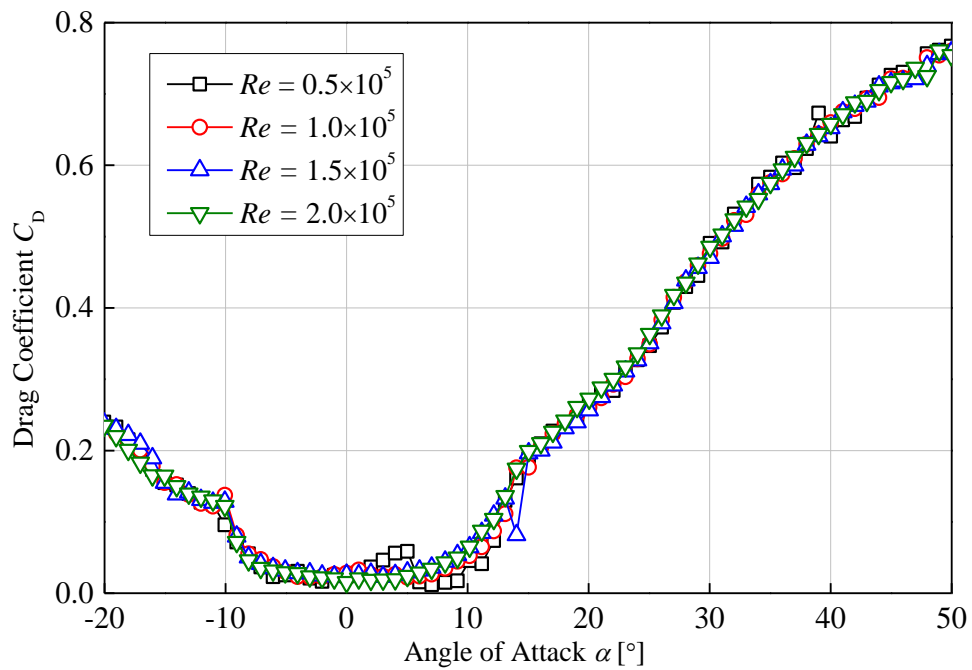


Fig. 4.8 Drag coefficient with angle of attack at Re number change

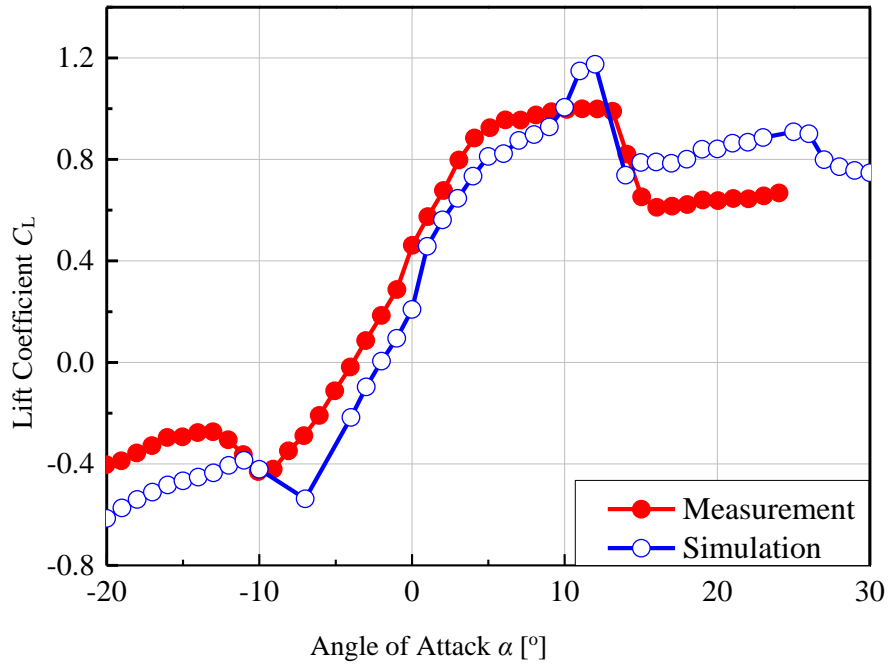


Fig. 4.9 Lift coefficient with angle of attack at $Re=1.5 \times 10^5$

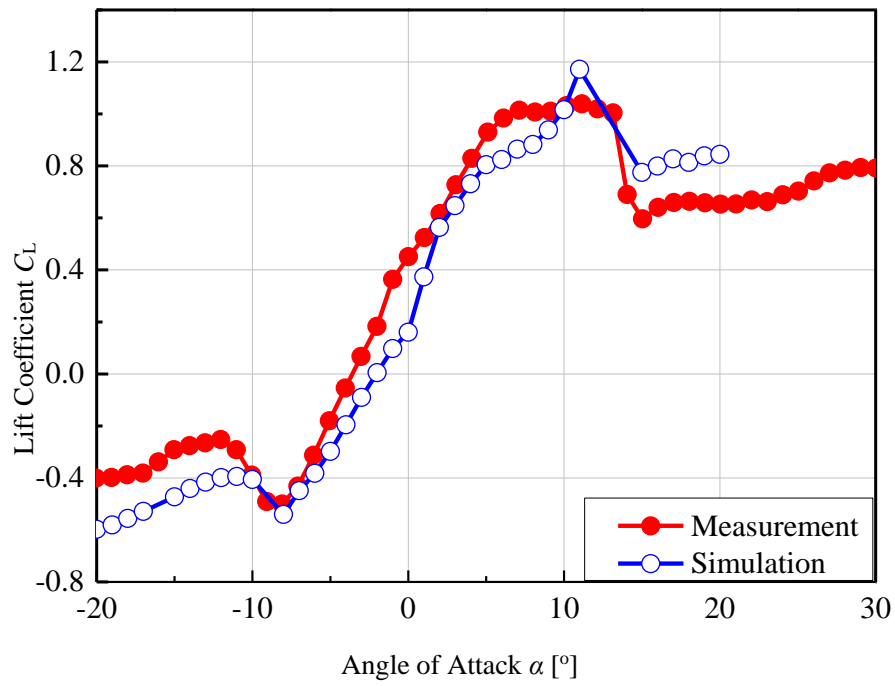


Fig. 4.10 Lift coefficient with angle of attack at $Re=2.0 \times 10^5$

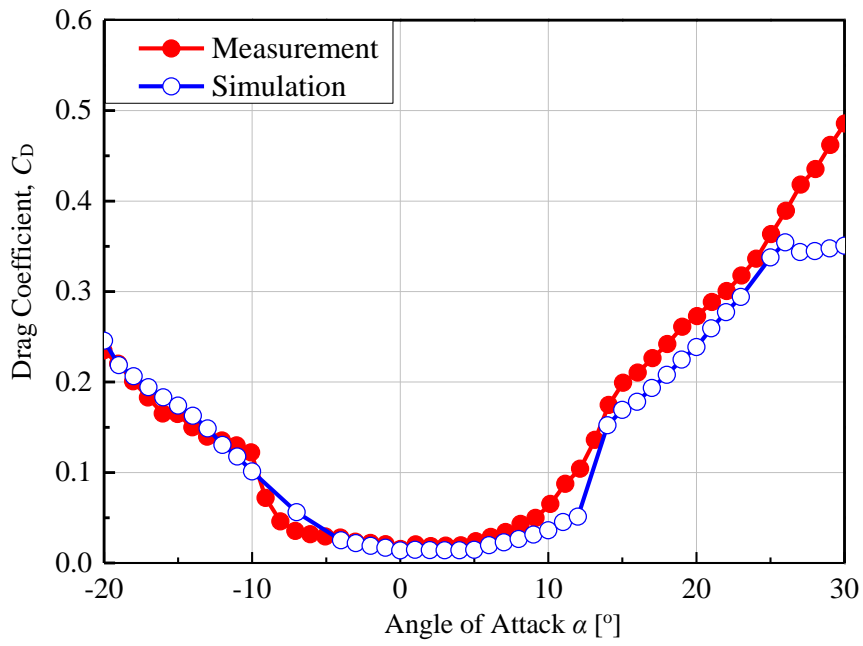


Fig. 4.11 Drag coefficient with angle of attack at $Re=1.5 \times 10^5$

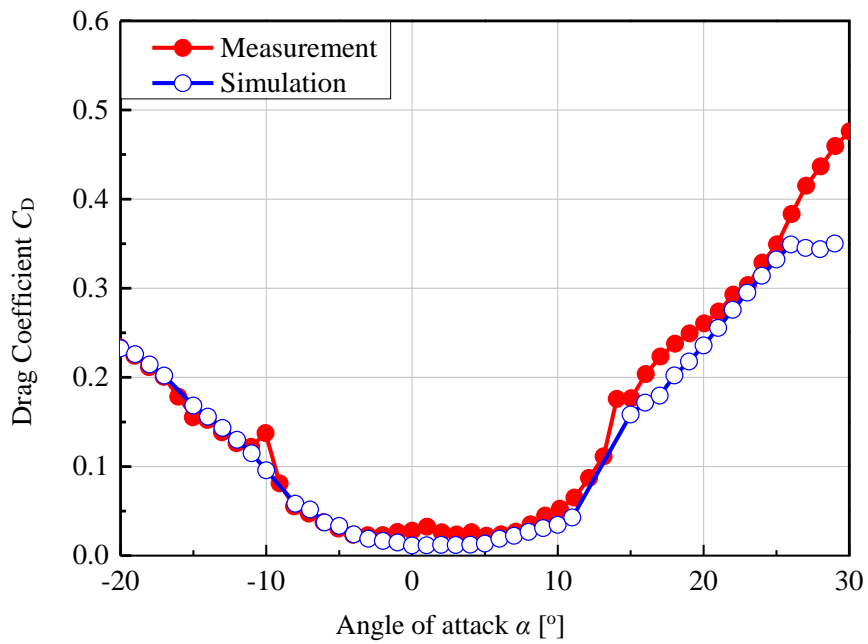


Fig. 4.12 Drag coefficient with angle of attack at $Re=2.0 \times 10^5$

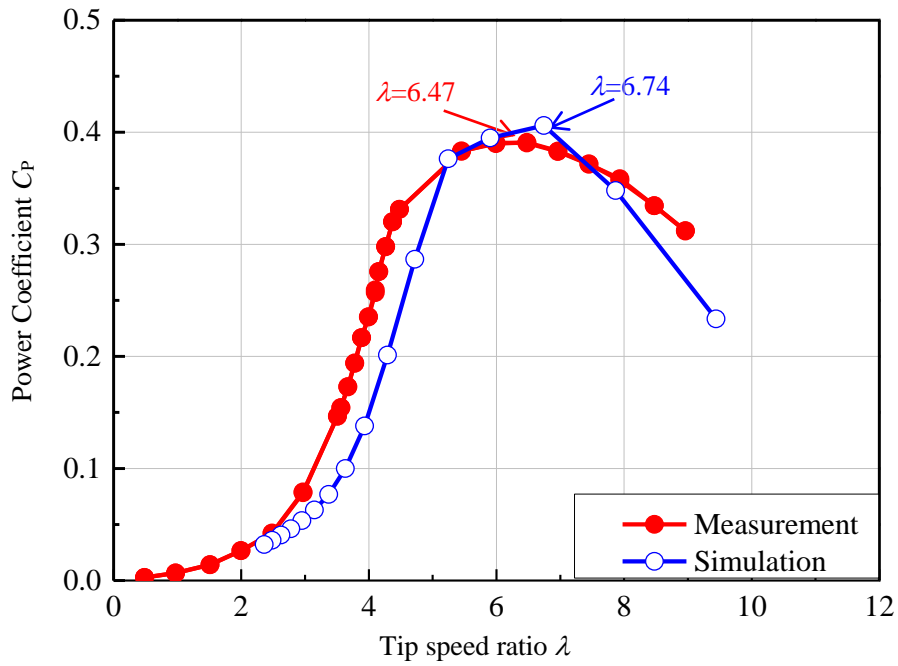


Fig. 4.13 Power coefficient with tip speed ratio at $TI = 1.6\%$

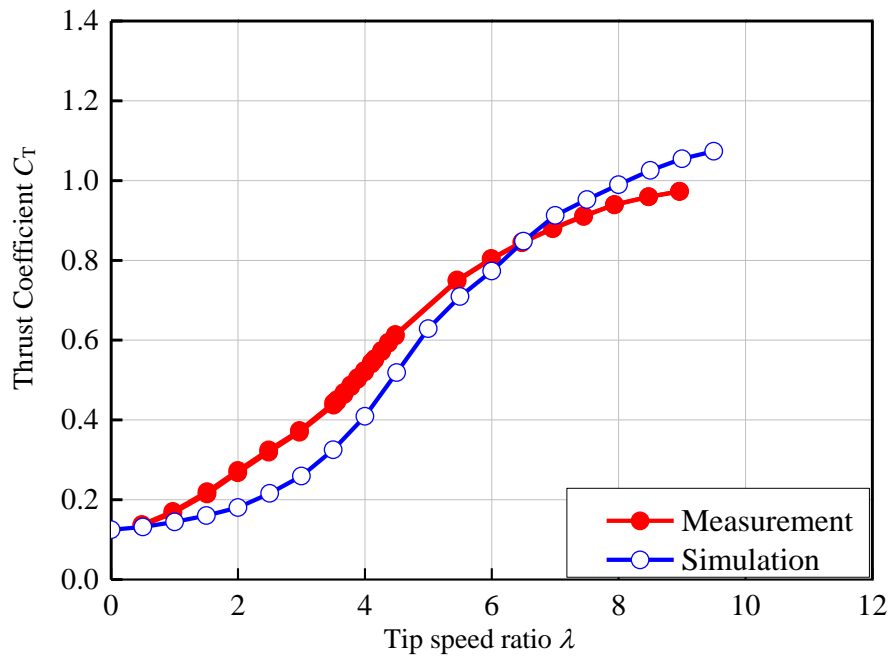


Fig. 4.14 Thrust coefficient with tip speed ratio at $TI = 1.6\%$

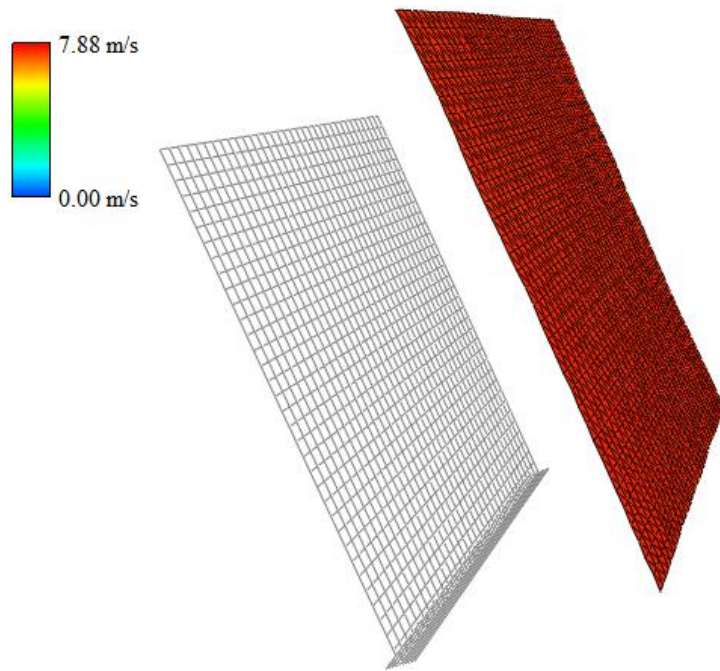


Fig. 4.15 Turbulence intensity simulation, $TI=1.6\%$

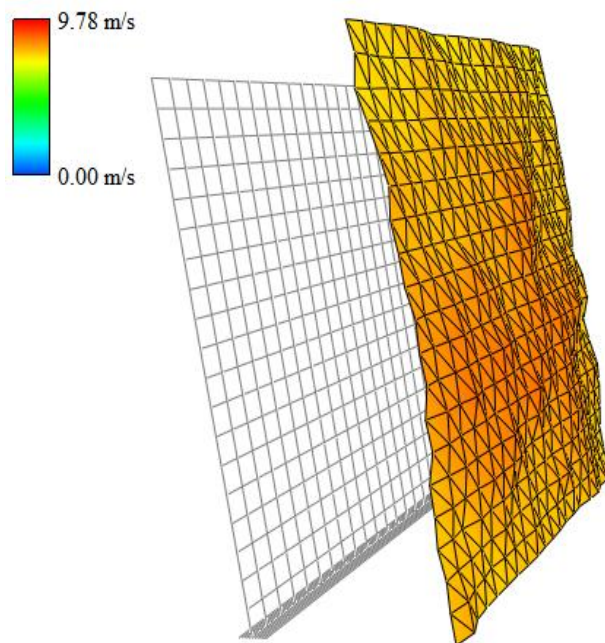


Fig. 4.16 Turbulence intensity simulation, $TI=10.5\%$

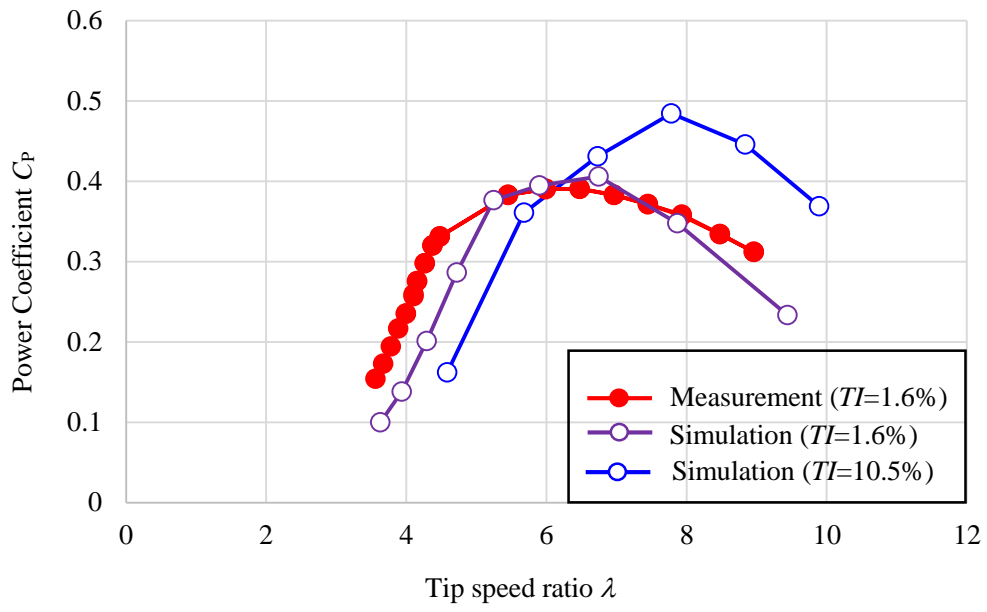


Fig. 4.17 Simulation of effect of TI on power coefficient

Chapter 5 Load fluctuation on HAWT for extreme wind direction change

The extreme wind direction change is one of the complex wind conditions which has been specified in the International Electrotechnical Commission (IEC) 61400-1 wind turbine design requirement standard. External conditions can generate extreme loads which may affect the power coefficient and the lifetime of HAWTs. The aerodynamic forces acting on a small HAWT under extreme wind direction change condition were investigated in the wind tunnel experiments. The two-bladed and three-bladed wind turbines were used in this experiment.

5.1 Experimental Apparatus and Conditions

5.1.1 Wind tunnel and model wind turbine

The experiment was carried out in the wind tunnel of Fluid Engineering Laboratory for Energy and Environment of Mie University, as shown in Fig. 4.1. A hot-wire anemometer is used to measure the mainstream wind velocity in the wind tunnel outlet. The output signal of hot-wire anemometer has obtained 65536 points per measurement at 20 kHz by a 16 bit A/D converter.

The model wind turbine is installed in the main test section of the wind tunnel, as shown in Fig. 5.1 (a). The model wind turbine has a rotor diameter of $D = 1.6$ m, and the mainstream wind velocity is set at 8.0 m/s. The two different wind turbines with two blades and three blades rotor was tested in the same parameters. Figs. 5.2 (a) and (b) show the photos of the two different wind turbines. A six-component balance at tower top can measure the forces and moments applied to the entire wind turbine in the three directions of x , y and z -axes, illustrated in in Fig. 5.1 (b). The pitching moment and yawing moment are defined in Fig. 5.1 (c).

In order to reduce the influence on the flow field around the wind turbine, the nacelle is covered with a nacelle cover. The rotational speed of the rotor is controlled by a variable speed generator. The rotor torque and the rotational speed are measured by a variable speed generator. The rotational direction of the rotor is clockwise when viewed from the upstream side. The azimuth angle of the rotor is defined as 0° when the reference blade faces vertically upward and the direction of rotor rotation is defined as the positive azimuth angle.

5.1.2 Sudden wind direction change equipment

Fig. 5.1 (a) describes the position of sudden wind direction change equipment in the wind tunnel. The sudden wind direction change equipment is installed between the wind tunnel outlet and the test wind turbine. The wind direction change equipment consists of two servo motors and a vane array. The vane array has 16 columns vanes with three stages of upper, middle and lower. The angle of vanes is controlled by two servo motors. Every vane is connected to the servo motor via link rod. The servo motors are Nikkidenso ND400-160-LS. The cross-sectional shape of the vane is a NACA0012 airfoil with the chord length of 0.3 m.

5.1.3 Experimental conditions

In order to inspect the effect of the extreme wind direction change on wind turbine, the wind condition and load analysis are discussed at several cases in the wind tunnel.

The sudden wind direction change is set according to the EDC. Wind direction changes of the EDC model $\theta(t)$ is defined by the following Eqs. (5.1) and (5.2).

$$\theta_e = \pm 4 \arctan \left\{ \frac{\sigma_1}{V_{\text{hub}} (1 + 0.1D / A_1)} \right\} \quad (5.1)$$

$$\theta(t) = \begin{cases} 0^\circ & \text{for } t < 0 \\ \pm 0.5\theta_e \{1 - \cos(\pi t/T_{\text{time}})\} & \text{for } 0 \leq t \leq T_{\text{time}} \\ \theta_e & \text{for } t > T_{\text{time}} \end{cases} \quad (5.2)$$

Here, θ_e is the wind direction change angle, T_{time} is the period of the sudden wind direction change, σ_1 is the standard deviation of the wind, V_{hub} is the hub height wind velocity, D is the rotor diameter, and A_1 is the turbulence scale parameter, respectively.

As shown in Table 5.1, a 10 MW wind turbine is assumed, the rotor diameter is $D = 200$ m, the hub height wind velocity is $V_{\text{hub}} = 11$ m/s, the turbulence scale parameter is $A_1 = 91$ m, and the wind direction change angle is $\theta_e = \pm 28.2^\circ$. In addition, according to the IEC61400-1 standard, the period for the extreme wind direction change is given as $T_{\text{time}} = 6$ s. The period for wind direction change for wind tunnel test is decided by the scale ratio between the actual and modelled wind turbine. The rotor diameter of the wind turbine model is $D = 1.6$ m and the mainstream wind velocity is 8.0 m/s. There is a correlation between the 10 MW wind turbine and wind turbine model in wind tunnel such as the rotor diameter ratio of (1.6/200), the wind velocity ratio of (8/11) and the determine time scale ratio of (1.6/200 \times 11/8). Therefore, the period for the sudden wind direction change in this wind tunnel experiment is $6 \times 1.6/200 \times 11/8 = 0.066$ s.

Fig. 5.3 shows the vane array which can generate the sudden wind direction change in the wind tunnel test section. The vane angle is defined as the angle between the wind direction and the movement plane of vane. In this experiment, the wind direction after vane array is changed from -14.1° to $+14.1^\circ$ from the centerline of wind tunnel to keep the model wind turbine in the core region of the wind during wind direction change. In addition, the yawed angle of wind turbine is formed between the wind direction and the center axis at the hub height of wind turbine. The model wind turbine is fixed at yawed angle of -14.1° from centerline of the wind tunnel. Therefore, the wind direction change seeing from wind turbine is from 0° to -28.2° , as shown in Fig. 5.4.

5.2 Experimental Results

5.2.1 Extreme wind direction change simulation

Fig 5.5 (a) and Table 5.2 indicate position of 5 measured points in the rotor plane (seen from the upstream). Fig. 5.5 (b) shows the measured wind direction at the 5 points in the rotor plane of the model wind turbine. The vertical axis is the wind direction and the horizontal axis presents the time based on the trigger signal. The measured wind directions at the 5 points show good agreement, and it is considered that the wind direction changes uniformly in the rotor plane. In addition, the wind directions before and after change are close to the target values of -14.1° and $+14.1^\circ$, respectively. The sudden change of the wind direction starts about 0.6 seconds after the trigger signal. This is the time difference caused by the distance between the wind direction change equipment and the wind turbine rotor plane.

The rotor azimuth angle at the wind direction change ϕ_{WDC} is shown as follows:

$$\phi_{\text{WDC}} = \phi_{\text{TRG}} + \Delta t_{\text{WDC}} \times \omega \quad (5.3)$$

where, ϕ_{TRG} is the azimuth angle at the trigger timing for the wind direction change equipment, Δt_{WDC} is the time delay from the trigger to the wind direction change at the rotor, and ω is the rotor angular velocity.

Fig. 5.6 shows the time series of the vane angle, the averaged wind direction the EDC model wind direction. The black line shows vane angle. The blue line and red line show the wind direction of measurement and the EDC model. In this figure, the wind direction of EDC model is started at -14.1° , because the model wind turbine is installed at the yaw angle of -14.1° . So, the wind direction change is set from -14.1° to $+14.1^\circ$. The time in horizontal axis is based on the start time of the sudden wind direction change. As shown in this figure, it has a good agreement with the results from the EDC model in IEC standard. From figure 5.6, it is confirmed that the sudden wind direction change is completed at the targeted 0.066 seconds.

In this experiment, the vane movement can't generate immediately the sudden wind direction change, because the shed vortices are generated by the start and end of vane movement. The service valves are expanded on before and after main vane to cancel out the vortex effects. The time of sudden wind direction change is 0.066s (this time is the period that changes the wind direction in the Fig. 5.6). As the result, the total time of vane operation is 0.6 seconds. Therefore, the time of 0.066 seconds can be considered a part of the time of 0.6 seconds.

From the measurement result of the wind direction change in the wind tunnel, the sudden wind direction change is possible to generate wind direction change well in agreement with the EDC model.

5.2.2 Wind turbine performance in steady wind

This experiment is performed without the extreme wind direction change. The wind turbine is operated in the mainstream wind velocity of 8 m/s with the yaw misalignment of 0 degrees. The output power was evaluated by the rotor torque and the rotational speed.

Fig. 5.7 compares the fluctuation of the output power coefficient for the two-bladed and three-bladed wind turbines. The vertical axis is the power coefficient and the horizontal axis represents the tip speed ratio. From this figure, the maximum power coefficient for the two-bladed wind turbine is obtained at the tip speed ratio of $\lambda = 7.15$. In the case of three-bladed wind turbine, the optimal tip speed ratio is $\lambda = 5.62$. The optimal tip speed ratio of three-bladed one is lower than that for the two-bladed one. Because the solidity of the three-bladed wind turbine is larger than the two-bladed.

5.2.3 Load measurement of two-bladed and three-bladed wind turbines

The yaw misalignment angle is changed from 0° to -28.2° with the wind direction change. The load fluctuation of the wind turbine may depend on the rotor azimuth angle when the sudden wind direction change reaches the rotor.

The optimal tip speed ratios are 7.15 for the two-bladed and 5.62 for the three-bladed one, respectively as shown Fig 5.7. The rotor rotational speeds are 680 rpm for the two-bladed and 560 rpm for the three-bladed, respectively. Fig. 5.8 (a) shows the time series of measured yaw misalignment, the pitching moment on the tower top for the two-bladed wind turbine. The horizontal axis shows the time based on the trigger timing of the wind direction change equipment. The grey bar exhibits finishing the vane operation and the total time of vane movement is 0.6 seconds. The averaged value of pitching moment M_x is negative due to the 6-component balance which is located at the coordinate axis of wind turbine. From this figure, the amplitude of pitching moment fluctuation increases after 0.6 s. This is because the aerodynamic force acting on the rotor blades varies with yaw misalignment angle and the fluctuation of the rotor blades effects on wind turbine oscillation due to the influence of the force.

Similarly, Fig. 5.8 (b) shows the time series of measured yaw misalignment, pitching moment on the tower top for the three-bladed wind turbine. The fluctuating amplitude on the pitching moment for three-bladed is smaller than two-bladed after the wind direction change. In order to evaluate the period effecting of wind direction change on the wind turbine load, the fluctuation amplitude of pitch moment is considered at the wind direction change. Fig. 5.8 indicates that the time which effects on the rotor of the three-bladed wind turbine is longer after the EDC effects on the rotor of the two wind turbines. Simultaneously, the fluctuation period is shorter than the two-bladed one. This proves that the solidity of the three-bladed wind turbine is higher than that for the two-bladed.

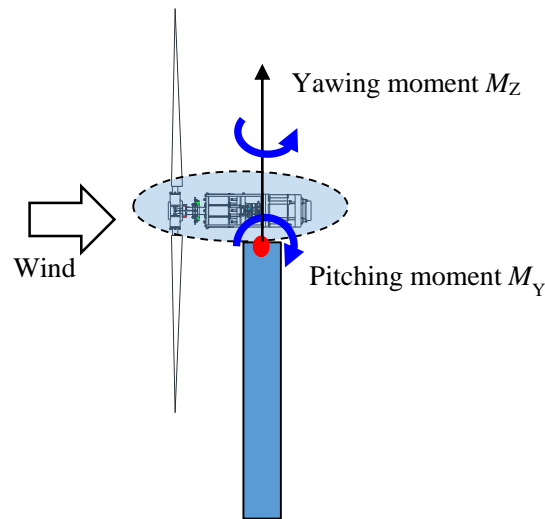
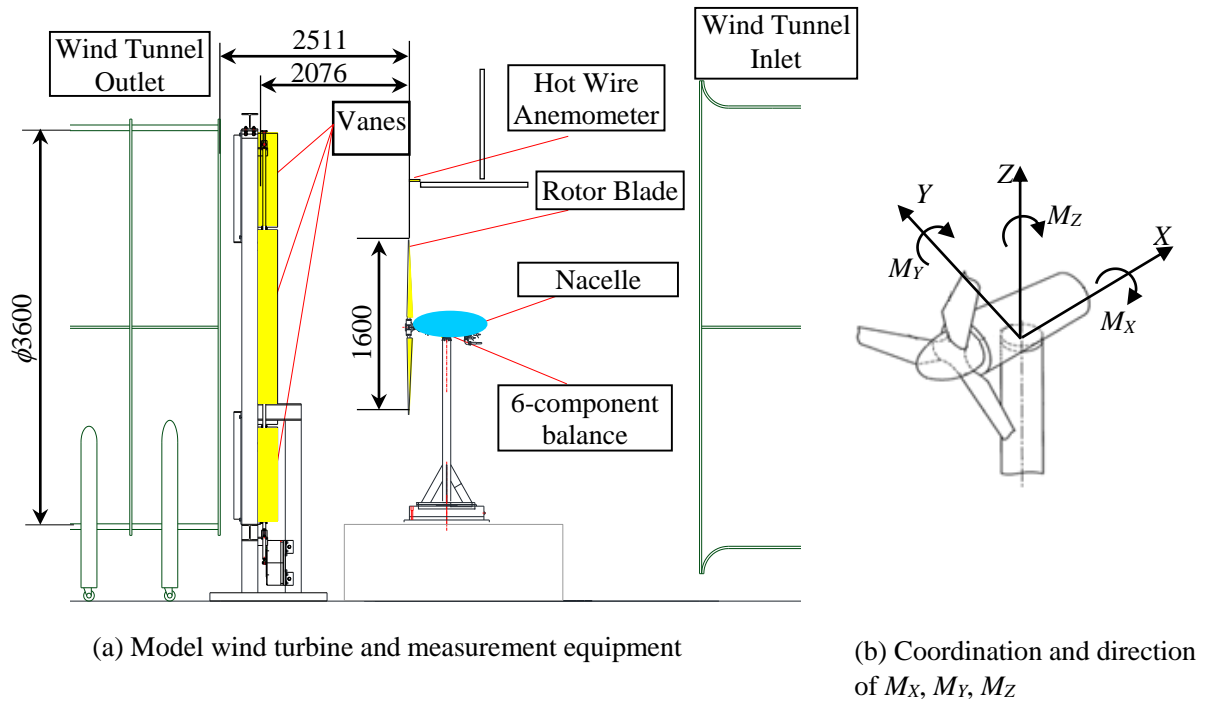
The yawing moment variations of the two-bladed and three-bladed wind turbines for the sudden wind direction change against the trigger criteria time are compared as seen in Fig. 5.9. The horizontal axis indicates the reference trigger time t , the vertical axis is the yawing moment M_z . The azimuth angle is set to 0° . From this figure, it can be seen that the yawing moment of the two-bladed shows larger fluctuation than the three-bladed one.

Fig. 5.10 (a) and (b) show the relation of the maximum yawing moment and the minimum yawing moment as a function of the azimuth angle. The horizontal axis indicates the azimuth angle, and the vertical axis represents the maximum yawing moment and the minimum yawing moment, respectively. Circle and tri-angle dots represent the two-bladed and three-bladed wind turbines. A large fluctuation of the yawing moment is seen for the two-bladed wind turbine, comparing with the three-bladed one.

The relation of the yawing moment amplitude and the azimuth angle is shown in the Fig. 5.10 (c). For the averaged value of the yawing moment amplitude, the two-bladed wind turbine is about 24.14 Nm while the three-bladed one is approximately 17.37 Nm. The yawing moment amplitude of two-bladed wind turbine is about 39% higher than the three-bladed one.

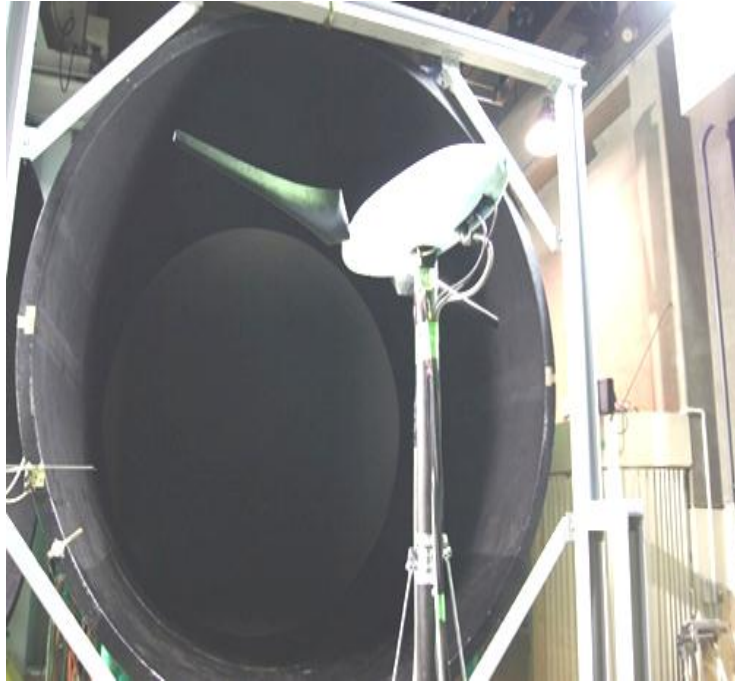
Fig. 5.11 (a) and (b) indicate the relation of the maximum pitching moment and the minimum pitching moment against azimuth angle. The horizontal axis exhibits azimuth angle, and the vertical axis is the maximum pitch moment and the minimum pitching moment, respectively. In the Fig.5.11 (a), the maximum pitching moment of the two-bladed wind turbine is higher than the three-bladed one. However, the minimum pitching moment of two wind turbines has no much difference. The reason is considered to be the influence of the angle of attack of the blade.

The relation between the pitching moment amplitude and the azimuth angle is shown in Fig. 5.11 (c). The pitching moment fluctuation amplitude of the two-bladed wind turbine has two peaks at the azimuth angles of $\phi_{WDC} = 60^\circ$ and 200° . It is seen that the fluctuation amplitude of the pitching moment has three periods during rotation for the three-bladed one. For the averaged value of the pitching moment amplitude, there is no significant difference between the two-bladed and three-bladed wind turbines. The strong dependence of the inflow timing of the wind direction change in the pitching moment fluctuation amplitude can be seen only for two-bladed wind turbine.

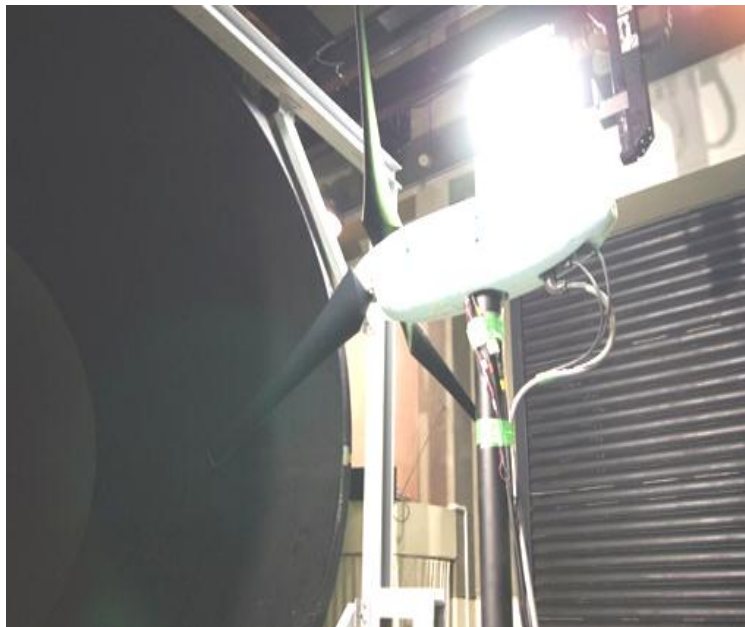


(c) Define pitching moment M_y and yawing moment M_z

Fig. 5.1 Schematic view of experimental apparatus in the large wind tunnel



(a) Two-bladed wind turbine



(b) Three-bladed wind turbine

Fig. 5.2 The model wind turbine



Fig. 5.3 Wind direction change equipment in wind tunnel

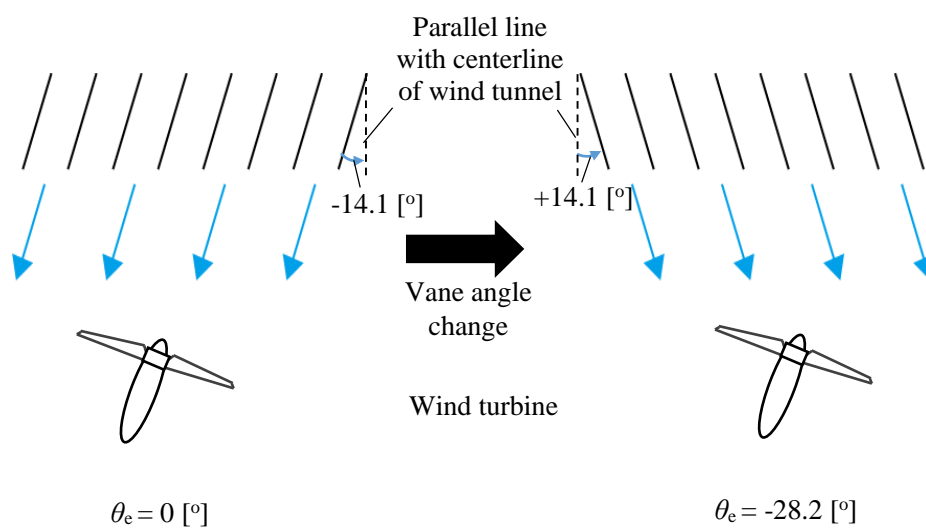
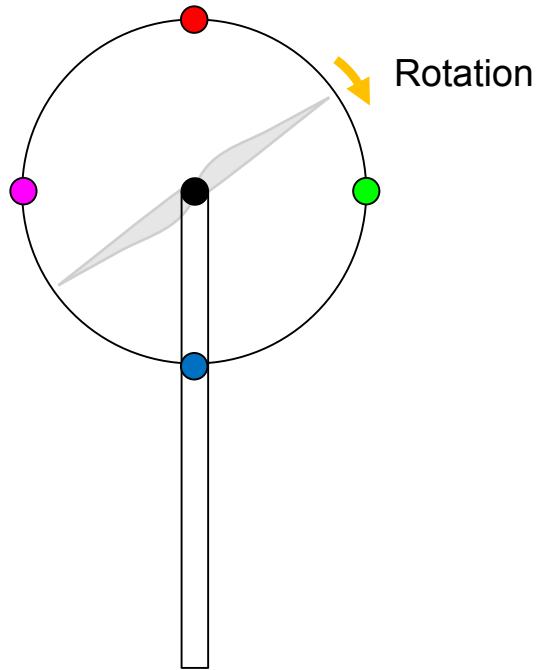
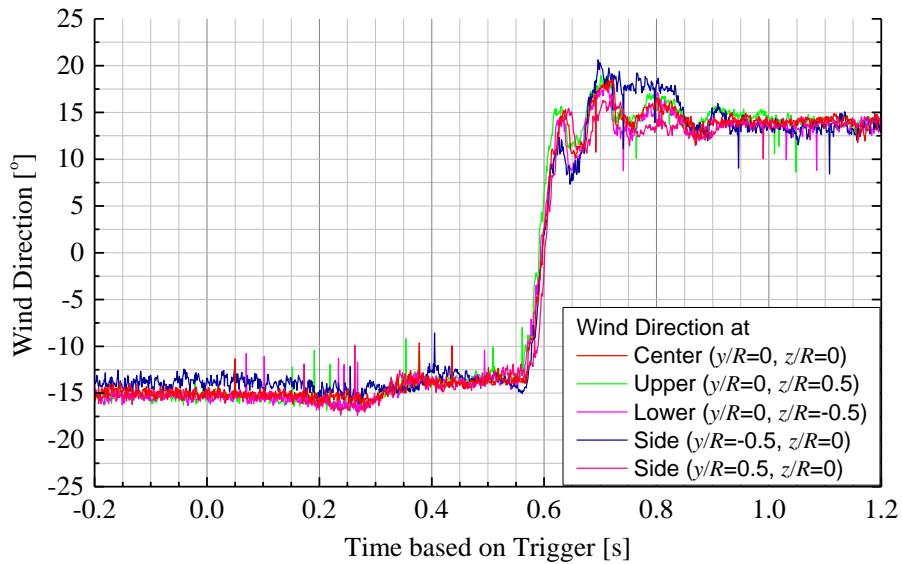


Fig. 5.4 Vane array angle changes from 0° to -28.2°



(a) Position of 5 measured points in the rotor plane (seen from the upstream)



(b) Measurement data at 5 points

Fig. 5.5 Wind direction change at five points in the rotor plane

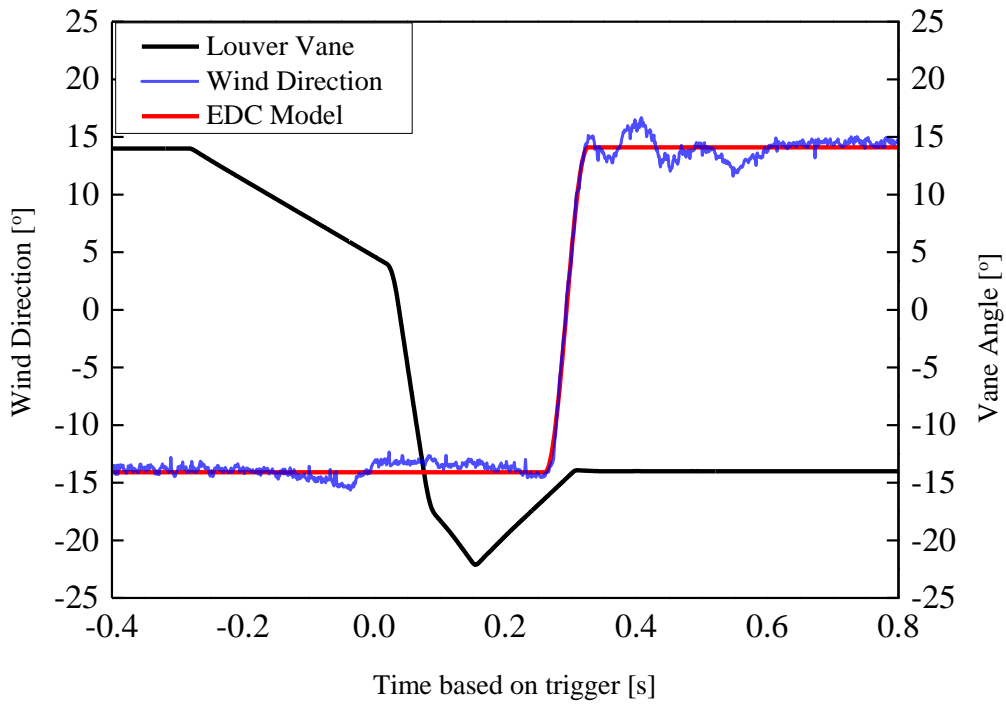


Fig. 5.6 Wind direction change and IEC EDC model in wind tunnel

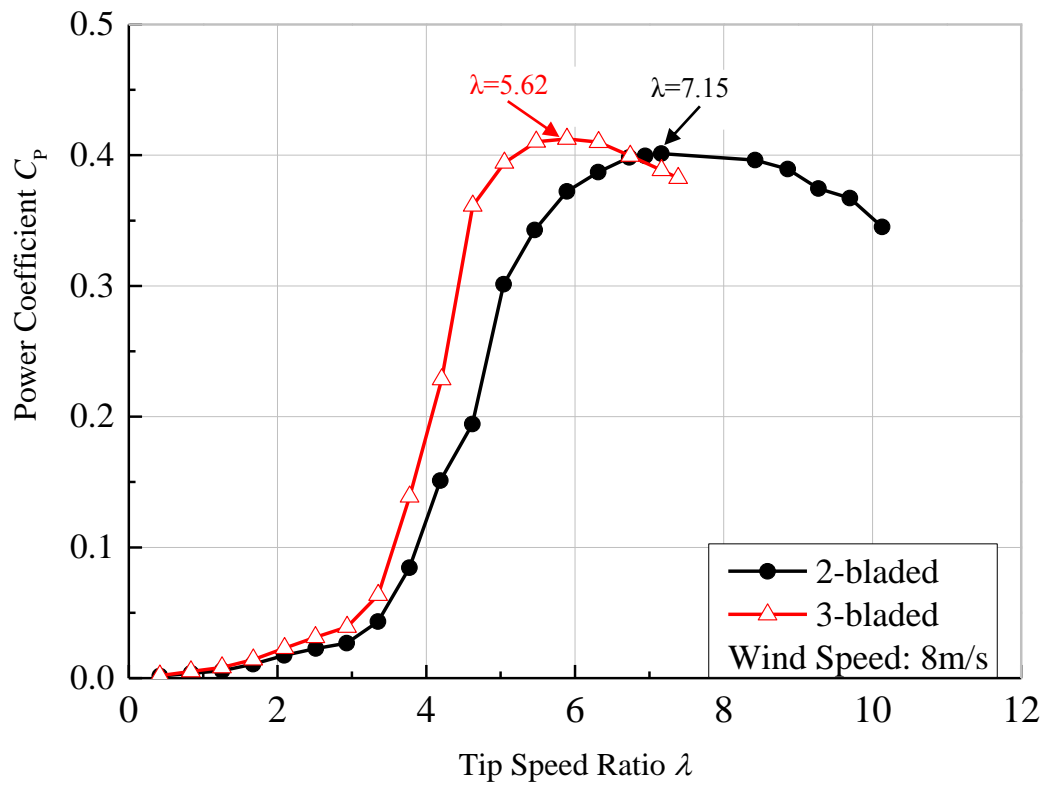
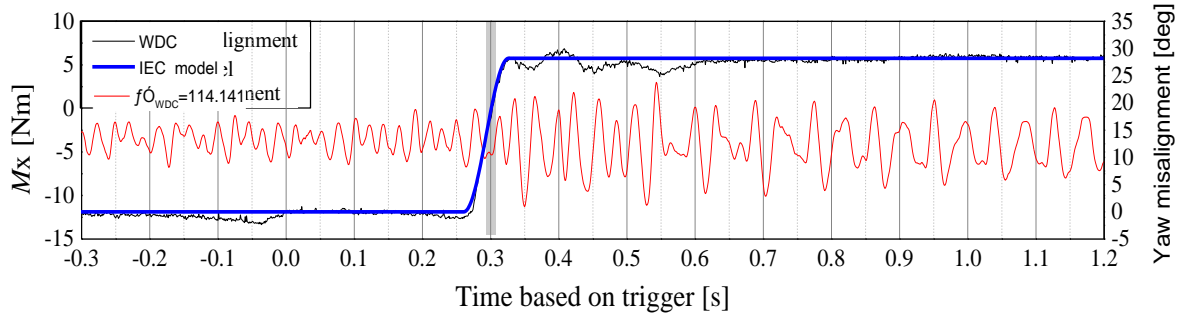
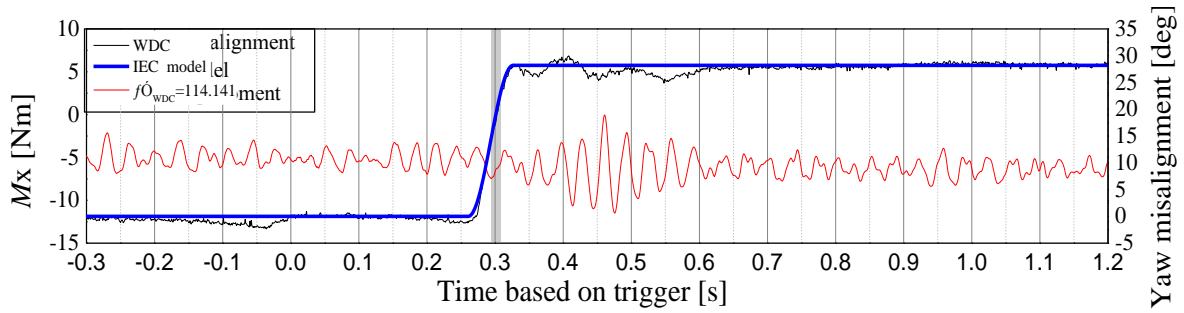


Fig. 5.7 Power coefficient curve of two-bladed and three-bladed wind turbines



(a) Two-bladed wind turbine



(b) Three-bladed wind turbine

Fig. 5.8 Fluctuation of pitching moment of two-bladed and three-bladed wind turbines

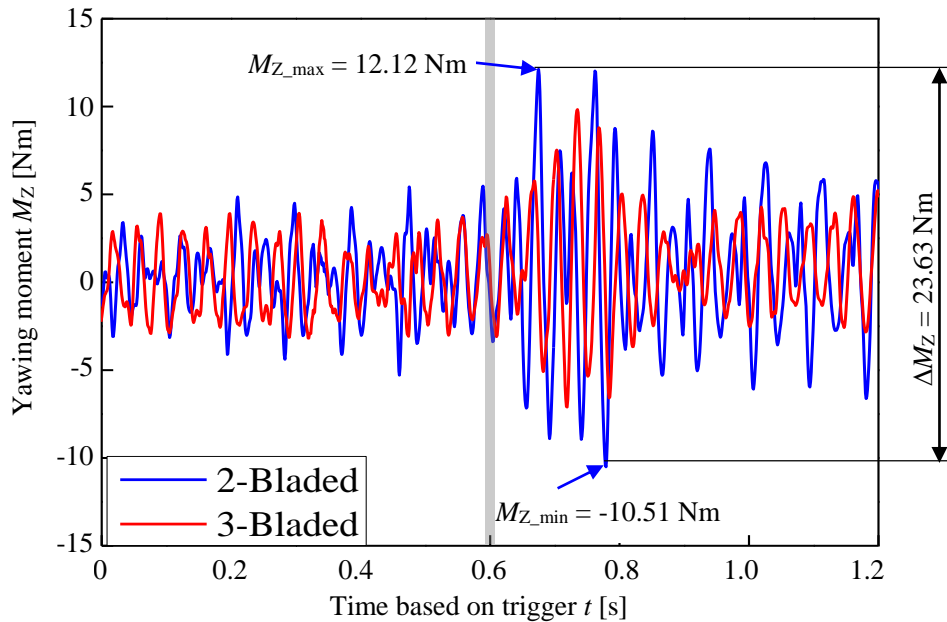
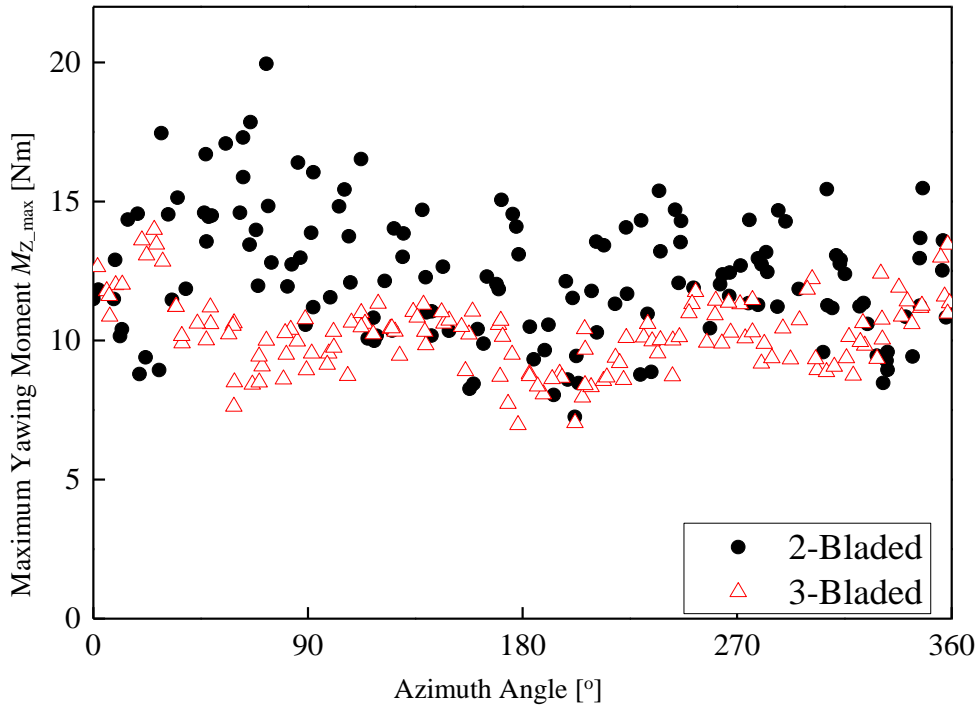
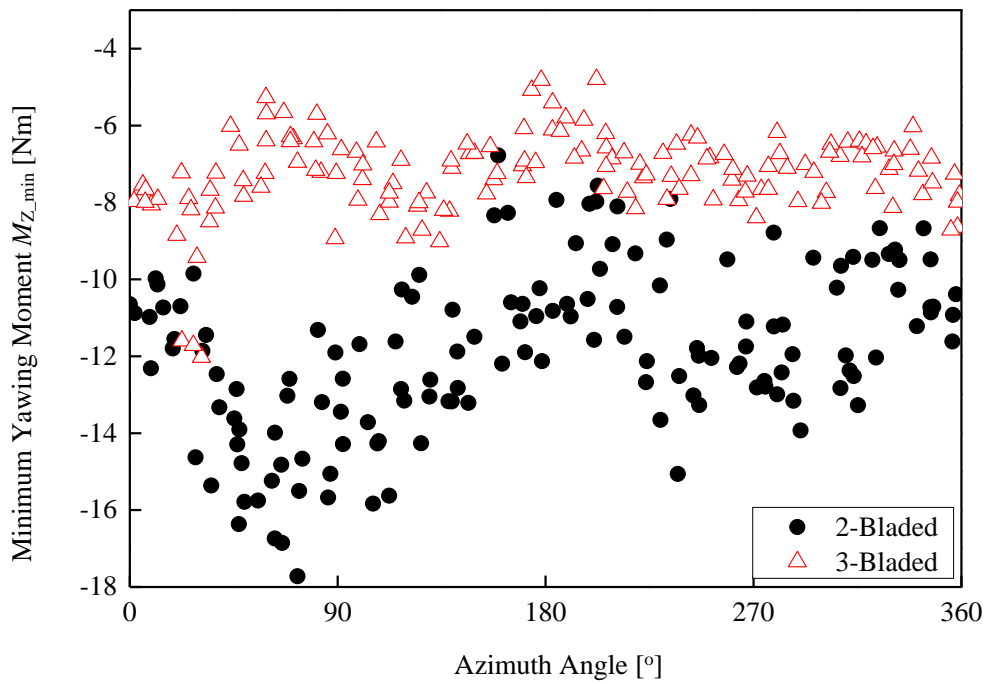


Fig. 5.9 Wind direction change and IEC EDC model in wind tunnel

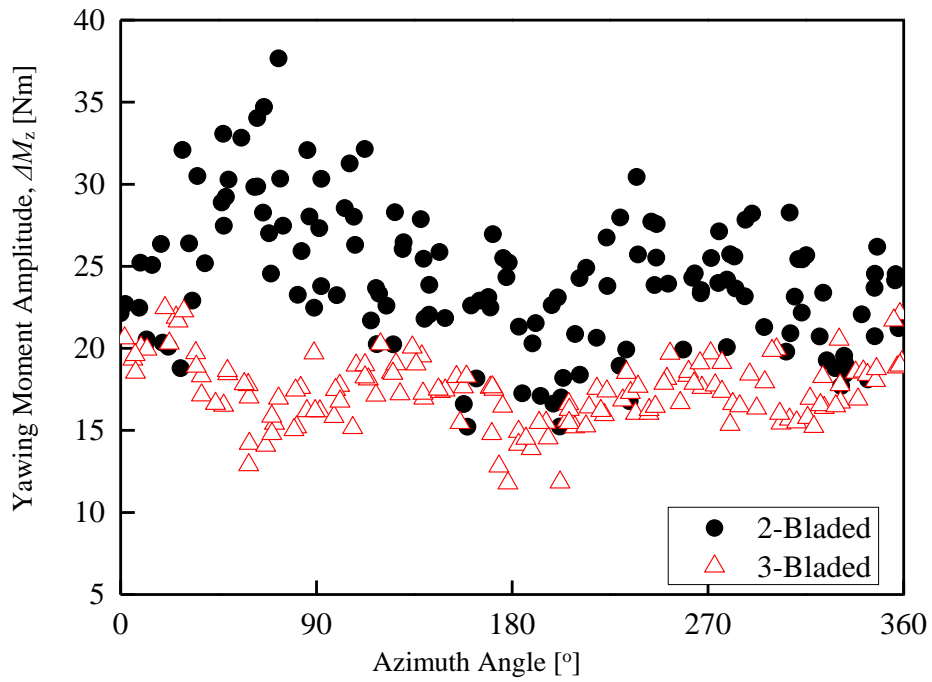


(a) The maximum yawing moment value for the azimuth angle



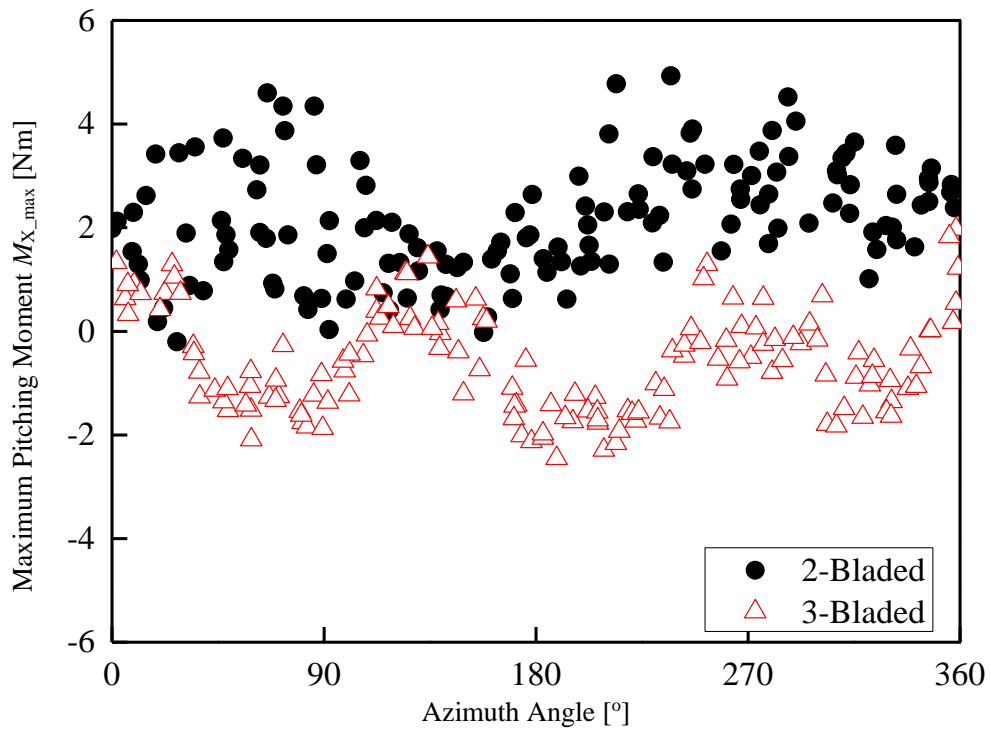
(b) The minimum yawing moment value for the azimuth angle

Fig. 5.10 Yawing moment fluctuation as the wind direction change



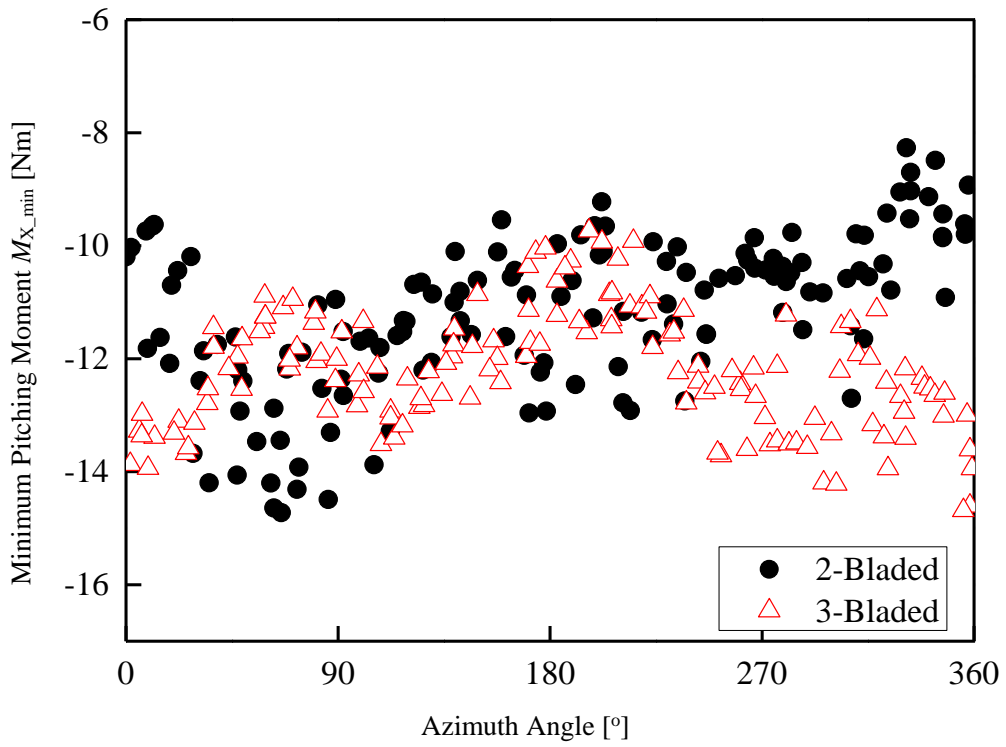
(c) Amplitude of the yawing moment at the azimuth angle

Fig. 5.10 Yawing moment fluctuation as the wind direction change

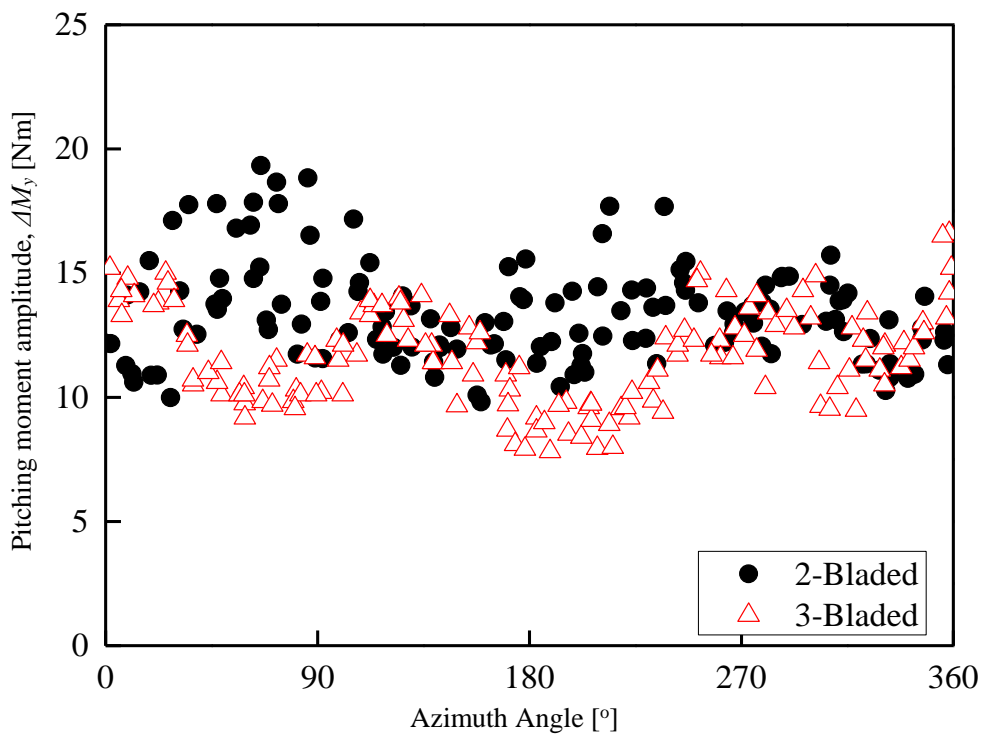


(a) The maximum pitching moment value at the azimuth angle

Fig. 5.11 Pitching moment fluctuation as the wind direction change



(b) The minimum pitching moment value at the azimuth angle



(c) Amplitude of the pitching moment at the azimuth angle

Fig. 5.11 Pitching moment fluctuation as the wind direction change

Table 5.1 Specifications of 10MW wind turbine and wind turbine model

	Unit	10 MW wind turbine	Wind turbine model
Rotor diameter	[m]	200	1.6
Hub height wind velocity	[m/s]	11	8
Wind direction change angle	[deg]	-28.2° ~ +28.2°	-14.1° ~ +14.1°
Extreme wind direction change time	[s]	6	0.066

Table 5.2 Position of 5 measured points on the rotor plane (seen from the upstream)

Position relative to rotor surface	$(x/R, z/R)$
Center	(0, 0)
Right end	(1, 0)
Left end	(-1, 0)
Upper end	(0, 1)
Lower end	(0, -1)

Chapter 6 Investigation of cyclic pitch control on HAWT

In this chapter, the experimental results of the cyclic pitch control method are discussed. The load and performance of HAWT were observed in the front inflow wind and the yawed inflow wind conditions. The first results are the effect of the collective pitch on the power and thrust coefficients. The next shows the experimental results about the effect of cyclic pitch on load of the model wind turbine in the front inflow wind. Finally, in the cyclic pitch control experiment, the tip speed ratio was kept constant in the case of the yawed inflow wind, the phase angle was divided into the two cases of $\xi = 0^\circ, 45^\circ, 90^\circ, 135^\circ$ and the $\xi = 30^\circ, 60^\circ, 120^\circ, 150^\circ$.

6.1 Experimental Apparatus and Conditions

6.1.1 Wind tunnel and model wind turbine

The experiment was carried out in the wind tunnel of Fluid Engineering Laboratory for Energy and Environment of Mie University, as shown in Fig. 4.1 (a).

The coordinate system of the wind tunnel is defined for the measurements, in which the x , y and z -axes are set in the mainstream, the lateral and the vertical directions, respectively as shown in Fig. 6.1 (b).

6.1.2 Model wind turbine

The model wind turbine is a two-bladed downwind horizontal axis wind turbine with the rotor diameter of $D = 1.6$ m and the hub height is 1.535m as seen in Fig. 6.1 (a). The rotor rotational speed is adjusted by a variable speed generator with the maximum of 1200 rpm. In this study, the rated rotational speed is set at 880 rpm and the mainstream wind velocity is 10 m/s. The blade is an Avistar airfoil. Fig. 6.1 (b) shows thrust force T , pitching moment M_X and yawing moment M_Z on the test wind turbine. The thrust force T is a component in the direction of the rotation axis of the force acting on the rotor plane. An elliptical nacelle cover is attached to the nacelle.

Fig. 6.2 (a) describes the definitions of the blade pitch angle and the rotor azimuth angle. The pitch angle of θ is defined as the angle between the chord line at blade tip and at the rotational plane, and the positive pitch angle when the leading edge of the blade inclines toward the upstream side. The azimuth angle is positive in the direction of the rotor rotation. The yaw angle is defined as the angle between the rotor axis and the wind direction, and the yaw angle is positive to the clockwise direction of the tower central axis seen from the sky.

6.1.3 Swash plate and pitch control actuator

Swash plate

The position of swash plate of the model wind turbine is shown in Fig. 6.2. The pitch angle change in the cyclic pitch control is given by Eq. (3.1). Fig. 6.3 shows the pitch angle change in the cyclic pitch control. The vertical axis presents the pitch angle. The horizontal axis is the azimuth angle. From this figure, the pitch angle is considered as a function of the azimuth angle. The change of the pitch angle amplitude a and phase angle ξ affect the shape of the pitch angle following the azimuth angle.

Fig. 6.4 exhibits the relationship between the swash plate displacement and the pitch angle change. In this figure, the pitch angle θ , the displacement amount of the swash plate σ_{SW} , the actuator position σ_A , and the average pitch angle b are presented. The cyclic pitch control is conducted with the averaged pitch angle of $b = 0^\circ$, the phase angle of $\xi = 0^\circ$, and the pitch angle amplitude of $a = 1^\circ$. The displacement amount of the swash plate is advanced by 50° in phase angle as compared with the pitch angle change. This is because there is a phase difference in the connection between the swash plate and the pitch lever for changing the pitch angle. Therefore, the pitch angle can periodically change by operating the displacement amount.

Pitch control actuator

The actuator which is used to control the pitch angle is a linear drive actuator. The relation between the actuator displacement and the pitch angle is geometrical relation. It means that the pitch angle is determined by actuator displacement through the structure of connected rod and connection point to the swash plate. The command values from the personal computer are sent to the actuator driver to control the pitch angle of the swash plate. The specifications and position of the pitch control actuator used in this experiment are shown in Table 6.1 and Fig. 6.2.

6.1.4 Experimental conditions

The effect of the pitch control was investigated in the stable wind condition, and the dynamic forces acting on entire wind turbine are measured by a 6-component balance. The stable wind condition was divided into two cases: the front wind and the yawed inflow wind.

Firstly, the collective pitch control test clarifies the relationship between the power coefficient and thrust coefficient for various pitch angles. In this test, the dynamic force generated by changing the pitch angle $\theta = -2^\circ$ to $+2^\circ$ and the optimal tip speed ratio $\lambda = 7.4$ was measured. In these experiments, the same measurement is performed even when the yaw angle $\varphi = -10^\circ, -5^\circ, 0^\circ, +5^\circ, +10^\circ$. Changing in wind speed and wind direction of the main flow wind alter the relative inflow wind of the rotor blades and affect the output performance of the wind turbine, therefore it is important to know effect of the change of wind speed and wind direction on the wind turbine characteristics. The relative inflow wind of the rotor blades is a combination of three vectors of rotational speed, main flow velocity, and reduced velocity. The angle of attack is the angle between the chord line and the relative inflow wind. The angle of attack varies with the entire span of the rotor blade due to the change in the pitch angle, and the fluid force acting on the blade is changed. As a result, the fluid force generated on the rotor plane can be changed. The pitch angle at the wind turbine output performance test and the steady pitch control test is constant at all azimuth angle positions.

Secondly, Table 6.2 presents experimental conditions for the cyclic pitch control experiment. Experiments are performed at the averaged pitch angle of 0° and the optimal tip speed ratio of $\lambda = 7.4$ with the mainstream wind velocity of 10.0 m/s. In this experiment, the dynamic forces are obtained by changing the phase angle of the pitch angle and modifying the pitch angle amplitude. In addition, the yaw angle is set to $\varphi = -5^\circ, 0^\circ, +5^\circ$ and the pitch angle amplitude is controlled at $-1^\circ \leq a \leq 1^\circ$ in the yawed inflow wind condition. In the cyclic pitch control experiment, the measurement data are focused on the wind turbine torque, the rotational speed, the thrust, the yawing moment and the pitching moment acting on the rotor centre. The periodic pitch change causes different dynamic forces at different azimuth angles and also generates different moments on the rotor plane.

6.2 Rotor Aerodynamic Load and Performance Characteristics for Front Inflow Wind

6.2.1 Steady pitch control

Fig. 6.5 shows the power coefficient curves for the pitch angle change. Mainstream wind velocity is $U = 10$ m/s. The vertical axis presents the power coefficient C_p . The horizontal axis is the tip speed ratio. From this figure, the maximum power coefficient decreases when the pitch angle increases or decreases from $\theta = 0^\circ$. The maximum power coefficient is obtained at the pitch angle of $\theta = 0^\circ$, and the tip speed ratio is $\lambda = 7.4$. Therefore, for an optimum operation of the model wind turbine, the tip speed ratio is set to $\lambda = 7.4$ and the pitch angle is $\theta = 0^\circ$.

In order to understand clearly this issue, Fig. 6.6 shows the fluid force acting on the blade element depending on the pitch angle change. For the small pitch angle as shown in Fig. 6.6 (a), the wind speed is constant. The magnitude of the lift and drag force in the blade element are determined by the angle of attack, and each direction is determined by the inflow angle. As shown in the figure, the inflow angle decreases as the tip speed ratio increases. The direction of the fluid force acting on the blade element faces the thrust direction as the tip speed ratio increases. At this time, the angle of attack of the blade decreases due to the increase of the tip speed ratio, and the lift coefficient increases. Also, the magnitude of lift and drag increases. From the above, the thrust increases as the tip speed ratio

increases. In addition, the angle of attack of the high tip speed ratio region is not in the stall region, and the lift coefficient linearly increases as the angle of attack decreases.

As shown in Fig. 6.6 (b), in the case of a large pitch angle, the angle of attack of the blade at the high tip speed ratio is large and the magnitude of the fluid force at the blade decreases. Therefore, the thrust coefficient in the high tip speed ratio region decreases as the pitch angle increases. In the case of the low tip speed ratio, the angle of attack is large and there is stall. Due to this stall, the lift coefficient in the low tip speed ratio region does not substantially change regardless of the tip speed ratio change.

Fig. 6.7 describes the thrust coefficient curves for the various pitch angle. The horizontal axis shows the tip speed ratio and the vertical axis is the thrust coefficient C_T . From this figure, the thrust coefficient C_T at each the pitch angle monotonically increases as the tip speed ratio increases. At any pitch angle θ , the increasing gradient of the thrust coefficient with respect to the increase in the tip speed ratio becomes gently on the high tip speed ratio side.

The relationship between the power coefficient under the optimal operation with the pitch angle in the steady pitch is seen in Fig. 6.8. The optimum operation tip speed ratio is $\lambda = 7.4$, and the pitch angle is changed from -2° to 2° with intervals of 1° . From this figure, the optimum pitch angle is $\theta = 0^\circ$ and the maximum power coefficient is $C_P = 0.405$. The power coefficient also decreases when the pitch angle is out of the optimum.

Fig. 6.9 shows the relationship between the thrust coefficient and the pitch angle for the optimum tip speed ratio. The horizontal axis represents the pitch angle θ , and the vertical axis is the thrust coefficient C_T . It can be seen from the figure that the thrust coefficient C_T decreases as the pitch angle increases. When the pitch angle is made larger than the optimum, the angle of attack of the blade becomes small. Therefore, the lift decreases and the thrust decreases. If the pitch angle is set smaller than the optimum, the angle of attack of the blade becomes larger. Therefore, the lift of the blade increases and the thrust coefficient increases. By varying the pitch angle, the lift generated in the blade can be increased or decreased, and the magnitude of the thrust can be changed by increasing or decreasing the lift. From this, it is possible to control the magnitude of thrust by steady pitch control.

6.2.2 Cyclic pitch control

Fig. 6.10 and Fig. 6.11 exhibit the power coefficient curves for the cyclic pitch control of the test wind turbines at $\xi = 0^\circ, 45^\circ, 90^\circ, 135^\circ$ and $\xi = 30^\circ, 60^\circ, 120^\circ, 150^\circ$. The horizontal axis is the pitch angle amplitude a , and the vertical axis is the power coefficient C_P . When the pitch angle amplitude is 0° , there is no periodic change in the pitch angle and the same wind turbine operation state is set, the optimum power coefficient $C_P = 0.405$. As can be seen from two figures, the power coefficient almost stable as the pitch angle amplitude a increases or decreases in each phase angle ξ . However, the cases in the Fig. 6.10 have a little smaller of the maximum power coefficients than the cases in the Fig 6.12. The peak of the power coefficient is obtained at different pitch angle amplitude. This is because the azimuth angle position at which the maximum pitch angle and the minimum pitch angle are reached by the cyclic pitch control differs according to the phase angle ξ . Therefore, the inflow wind acting on the rotor plane is changed due to the tower shadow effect.

Similarly, the thrust coefficient curves for cyclic pitch control of the test wind turbines at $\xi = 0^\circ, 45^\circ, 90^\circ, 135^\circ$ and $\xi = 30^\circ, 60^\circ, 120^\circ, 150^\circ$ is shown in Fig 6.12 and Fig. 6.13. The horizontal axis represents the pitch angle variation amplitude a , and the vertical axis is the thrust coefficient C_T . As shown in the figures, the thrust coefficient C_T is kept almost constant with respect to the change of the change amplitude a . This is because the average pitch angle is constant at each pitch angle amplitude a and is represented by the average value of thrust on the rotor plane. Evaluating the instantaneous value of the thrust on the rotor plane as the pitch angle varies periodically, the angle of attack of the blade fluctuates, so it is considered that the thrust changes with the azimuth angle position of the rotor plane. Moreover, thrust is thought to be influenced by the change of the inflow wind by the tower wake.

Fig. 6.14 and Fig 6.15 exhibit the relation between the pitch angle amplitude and the pitching moment coefficient C_{M_x} with the phase angles of $\xi = 0^\circ, 45^\circ, 90^\circ, 135^\circ$ and $\xi = 30^\circ, 60^\circ, 120^\circ, 150^\circ$, respectively. Fig. 6.16 and Fig 6.17 show the relation between the pitch angle amplitude and the yawing moment coefficient C_{M_z} with the phase angles of $\xi = 0^\circ, 45^\circ, 90^\circ, 135^\circ$ and $\xi = 30^\circ, 60^\circ, 120^\circ, 150^\circ$. In these figures, the horizontal axis represents the pitch angle amplitude a , and the vertical axis is the pitching moment coefficient C_{M_x} and the yawing moment

coefficient C_{M_z} , respectively. It can be seen that C_{M_x} and C_{M_z} linearly change with respect to the pitch angle amplitude a . Thus, by adjusting the pitch angle amplitude a , the magnitude of the moment acting on the rotor plane can be controlled. From Fig. 6.14 and Fig. 6.15, at the phases of $\xi = 0^\circ, 120^\circ, 135^\circ$ and 150° , the gradient of these lines are lower than other lines. In addition, C_{M_x} and C_{M_z} are determined by two variables, the phase ξ and the pitch angle amplitude a . Therefore, by setting the phase ξ and the pitch angle amplitude a , the magnitude and direction of the moment can be arbitrarily controlled. Also, C_{M_x} and C_{M_z} are not 0 at the pitch angle amplitude $a = 0^\circ$. This is thought to be due to the influence of the flow field of the downstream of the tower of the test wind turbine on the rotor plane and the zero point offset at the 6-component balance.

Next, to understand the effect of the change of the pitch angle amplitude on the pitching moment coefficient and the yawing moment coefficient, the two directions of the moment coefficients are compared with the change of the pitch angle amplitude at the each phase angle ξ . The corrected pitching moment coefficient $C_{M_x}'(\xi, a)$ and the corrected yawing moment coefficient $C_{M_z}'(\xi, a)$ show the fluctuation of C_{M_x} and C_{M_z} when the pitch angle amplitude changes. They are defined by the values of C_{M_x} and C_{M_z} at the pitch angle amplitude of $a = 0^\circ$ as the origin value. The $C_{M_x}'(\xi, a)$ and $C_{M_z}'(\xi, a)$ are obtained by subtracting the values of C_{M_x} and C_{M_z} at the pitch angle amplitude of $a = 0^\circ$. The following Eqs. (6.1) and (6.2) of $C_{M_x}'(\xi, a)$, $C_{M_z}'(\xi, a)$ are shown as follows:

$$C_{M_x}'(\xi, a) = C_{M_x}(\xi, a) - C_{M_x}(\xi, 0) \quad (6.1)$$

$$C_{M_z}'(\xi, a) = C_{M_z}(\xi, a) - C_{M_z}(\xi, 0) \quad (6.2)$$

where $C_{M_x}(\xi, a)$ and $C_{M_z}(\xi, a)$ show the experimental value at the pitch angle phase ξ and the pitch angle amplitude a .

Fig. 6.18 and Fig 6.19 exhibit the relation between $C_{M_x}'(\xi, a)$ and $C_{M_z}'(\xi, a)$ with the phase angles of $\xi = 0^\circ, 45^\circ, 90^\circ, 135^\circ$ and $\xi = 30^\circ, 60^\circ, 120^\circ, 150^\circ$. The horizontal axis of the figure is the corrected pitching moment coefficient $C_{M_x}'(\xi, a)$ and the vertical axis is the corrected yawing moment coefficient $C_{M_z}'(\xi, a)$. From the figure, C_{M_x}' , C_{M_z}' at an arbitrary phase a changes on a straight line having a certain slope with respect to the change of change amplitude a .

The slope of the straight line is defined as the moment axis azimuth angle ψ_M , and it is calculated by $C_{M_x}'(\xi, a)$ and $C_{M_z}'(\xi, a)$ as the following Eq. (6.3).

$$\psi_M(\xi, a) = \tan^{-1} \left[\frac{-C_{M_x}'(\xi, a)}{C_{M_z}'(\xi, a)} \right] \quad (6.3)$$

Here, like the azimuth angle, the moment axis azimuth angle ψ_M is set 0° when the rotor vertical direction is upward and the rotor rotation direction is a positive value.

Fig. 6.20 and 6.21 shows the relationship between the pitch angle change amplitude a of $\xi = 0^\circ, 45^\circ, 90^\circ, 135^\circ$ and $\xi = 30^\circ, 60^\circ, 120^\circ, 150^\circ$ and the synthetic moment coefficient $C_M(\xi, a)$. In the figure, the horizontal axis represents the pitch angle amplitude a and the vertical axis is the synthetic moment coefficient $C_M(\xi, a)$. In addition, in the region where the change amplitude a is negative, since the direction of the moment is opposite, the value of $C_M(\xi, a)$ is negative. From the figure, the magnitude of the composite moment greatly depends on the change of the pitch angle amplitude a in the range of $a = -1^\circ$ to 1° , but it can be said that it is almost not influenced by the phase ξ . There is a slight difference occurs in $C_M(\xi, a)$ due to phase ξ is considered to be non-uniform inflow velocity in the rotation plane. This is because the decelerated flow of the tower downstream flows into the rotor plane, and the wind speed flowing into the rotor plane changes at the azimuth angle position.

Considering the wind turbine load fluctuation due to rotor blade aerodynamic load during the cyclic pitch control. The measurement result of the six-component force balance used here is data that is not subjected to load

point correction. Fig. 6.22 shows the variation of the yawing moment M_Z occurring at the top of the tower with respect to the azimuth angle position of the rotor blade during cyclic pitch control. The horizontal axis of the figure is the azimuth angle ψ , and the vertical axis is the yawing moment M_Z . The figure shows the results of the pitch angle phase $\xi = 45^\circ$ and the pitch angle amplitude $a = -1^\circ, 0^\circ, 1^\circ$. From the figure, by applying cyclic pitch control, the phase and amplitude of the yawing moment change. In the case of $a = 0^\circ$, the pitch angle does not change periodically and shows the variation of the yawing moment of the steady pitch at the optimum pitch angle. The yawing moment of $a = 0^\circ$ shows the maximum value $M_Z = 14.90$ [Nm] at the azimuth angle $\psi = 230.0^\circ$, and when the azimuth angle $\psi = 134.9^\circ$, the minimum value $M_Z = -16.42$ [Nm]. The amplitude of the yawing moment of the cyclic pitch control at $a = 1^\circ$ is smaller than $a = 0^\circ$ and $a = -1^\circ$. From this, it is possible to suppress the load fluctuation on the yaw system by appropriately performing the cyclic pitch control.

Fig. 6.23 and 6.24 show the variation of the yawing moment due to the phase angle change. The horizontal axis of the figure is the azimuth angle ψ , and the vertical axis is the yawing moment M_Z . Fig. 6.23 shows the result of the pitch angle phase $\xi = 0^\circ, 45^\circ, 90^\circ, 135^\circ$ and the pitch angle amplitude $a = -1^\circ$. The azimuth angle position and amplitude change instantaneous yawing moment and showing maximum and minimum value by the phase angle ξ . The amplitude of yawing moment takes the maximum value at the phase $\xi = 45^\circ$, and the minimum value at $\xi = 135^\circ$. Fig. 6.24 shows the results of pitch angle phase $\xi = 0^\circ, 45^\circ, 90^\circ, 135^\circ$ and the pitch angle amplitude $a = +1^\circ$. In the case of the pitch angle amplitude $a = 1^\circ$, the magnitude of the yawing moment amplitude takes the maximum value at the pitch angle phase $\xi = 135^\circ$, the minimum value at $\xi = 0^\circ$.

Fig. 6.25 indicates the fluctuation of spectra calculated from fast Fourier transform (FFT) based on the data of the Fig. 6.23. The horizontal axis of the figure is the frequency f , and the vertical axis is the power spectrum. From this figure, the frequency analysis results are investigated with the pitch angle phases of $\xi = 0^\circ, 45^\circ, 90^\circ, 135^\circ$ at the pitch angle amplitude of $a = -1^\circ$. For $\xi = 0^\circ$, the first peak frequency is $f = 14.7$ Hz as seen from a low frequency. It is considered as the rotational frequency of the rotor blade. The second peak frequency is $f = 29.3$ Hz, it is shown as the effect of number of blade on the rotational frequency. In addition, for $\xi = 45^\circ, 90^\circ, 135^\circ$, the fluctuations of the frequency are a good agreement with the case of $\xi = 0^\circ$. From above results, the fluctuations of the frequency are independent of the angle phases in the cyclic pitch control.

Similarly, the frequency analysis is considered at the pitch angle amplitude of $a = 1^\circ$ as shown in Fig. 6.26. From this figure, the first peak frequency is $f = 14.7$ Hz and the second peak frequency is $f = 29.3$ Hz as seen from a low frequency at the pitch angle phases of $\xi = 0^\circ, 45^\circ, 90^\circ$ and 135° . Furthermore, from the Fig. 6.24, when the pitch angle phase increases, the maximum and minimum values of the yawing moment responded to the azimuth angle positions also increase. Therefore, in the cyclic pitch control, the angle phase of the yawing moment can arbitrarily set. And the magnitude of the yawing moment can be set by changing the pitch angle amplitude. Therefore, when the periodic yawing moment is generated in the nacelle, the yawing moment of opposite phase can be generated by the cyclic pitch control and the load applied on the yaw system can be reduced. From the above explanation, the load of vibration on the wind turbine can be reduced.

6.3 Rotor Aerodynamic Load and Performance Characteristics for Yawed Inflow Wind

6.3.1 Yawed inflow wind condition

When the floating offshore wind turbine operates on the ocean, excepting the main wind direction, there are the yawed wind, the storm and high turbulence wind. In this study, the yawed wind condition was focused on consideration. Therefore, it is important to clarify the wind turbine characteristics against yawed wind condition. The pitch angle control was applied to the wind turbine in the yawed inflow wind state, and the fluid force acting on the rotor plane was measured with a 6-component balance.

The angle of attack is considered at the yawed wind condition. It is assumed that the rotor blade rotation axis is inclined relative to the mainstream inflow velocity U as following:

$$U_r = U \sin\varphi \quad (6.4)$$

$$U_a = U \cos \varphi \quad (6.5)$$

where U_r is the horizontal velocity component in the main rotor blade rotation plane, U_a is the axial velocity component.

Fig. 6.27 describes the variation of the angle of attack at each yaw angle. The horizontal axis exhibits the azimuth angle ψ and the vertical axis is the angle of attack α . The figure shows the change in the angle of attack at the blade tip position when the optimal tip speed ratio $\lambda = 7.4$. The angle of attack at yaw angle $\varphi = 0^\circ$ is constant since it is not affected by the azimuth angle. In addition, the angle of attack at each yaw angle has the minimum value at the azimuth angle of $\psi = 0^\circ$ and the maximum value at the azimuth angle of $\psi = 180^\circ$. From Eqs. (6.4) and (6.5), the increasing of the horizontal direction velocity component and the decreasing of the axial velocity component in the rotor blade rotation plane of the main flow velocity are small at the yaw angles of $\varphi = \pm 5^\circ, \pm 10^\circ$. It is worth noting that the variations of the angle of attack are also small. From the above reasons, the change of the optimal tip speed ratio at yaw angle $\varphi = \pm 5^\circ, \pm 10^\circ$ is small. Also, as the yaw angle increases, the change of the angle of attack becomes larger.

Using the rotor blade angular velocity ω and the rotor blade azimuth angle ψ , the tip velocity component U_v flowing into the blade element at the blade tip position can be expressed by the following equation:

$$U_v = R\omega + U_r \cos \psi \quad (6.6)$$

Therefore, the angle of attack α in the cross section at the tip position can be expressed by the following:

$$\alpha = \tan^{-1} \left(\frac{U_a}{U_v} \right) - \theta \quad (6.7)$$

Fig. 6.28 shows the variations of the angle of attack with each azimuth angle position. At the azimuth angle from $\psi = 270^\circ$ to 90° , the rotor blade rotates to the windward direction with respect to the main flow, the relative circumferential velocity increases in accordance with the blade element and the angle of attack of the blade decreases with the increase of the azimuth angle. On the contrary, at the azimuth angle from $\psi = 90^\circ$ to 270° , the rotor blade rotates in the leeward direction according to the main flow, the relative tip velocity decreases and the angle of attack of the blade increases with the increase of the azimuth angle.

Fig. 6.29 represents the angle of attack for different change amplitude a when the yaw angle is set to $\varphi = -5^\circ$. The horizontal axis displays the azimuth angle ψ and the vertical axis is the angle of attack α . This figure shows the change in the angle of attack at the tip position at the optimal tip speed ratio $\lambda = 7.4$ and the phase of $\xi = 0^\circ$. As shown in the figure, the angle of attack at the change amplitude $a = 0^\circ$ becomes the maximum value at $\xi = 0^\circ$ with the change of the azimuth angle, and becomes the minimum value at $\psi = 180^\circ$. As the absolute value of the change amplitude a increases, the change in the angle of attack becomes larger and departs from the optimum angle of attack $\alpha = 7.72$ at the yaw angle $\varphi = 0^\circ$. Accordingly, as the absolute value of the change amplitude a increases, the power coefficient decreases. Relation between the pitch angle and the azimuth angle is described in Fig. 6.30 with the phase angle $\xi = 0^\circ, 45^\circ, 90^\circ, 135^\circ$ and $\xi = 30^\circ, 60^\circ, 120^\circ, 150^\circ$ at average pitch angle $b = 0^\circ$. Depending on the azimuth angle change, the pitch angle is controlled periodically. Specifically, according to Eq. (3.3), the pitch angle is a cosine function of the azimuth angle. Therefore, during on wind turbine operation, the pitch angle is adjusted periodically with respond to the azimuth angle change.

6.3.2 Steady pitch control

Fig. 6.31 and Fig. 6.32 exhibit the power coefficient and the thrust coefficient curve for the yaw angle modification in the yawed inflow wind condition. The maximum power coefficient obtains $C_P = 0.405$ at the yaw angle of $\varphi = 0^\circ$ as shown in Fig 6.31. The value of the maximum power coefficient decreases as the yaw angle increases or decreases. However, the optimum tip speed ratio for maximum power coefficient is constant regardless of the yaw angle change.

From Fig. 6.32, the thrust coefficient C_T at each the yaw angle increases monotonically when the tip speed ratio λ increases. Due to the horizontal velocity component of the mainstream wind velocity occurring in the yawed inflow wind condition, the angle of attack periodically changes with one rotation of the rotor blades. The change of angle of attack increases when the yaw angle increases. Furthermore, the average value of the angle of attack decreases as the yaw angle increases. Therefore, as the yaw angle increases, the thrust coefficient decreases, and the gradient of the thrust coefficient with respect to the tip speed ratio becomes moderate. In addition, due to the influence of the flow field of the tower wake, it shows different directions depending on whether the yaw angle is positive or negative.

Fig. 6.33 indicates the relationship between the power coefficient and the pitch angle in the yawed inflow wind condition. The optimum tip speed ratio is $\lambda = 7.4$. In the case of the yaw angle of $\varphi = 0^\circ$, the pitch angle is changed from -1° to 1° with intervals of 1° . When the yaw angle of $\varphi = \pm 5^\circ$ and $\pm 10^\circ$, the pitch angle is varied every 0.5° from -1° to 1° . From this figure, the optimum value of the pitch angle is $\theta = 0^\circ$ and the maximum power coefficient is $C_P = 0.405$. No significant change is seen in the power coefficient at yaw angle of $\varphi = \pm 5^\circ$ compared with the power coefficient of the yaw angle of $\varphi = 0^\circ$. However, the power coefficient at the yaw angle of $\varphi = \pm 10^\circ$ becomes smaller as compared with the power coefficient of the yaw angle of $\varphi = 0^\circ$. In addition, the power coefficient decreases from the optimum pitch angle of $\theta = 0^\circ$ to a smaller value in the yawed inflow condition.

6.3.3 Cyclic pitch control

6.3.3.1 Power coefficient and thrust coefficient characteristics

Fig. 6.34 and Fig. 6.35 depict the power coefficient curves against the pitch angle amplitude at the different phases of the pitch angle of $\xi = 0^\circ, 45^\circ, 90^\circ, 135^\circ$ and $\xi = 30^\circ, 60^\circ, 120^\circ, 150^\circ$, respectively. The horizontal axis represents the pitch angle amplitude a , the vertical axis represents the power coefficient C_P . From two figures, the power coefficient almost stable as the pitch angle amplitude a increases. The pitch angle amplitude of $a = 0^\circ$, the operation condition is the constant pitch angle. In addition, as shown in Fig. 6.34, the power coefficient obtains the maximum value $C_P = 0.405$ at the $a = -0.6^\circ$ and $\xi = 135^\circ$. Similarly, in the Fig. 6.35, the power coefficient obtains the maximum value $C_P = 0.406$ at the $a = -0.8^\circ$ and $\xi = 120^\circ$. From these above results can see that the pitch angle amplitude a indicates the maximum power coefficient variation depending on each phase angle of ξ . This is because the azimuth angle positions seeing the maximum and minimum pitch angle are different according to the phase angle of ξ . The relative inflow wind velocity which flows into the blade is modified following each the azimuth angle position.

Fig. 6.36 and Fig. 6.37 display the relationship between the thrust coefficient and the pitch angle amplitude at the phases of $\xi = 0^\circ, 45^\circ, 90^\circ, 135^\circ$ and $\xi = 30^\circ, 60^\circ, 120^\circ, 150^\circ$, respectively. The horizontal axis indicates the pitch angle amplitude a , and the vertical axis indicates the thrust coefficient, C_T . From these figures, the thrust coefficient C_T slightly changes with respect to the pitch angle amplitude a in the different phase angles of ξ . Because the azimuth angle position at which the maximum and minimum pitch angles are reached depending on the phase angle of ξ . From the above result, it is considered that the thrust coefficient slightly changes as a function of the phase angle of ξ , due to the average value of the angle of attack of the blades that changes at all azimuth angles.

6.3.3.2 Rotor blade aerodynamic load characteristics

In this section, the aerodynamic load acting on the rotor plane is considered when the cyclic pitch control is applied under the yawed inflow wind condition. The cyclic pitch angle change causes different fluid forces at different azimuth angles, and generates a moment on the rotor plane. In the cyclic pitch control experiment, the phase angle and the pitch angle amplitude are changed. The direction and magnitude of the moment caused by the fluid force generated on the rotor plane are evaluated.

Fig. 6.38 and Fig. 6.39 show the relationship between the pitch angle amplitude a of the phases $\xi = 0^\circ, 45^\circ, 90^\circ, 135^\circ$ and $\xi = 30^\circ, 60^\circ, 120^\circ, 150^\circ$ with the pitching moment coefficient C_{Mx} , respectively. Fig. 6.40 and Fig. 6.41 show the relationship between the pitch angle amplitude a of the phases $\xi = 0^\circ, 45^\circ, 90^\circ, 135^\circ$ and $\xi = 30^\circ, 60^\circ, 120^\circ, 150^\circ$ with the yawing moment coefficient C_{Mz} , respectively. In these figures, the horizontal axes represent the pitch angle amplitude a and the vertical axes are the pitching moment coefficient C_{Mx} and the yawing moment coefficient C_{Mz} , respectively. In these figures, it can be seen that C_{Mx} and C_{Mz} linearly change with respect to the pitch angle amplitude a . This can prove that they are possible control the magnitude of the moment acting on the rotor plane by adjusting the pitch angle amplitude of the cyclic pitch control in the yawed inflow wind condition. In addition, the pitching moment coefficient C_{Mx} is not value of 0 at the pitch angle amplitude $a = 0^\circ$. This is because the influence of the downstream wind of the tower (the tower shadow effect) of the test wind turbine flows into the rotor plane.

Combine the magnitude of the moments acting around the axis, the synthetic moment coefficient $C_M(\xi, a)$ is shown in the following Eq. (6.8).

$$C_M(\xi, a) = \sqrt{C_{Mx}'(\xi, a)^2 + C_{Mz}'(\xi, a)^2} \quad (6.8)$$

Fig. 6.42 and 6.43 show the relationship between the pitch angle change amplitude a of $\xi = 0^\circ, 45^\circ, 90^\circ, 135^\circ, \xi = 30^\circ, 60^\circ, 120^\circ, 150^\circ$ and the synthetic moment coefficient $C_M(\xi, a)$. In the figures, the horizontal axis represents the pitch angle amplitude a and the vertical axis is the synthetic moment coefficient $C_M(\xi, a)$. In addition, in the region where the pitch angle amplitude a is negative, since the direction of the moment is opposite, the value of $C_M(\xi, a)$ is negative. From the figure, the magnitude of the synthetic moment greatly depends on the change of the pitch angle amplitude a in the range of $a = -1^\circ$ to 1° , so it can be said that it is almost not influenced by the phase ξ . There is a slight difference occurred in $C_M(\xi, a)$ due to the phase angle ξ is considered to be non-uniform inflow velocity in the rotation plane. This is because the decelerated flow of the tower downstream flows into the rotor plane, and the wind speed flowing into the rotor plane changes at the azimuth angle position.

Fig. 6.44 and Fig. 6.45 indicates the relation of $C_{Mx}'(\xi, a)$ and $C_{Mz}'(\xi, a)$ at the phases of $\xi = 0^\circ, 45^\circ, 90^\circ, 135^\circ$ and $\xi = 30^\circ, 60^\circ, 120^\circ, 150^\circ$ for the cyclic pitch control. The horizontal axis is the corrected pitching moment coefficient $C_{Mx}'(\xi, a)$, and the vertical axis is the corrected yawing moment coefficient $C_{Mz}'(\xi, a)$. From this figure, the C_{Mx}' and C_{Mz}' at the arbitrary phase of ξ alter on a straight line with a certain slope with respect to the change of the pitch angle amplitude a .

In addition, by adding a point of the moment coefficient of the optimum operating condition in the front inflow wind condition into the Fig. 6.46 to compare with fluctuation of the rotor aerodynamic load in the yawed inflow wind condition. The brown plot in this figure is the moment coefficient of the optimum operating condition in the case of the front inflow wind condition. Because of the yawed inflow wind condition, the load acting on the rotor plane increases. In order to decrease the load on the rotor plane, the pitch angle is changed by the phase angle responding to the azimuth angle. Specifically, as can be seen from this figure, the moment coefficient of the optimum operating condition in the front inflow wind condition equals the averaged value of the aerodynamic load acting on the rotor plane in the yawed inflow wind condition at phase angle of $\xi = 60^\circ$. From the above result, it is possible to reduce the aerodynamic load acting on the blade during one rotation.

Fig. 6.47 describes the relationship between the azimuth angle of the rotor blades and the yawing moment M_z . In this figure, the horizontal axis shows the azimuth angle ψ , and the vertical axis is the yawing moment coefficient

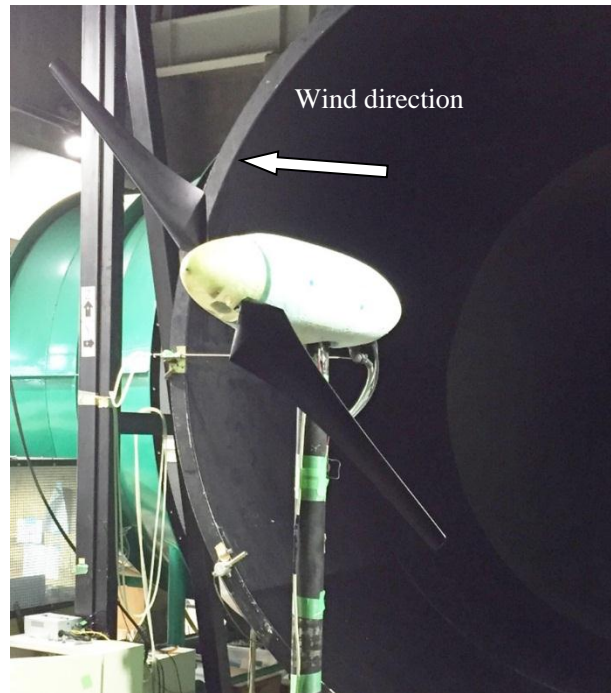
M_z . This figure also describes the results of the pitch angle phase of $\xi = 45^\circ$ and the pitch angle amplitude of $a = -1^\circ, 0^\circ$ and 1° . As shown in this figure, the phase angle and the magnitude of the yawing moment change by applying the cyclic pitch control. In the case of $a = 0^\circ$, the pitch angle does not change periodically and shows the variation of the yawing moment of the steady pitch at the optimum pitch angle.

At the pitch angle amplitude of $a = 0^\circ$, the yawing moment shows the maximum value of $M_z = 16.22$ Nm at the azimuth angle of $\psi = 58.2^\circ$, and when the azimuth angle $\psi = 155.2^\circ$, the minimum value of $M_z = -15.39$ Nm. This fluctuation is the effect on the vibration of the tower due to the rotation of the rotor blades. When the cyclic pitch control is performed with the phase angle of $\xi = 45^\circ$ and at the pitch angle amplitude of $a = -1^\circ$, the yawing moment acting on the rotor plane increases and the fluctuation also increases. When the cyclic pitch control is performed with the variation amplitude of $a = 1^\circ$, the yawing moment acting on the rotor plane decreases and its fluctuation also decreases. The fluctuation amplitude of the yawing moment at $a = 1^\circ$ is smaller than at $a = -1^\circ$, and higher than at $a = 0^\circ$. From this, it is possible to suppress the load fluctuation on the yaw system by appropriately performing the cyclic pitch control.

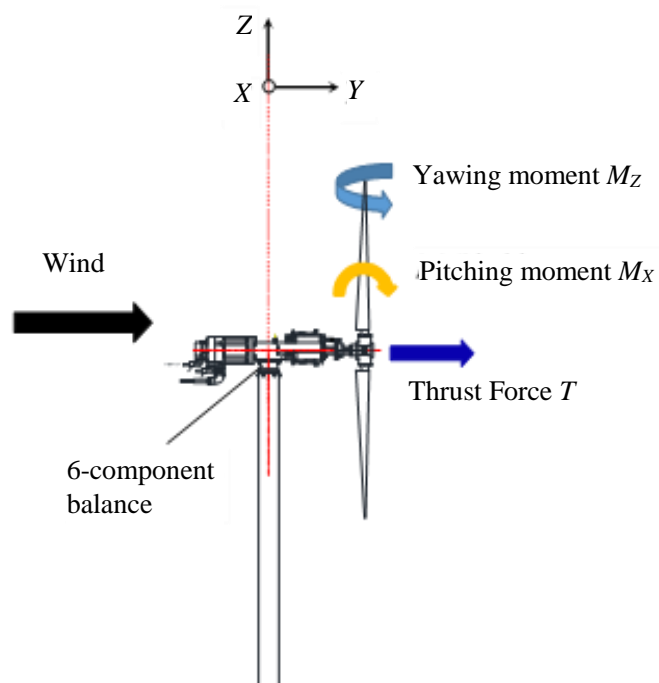
Fig. 6.48 and Fig. 6.49 show the variation of the yawing moment due to the difference of the phase angle. The horizontal axes of the two figures are the azimuth angle ψ , and the vertical axes are the yawing moment M_z . Fig. 6.48 indicates the result of the pitch angle phases of $\xi = 0^\circ, 45^\circ, 90^\circ$ and 135° and the pitch angle amplitude $a = -1^\circ$. The yawing moment changes instantaneously when modifying the azimuth angle position. The yawing moment presents the maximum and minimum values by the phase angle of ξ . The magnitude of the yawing moment has the maximum value at the phase angle of $\xi = 0^\circ$ and the minimum value at $\xi = 135^\circ$. Fig. 6.49 shows the result of the pitch angle phases of $\xi = 0^\circ, 45^\circ, 90^\circ$ and 135° and the pitch angle amplitude of $a = 1^\circ$. The magnitude of the yawing moment has the maximum value at the pitch angle phase of $\xi = 135^\circ$ and the minimum value of $\xi = 0^\circ$.

Fig. 6.50 indicates the fluctuation of spectra calculated from fast Fourier transform (FFT) based on the data of the Fig. 6.48. The frequency analysis result at the pitch angle amplitude $a = -1^\circ$. As can be seen from this figure, in each ξ , the first peak frequency seen from the low frequency is $f = 14.7$ Hz, and the second peak frequency is $f = 29.3$ Hz. In addition, the frequency analysis is performed based on the data in Fig. 6.49, and the results are shown in Fig. 6.51. The figure describes the frequency analysis result at the pitch angle amplitude $a = +1^\circ$. From this figure, in each ξ , the first peak frequency seen from the low frequency is $f = 14.7$ Hz, and the second peak frequency is $f = 29.3$ Hz. The peak of the frequency affects the rotation speed of the rotor blade, and the size of the spectrum affects the change of the working fluid force. The influence of this fluid force is due to the variation of the angle of attack under the yawed inflow wind and the cyclic pitch control. Therefore, it is considered the vibration acting on the wind turbine changes with these conditions.

Thus, in the cyclic pitch control, the phase of the yawing moment can be arbitrarily controlled. Furthermore, in the cyclic pitch control, the magnitude of the yawing moment can be controlled by changing the pitch amplitude. Then, when the periodic yawing moment is generated between the nacelle and tower, the yawing moment of the opposite phase can be generated by the cyclic pitch control, and the load applied to the yaw system can be reduced. From the above explanations, the possibility of reducing the load of vibration on the wind turbine has been shown.

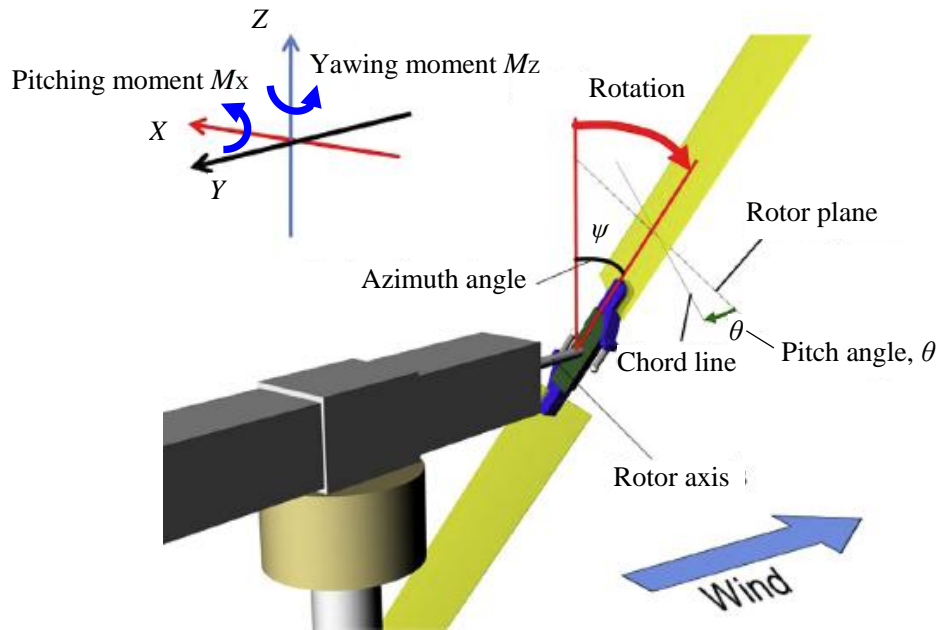


(a) Two-bladed downwind wind turbine model (seen from back side)

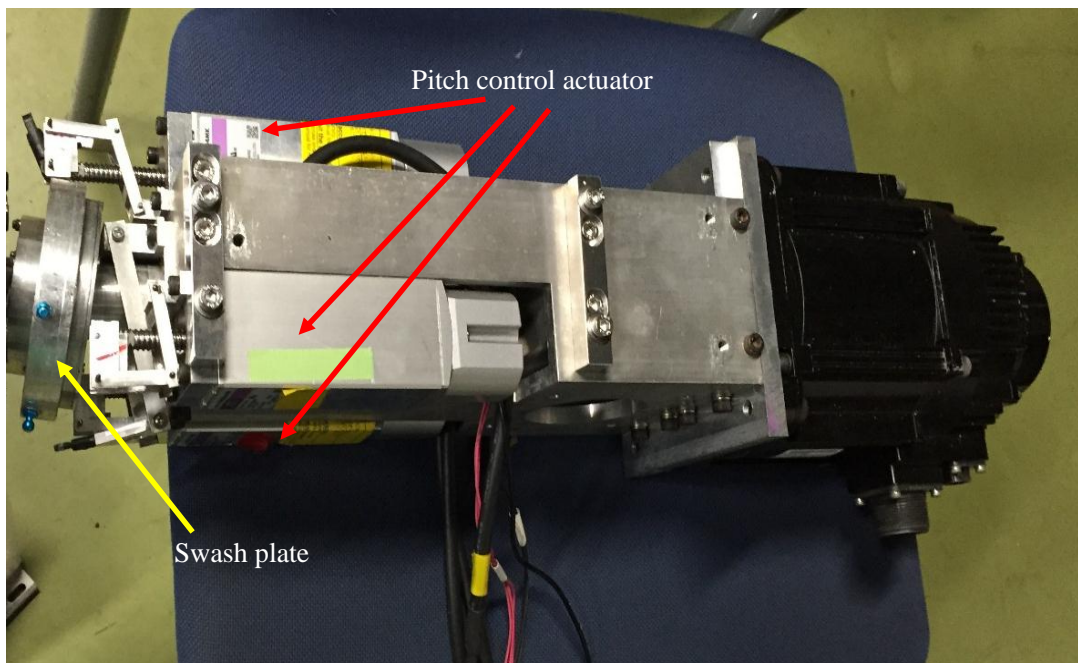


(b) Measurement elements on model wind turbine

Fig. 6.1 Model wind turbine and measurement elements



(a) Definitions of blade pitch angle and azimuth angle



(b) Picture of pitch control actuator and swash plate

Fig. 6.2 Picture of pitch control actuator and swash plate

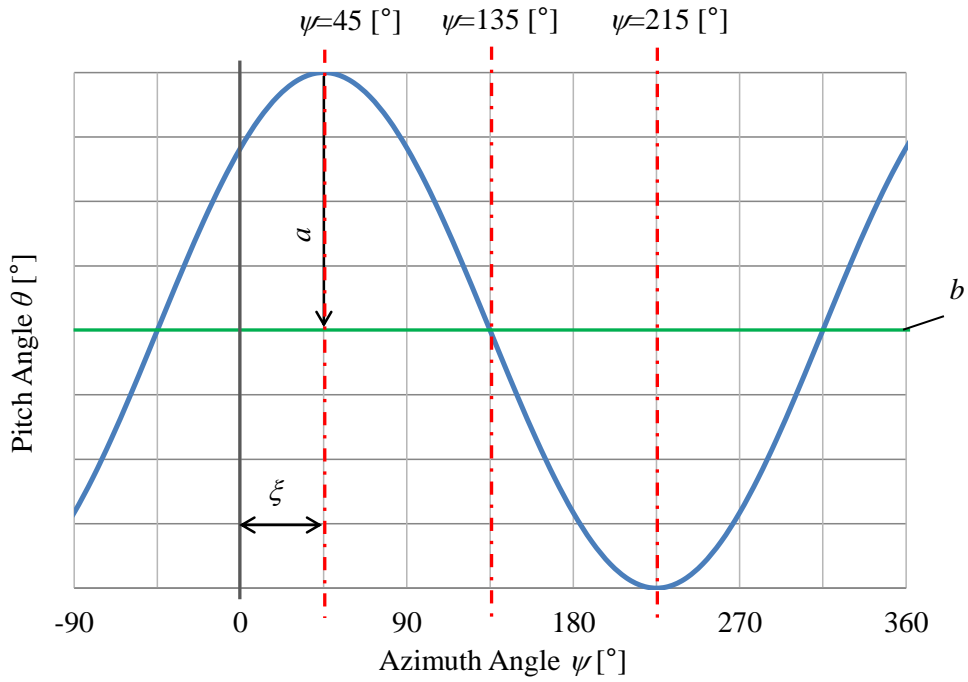


Fig. 6.3 Change in pitch angle in cyclic pitch control

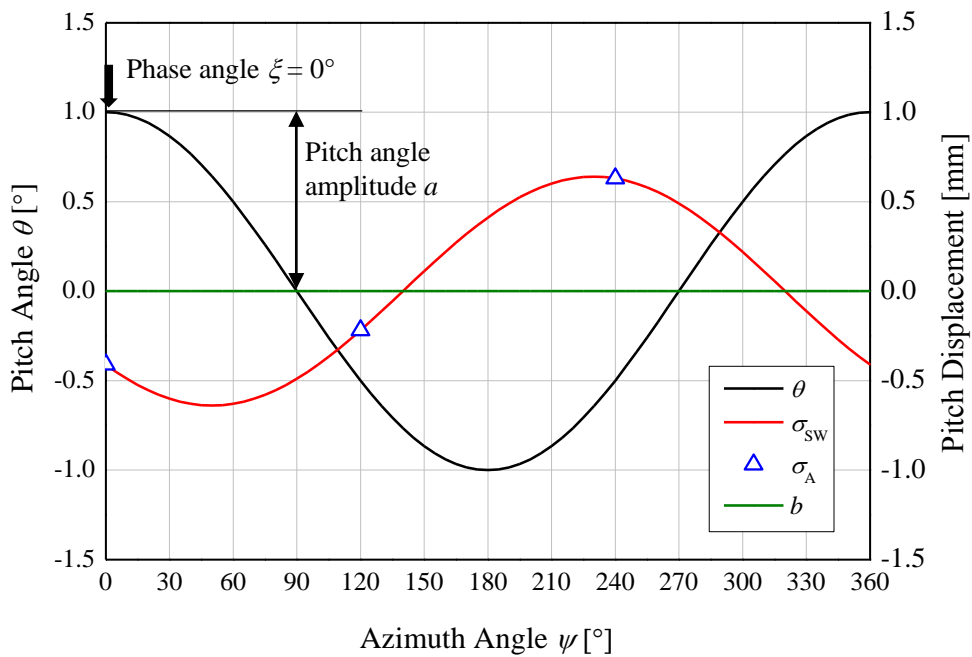


Fig. 6.4 Relationship between swash plate displacement amount and pitch angle change (Case of averaged pitch angle $b = 0^\circ$)

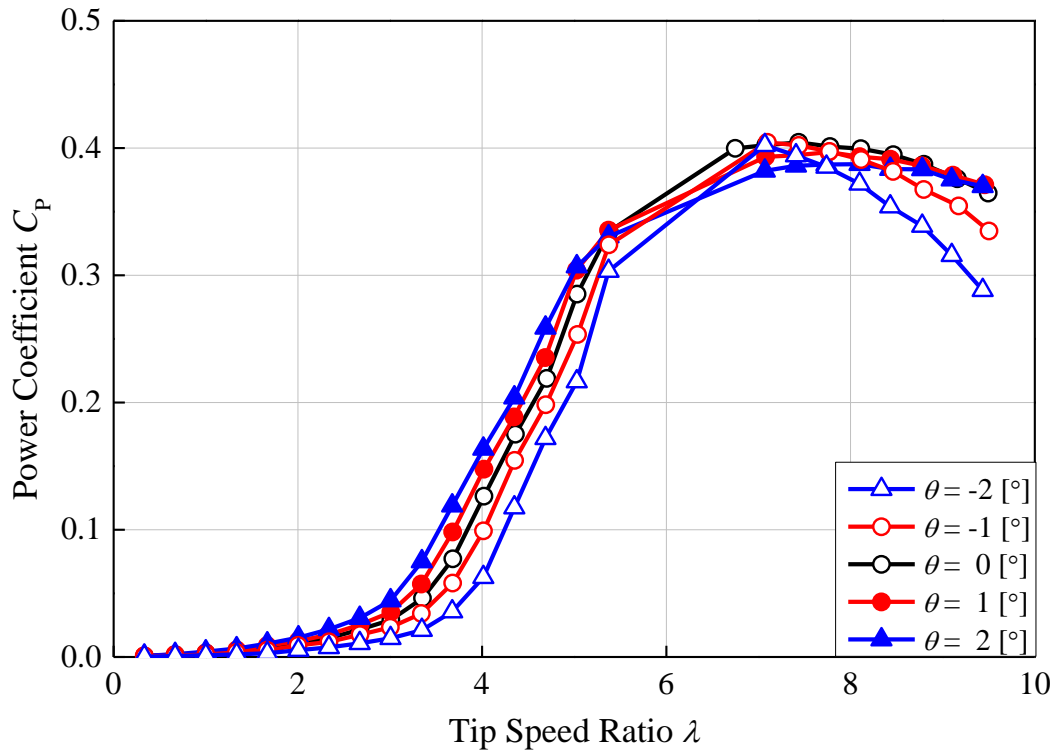
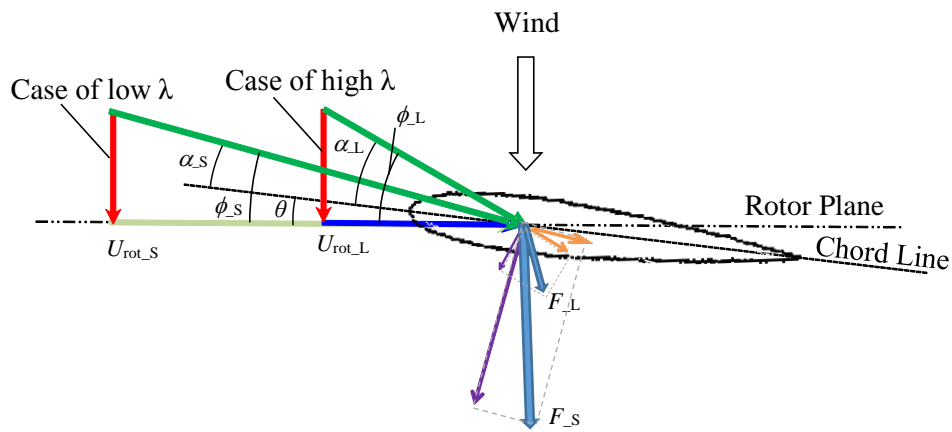
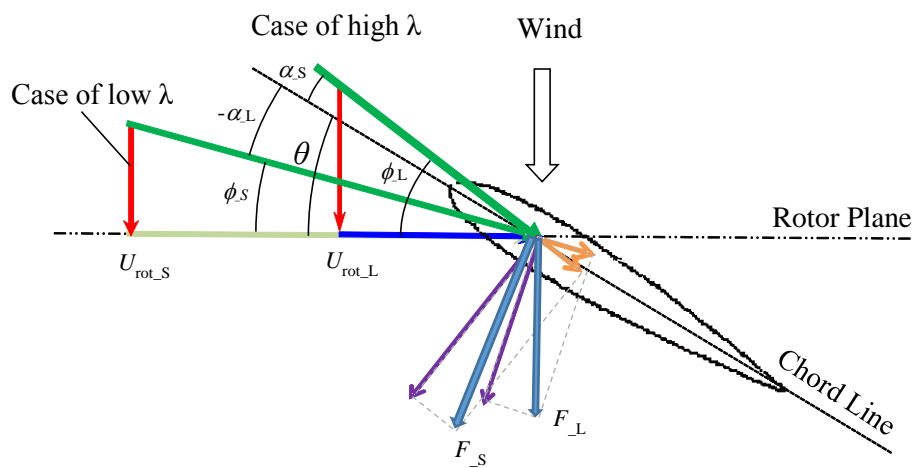


Fig. 6.5 Fluctuation of power coefficient for the pitch angle change



(a) Small pitch angle



(b) Large pitch angle

Fig. 6.6 Fluid force acting on blade element depending on the pitch angle

- where: U_{rot_S} : Rotor speed at the small tip speed ratio
 U_{rot_L} : Rotor speed at the large tip speed ratio
 α_S : Angle of attack at the small tip speed ratio
 α_L : Angle of attack at the large tip speed ratio
 θ : Pitch angle
 ϕ_S : Geometrical inflow angle at the small tip speed ratio
 ϕ_L : Geometrical inflow angle at the large tip speed ratio
 F_S : Aerodynamic force at the small tip speed ratio
 F_L : Aerodynamic force at the large tip speed ratio

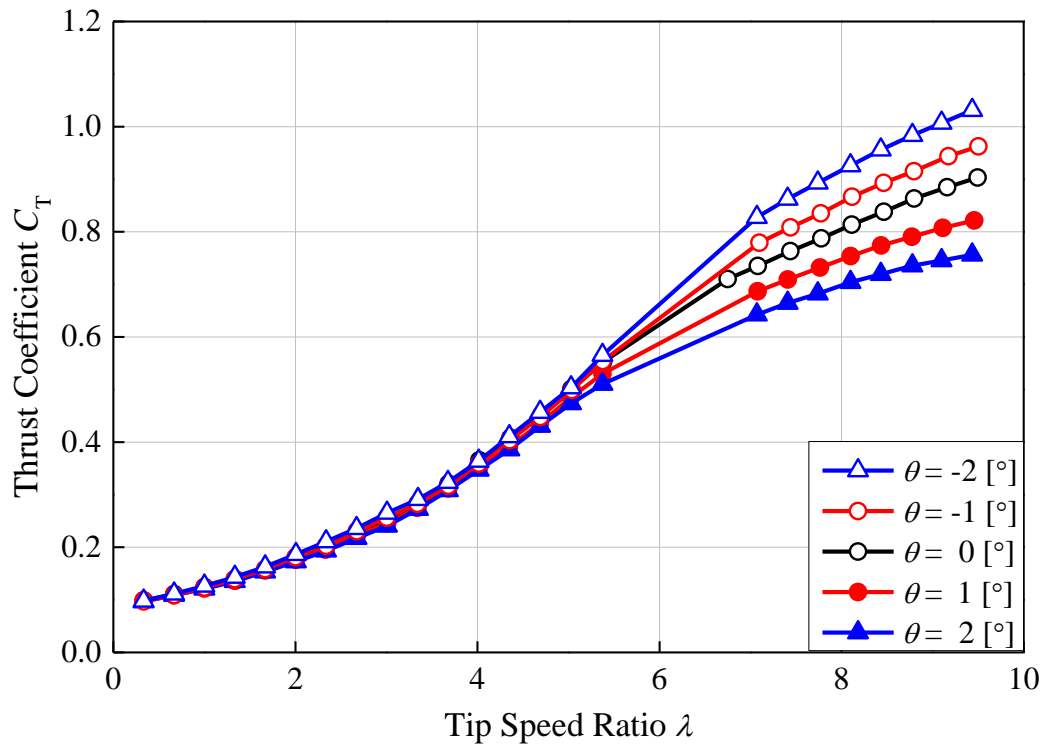


Fig. 6.7 Fluctuation of thrust coefficient for the pitch angle change

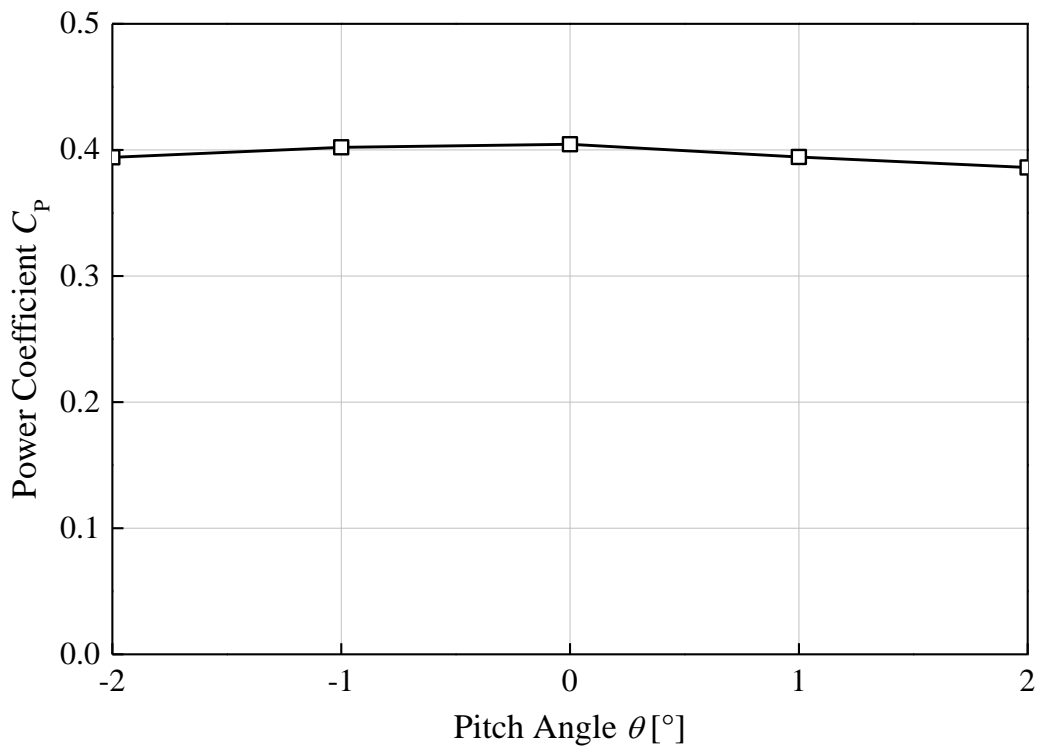


Fig. 6.8 Fluctuation of power coefficient at steady pitch control under optimal operation

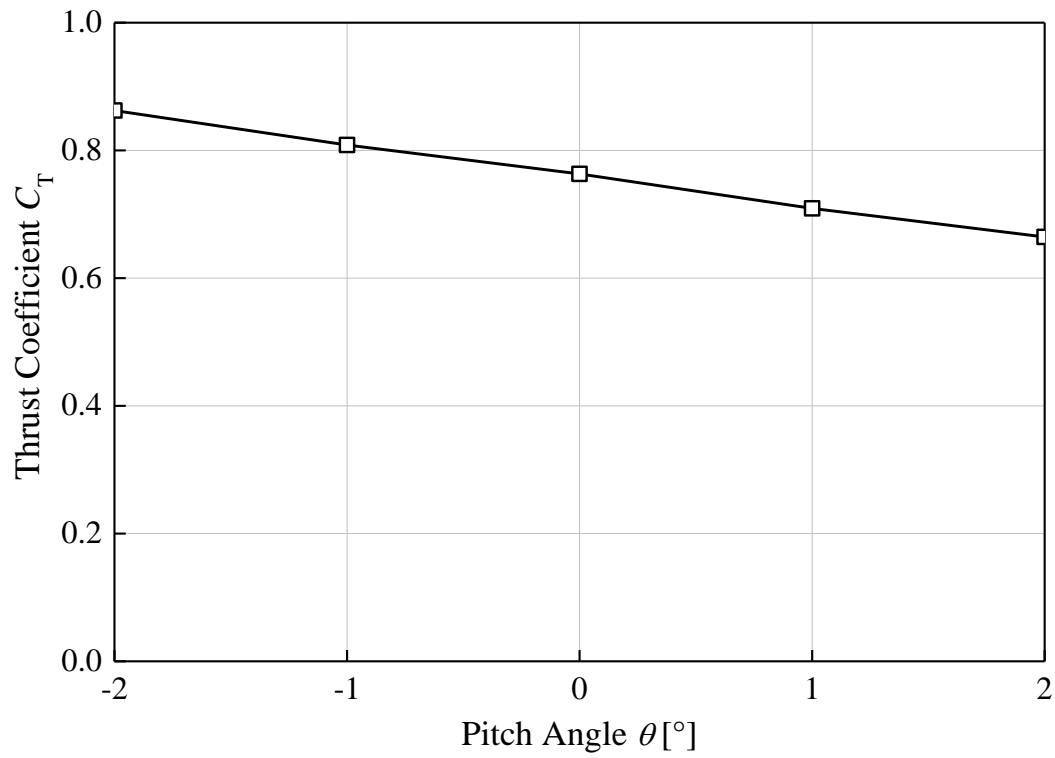


Fig. 6.9 Fluctuation of thrust coefficient at steady pitch control under optimal operation

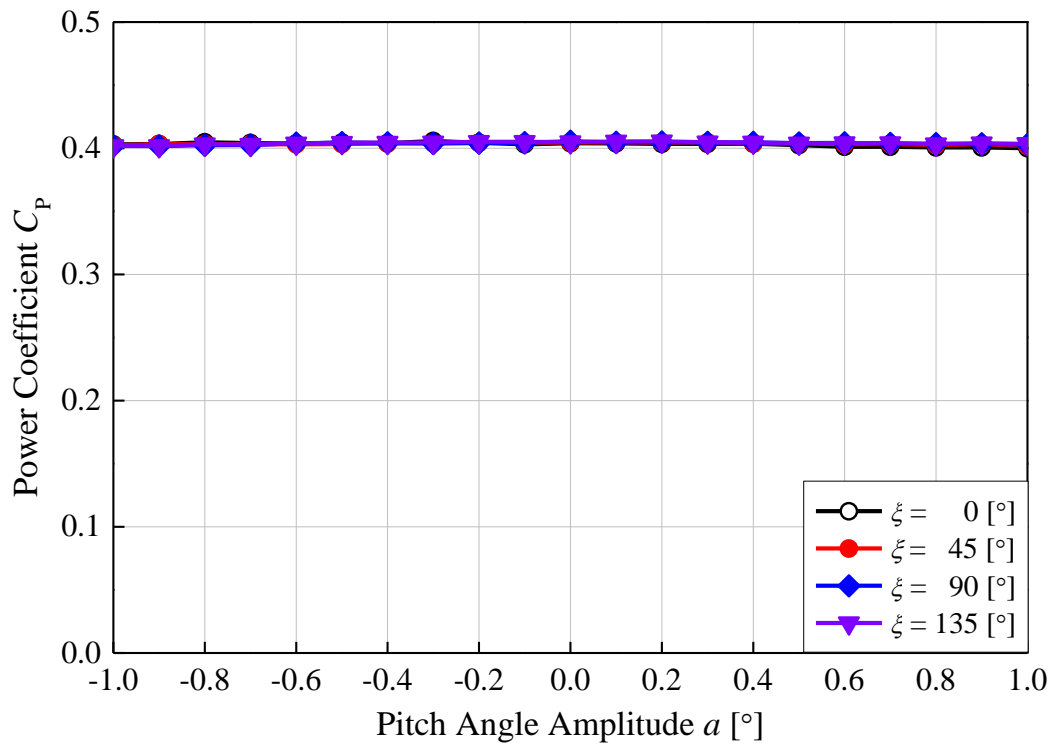


Fig. 6.10 Power coefficient for cyclic pitch control ($\xi = 0^\circ, 45^\circ, 90^\circ$ and 135°)

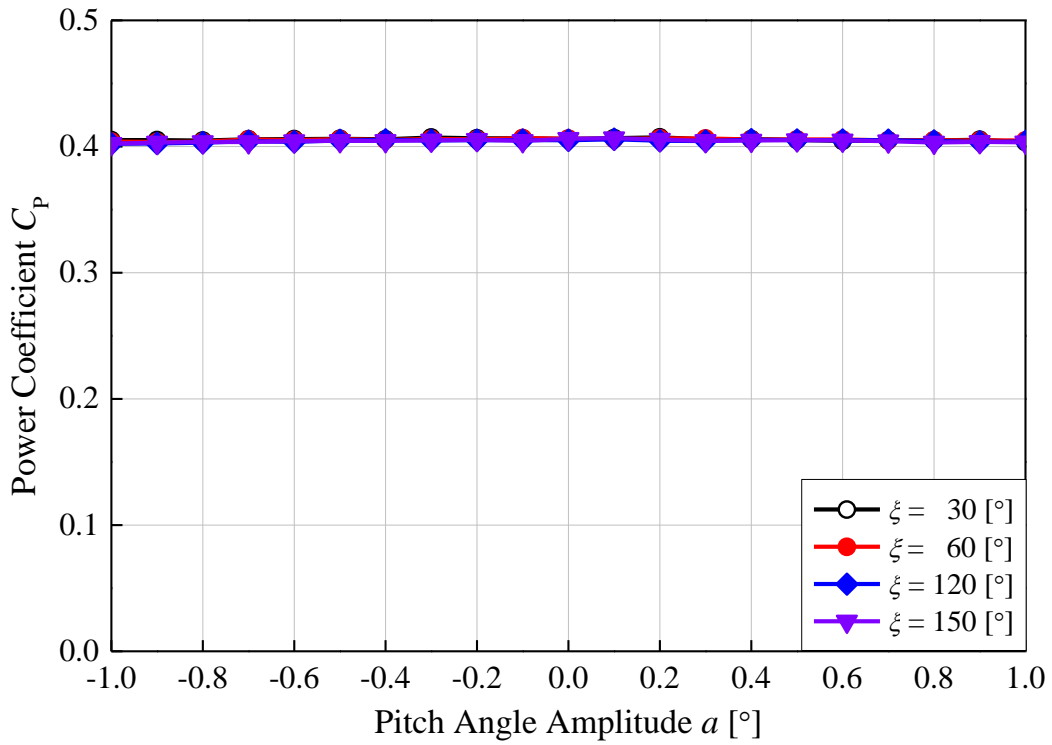


Fig. 6.11 Power coefficient for cyclic pitch control ($\xi = 30^\circ, 60^\circ, 120^\circ$ and 150°)

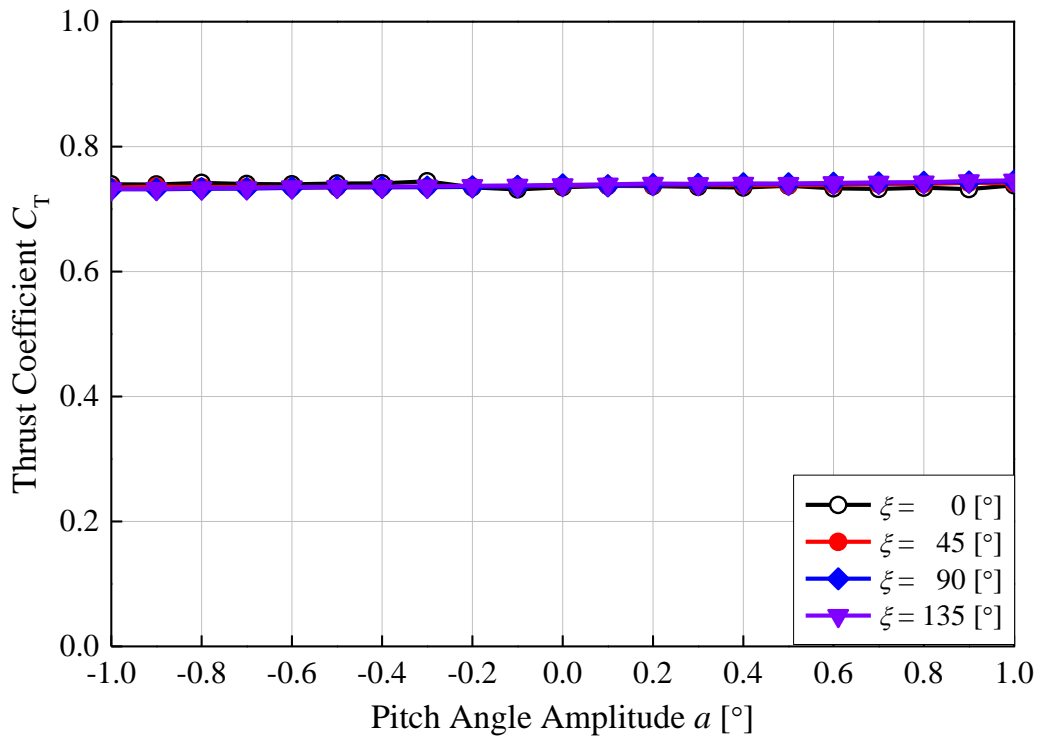


Fig. 6.12 Thrust coefficient for cyclic pitch control ($\xi = 0^\circ, 45^\circ, 90^\circ$ and 135°)

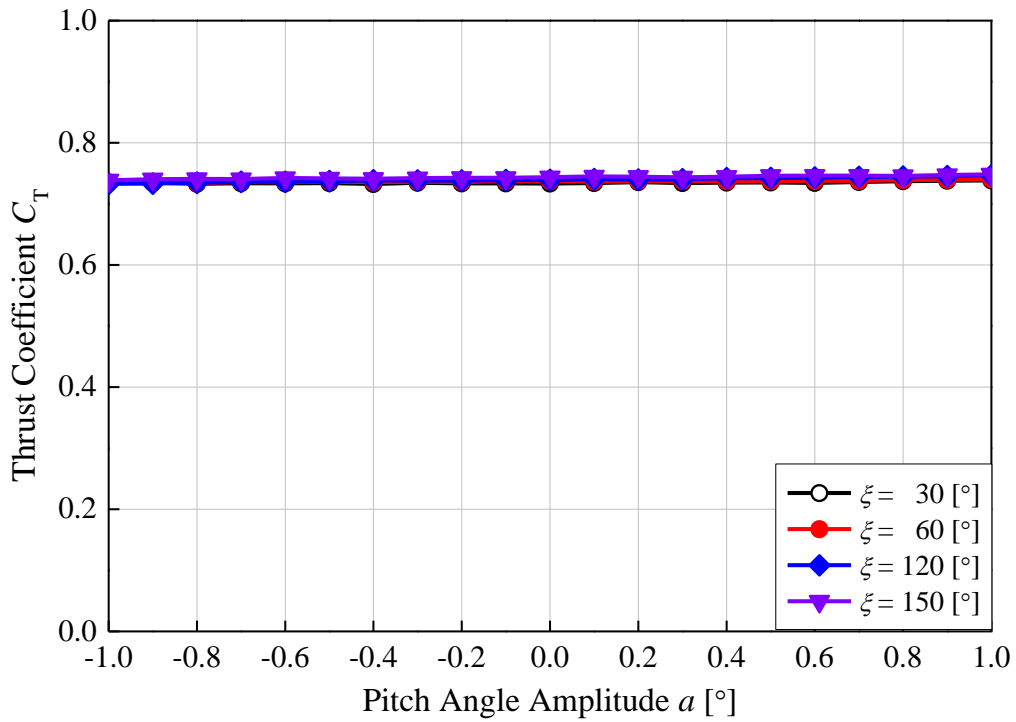


Fig. 6.13 Thrust coefficient for cyclic pitch control ($\xi = 30^\circ, 60^\circ, 120^\circ$ and 150°)

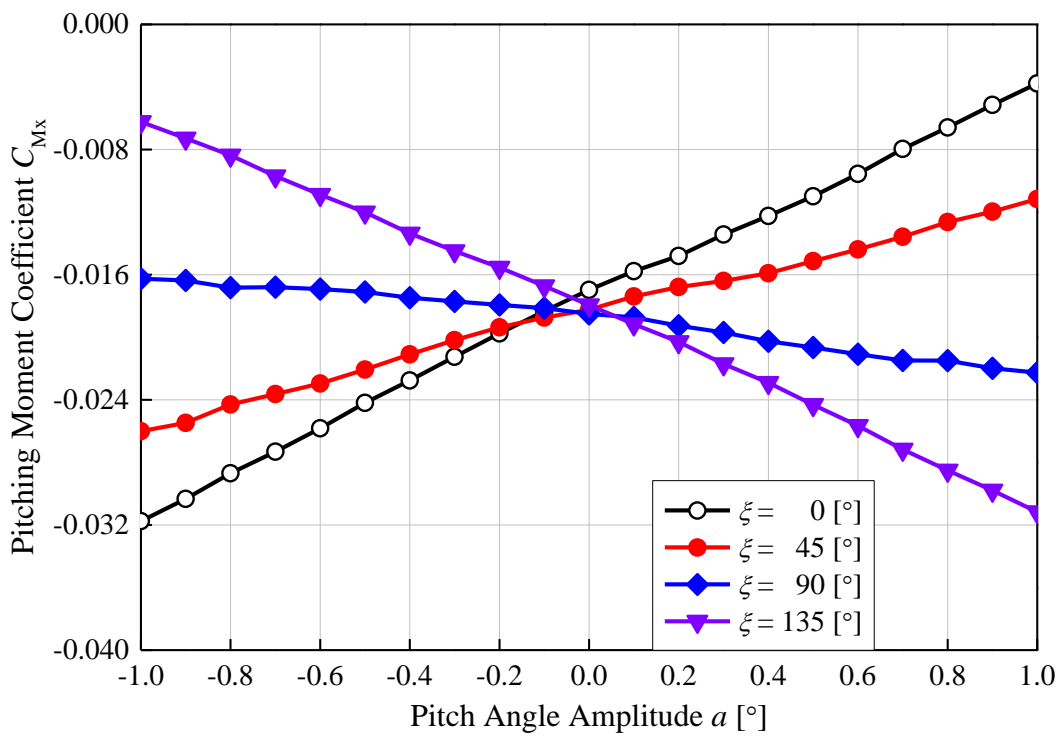


Fig. 6.14 Pitching moment coefficient for cyclic pitch control ($\xi = 0^\circ, 45^\circ, 90^\circ$ and 135°)

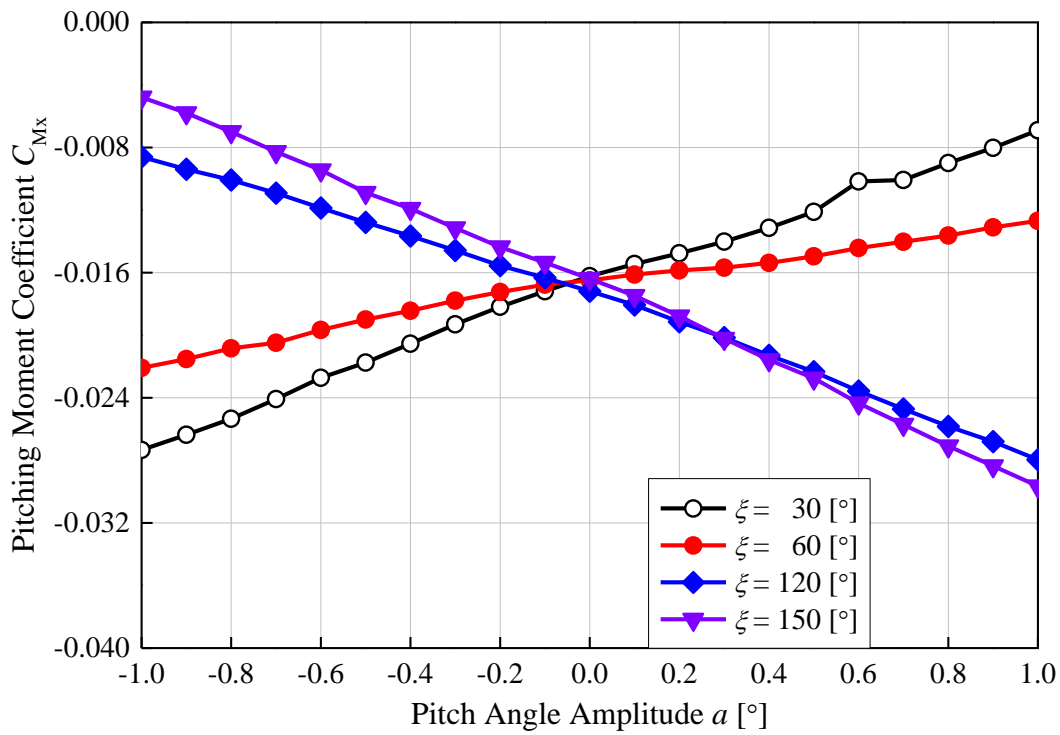


Fig. 6.15 Pitching moment coefficient for cyclic pitch control ($\xi = 30^\circ, 60^\circ, 120^\circ$ and 150°)

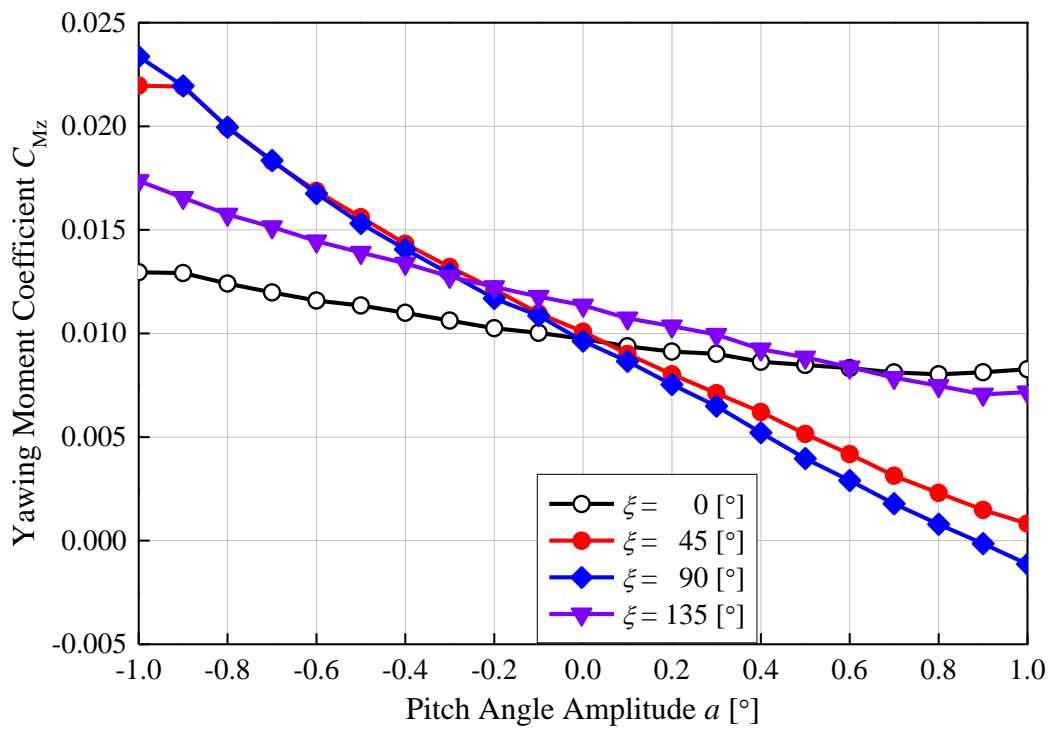


Fig. 6.16 Yawing moment coefficient for cyclic pitch control ($\xi = 0^\circ, 45^\circ, 90^\circ$ and 135°)

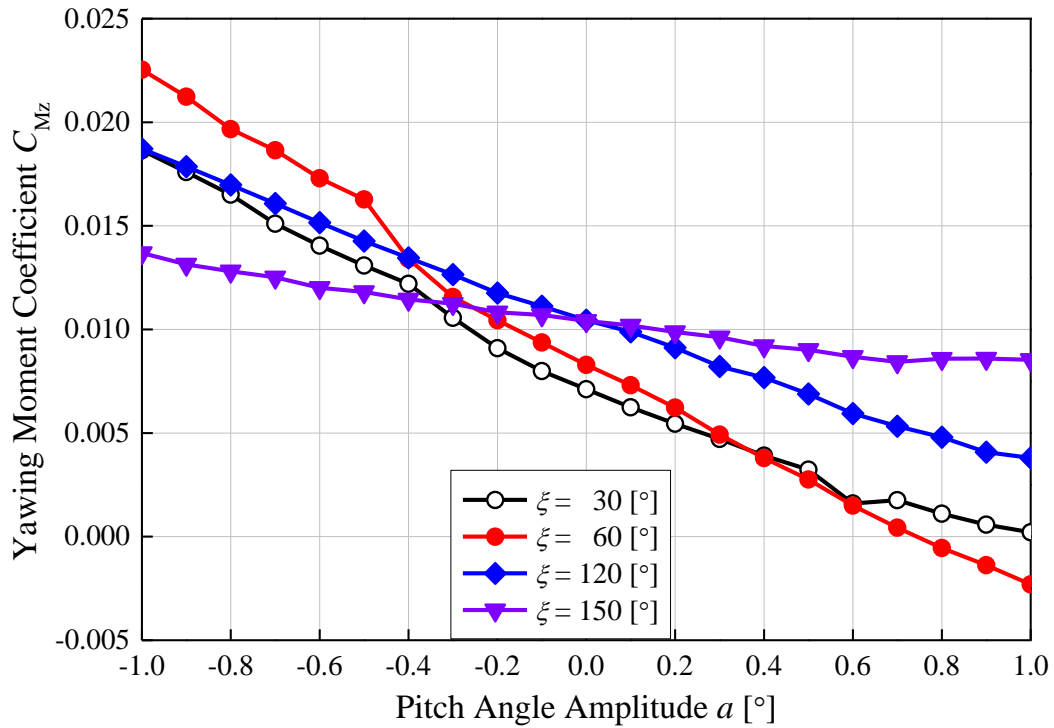


Fig. 6.17 Yawing moment coefficient for cyclic pitch control ($\xi = 30^\circ, 60^\circ, 120^\circ$ and 150°)

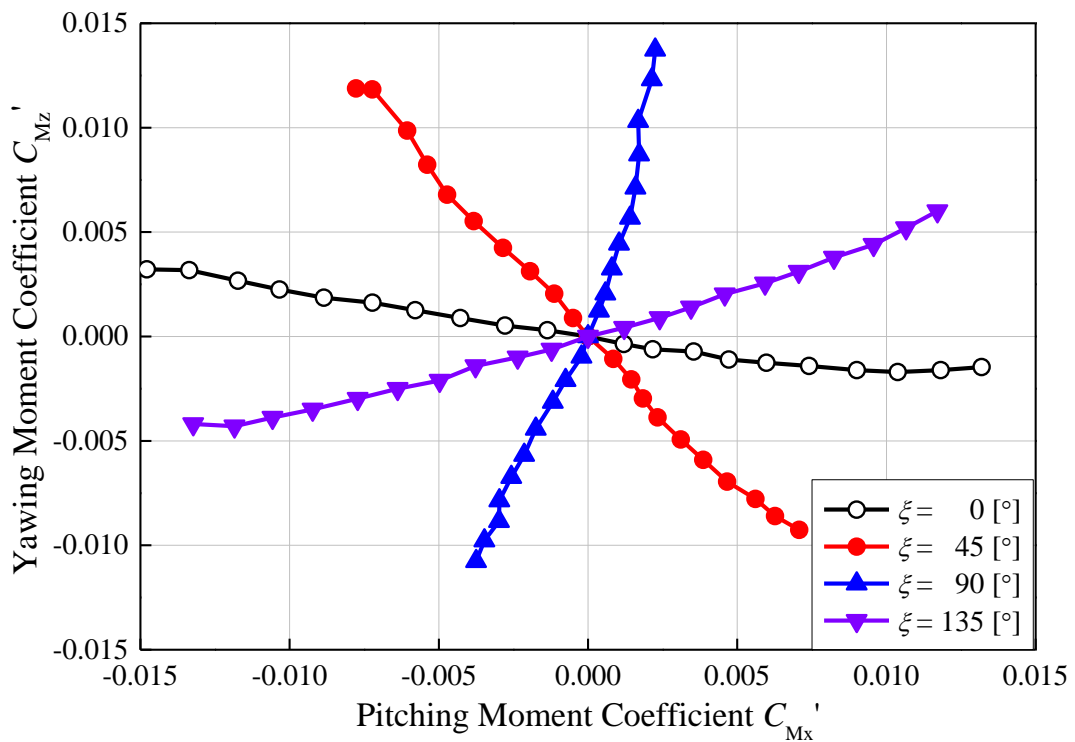


Fig. 6.18 Moment coefficient for cyclic pitch control ($\xi = 0^\circ, 45^\circ, 90^\circ$ and 135°)

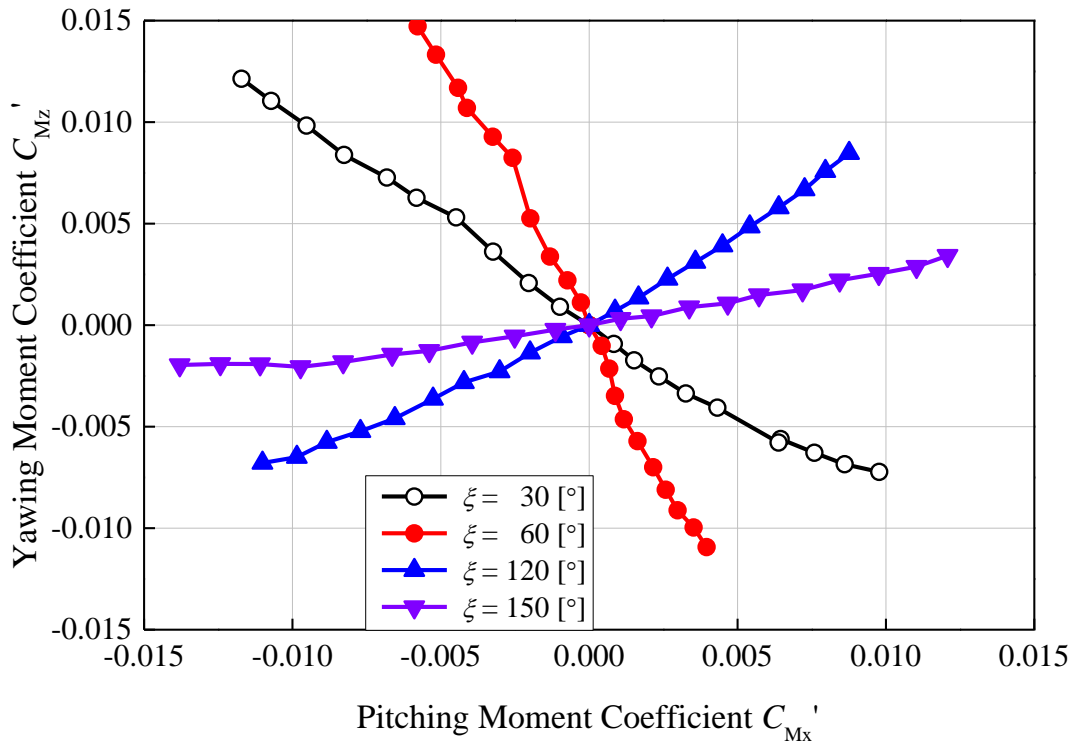


Fig. 6.19 Moment coefficient for cyclic pitch control ($\xi = 30^\circ, 60^\circ, 120^\circ$ and 150°)

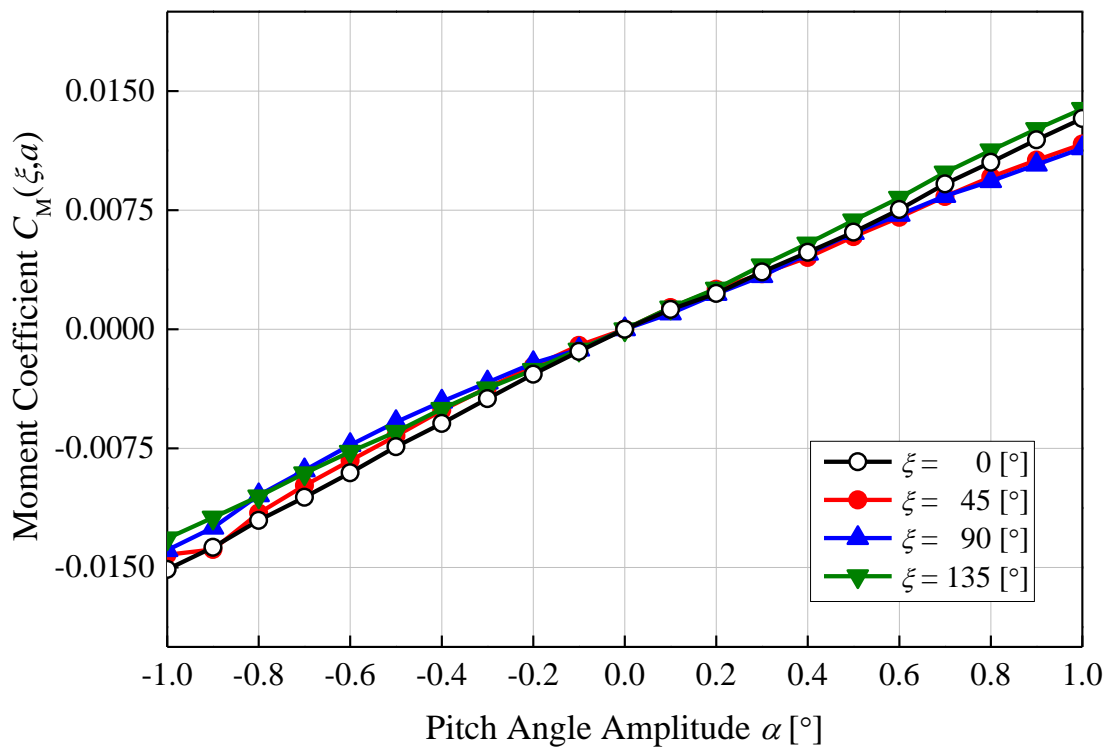


Fig. 6.20 Moment coefficient for cyclic pitch control ($\xi = 0^\circ, 45^\circ, 90^\circ$ and 135°)

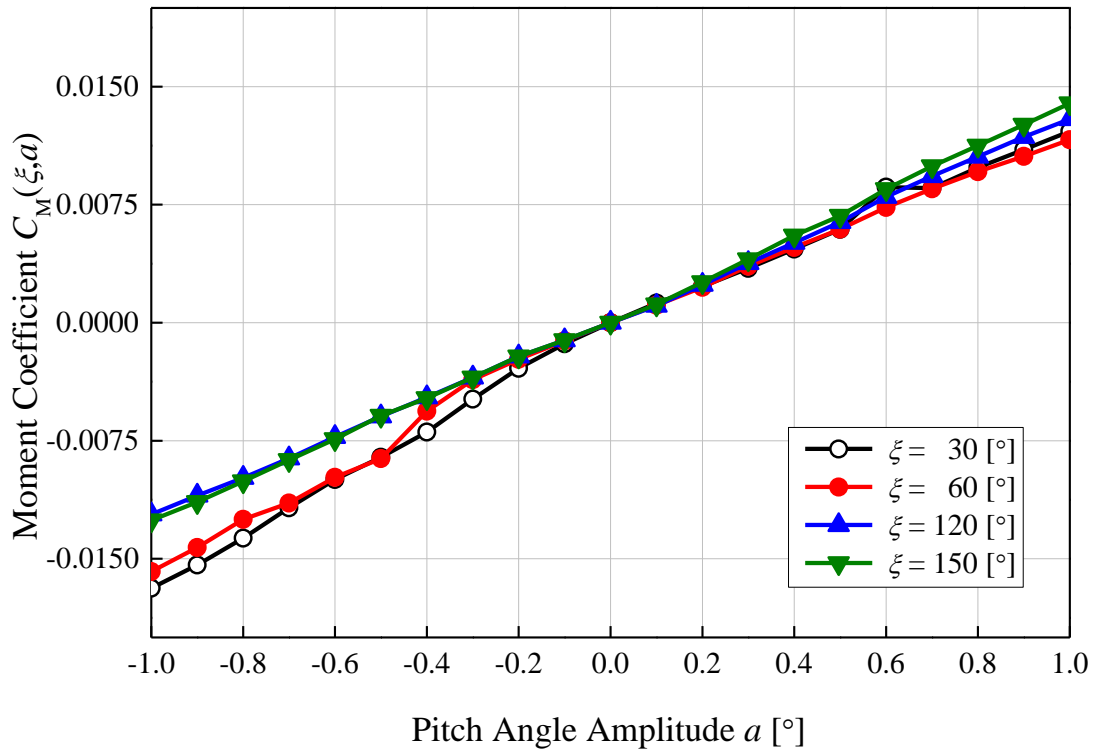


Fig. 6.21 Moment coefficient for cyclic pitch control ($\xi = 30^\circ, 60^\circ, 120^\circ$ and 150°)

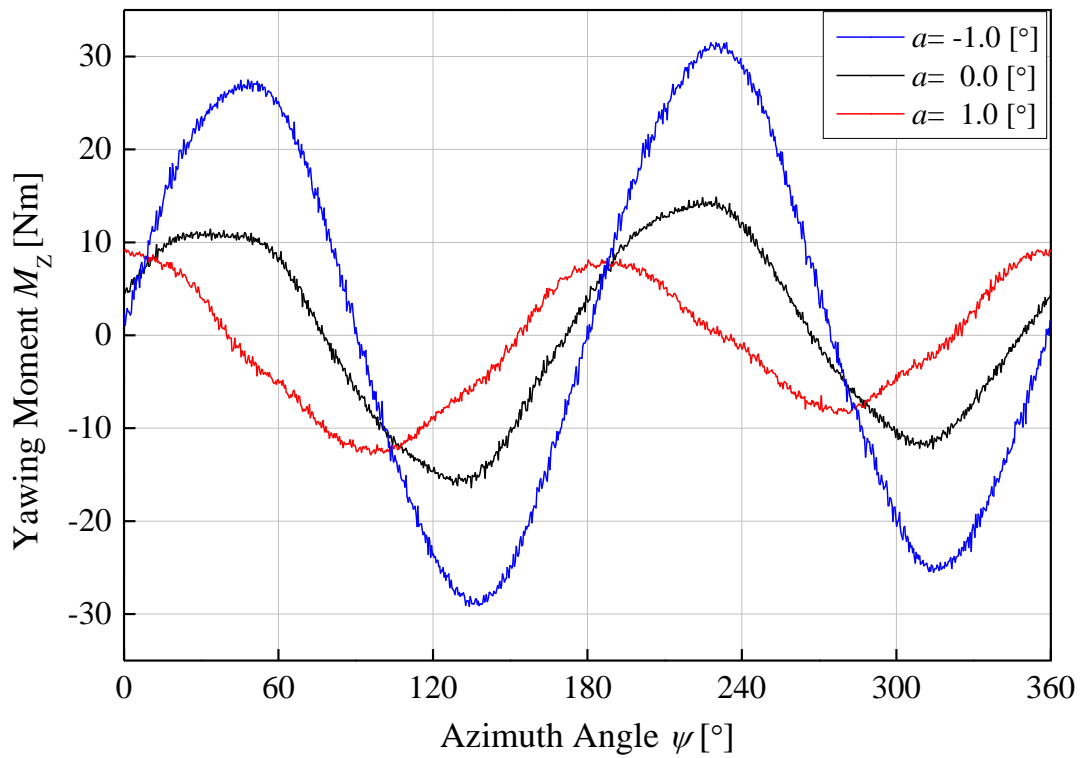


Fig. 6.22 Variation of yawing moment with respect to cyclic pitch control

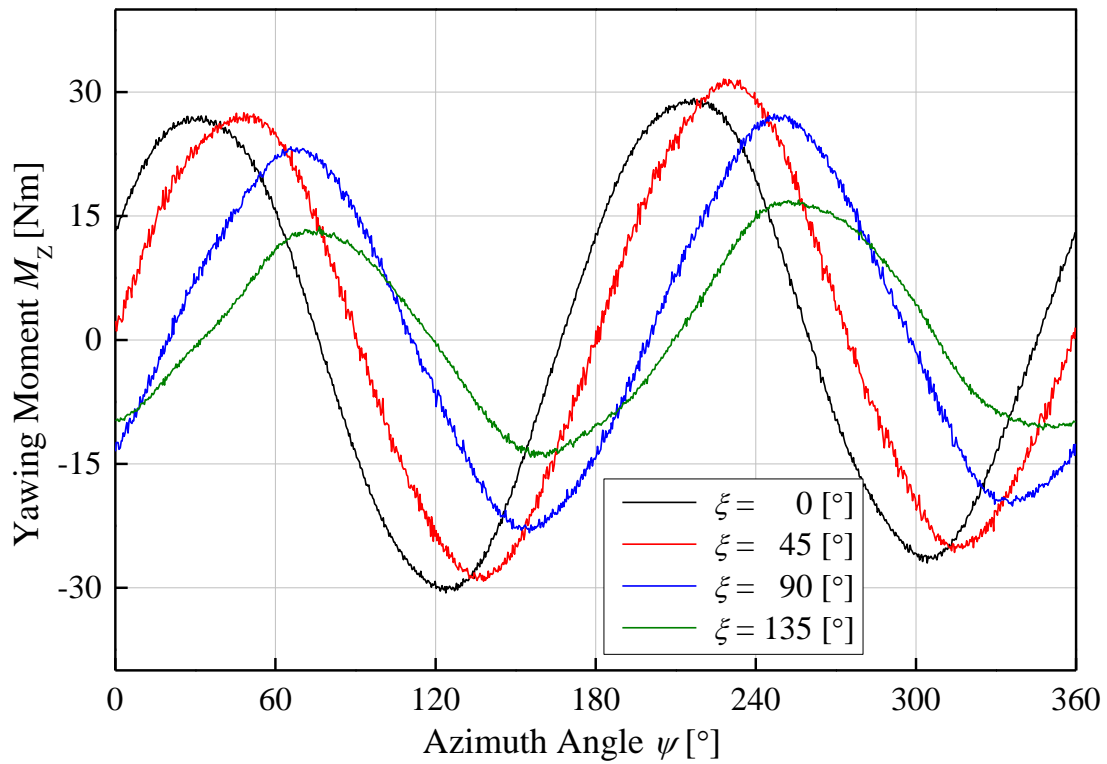


Fig. 6.23 Variation of yawing moment for phase angle change ($a = -1$)

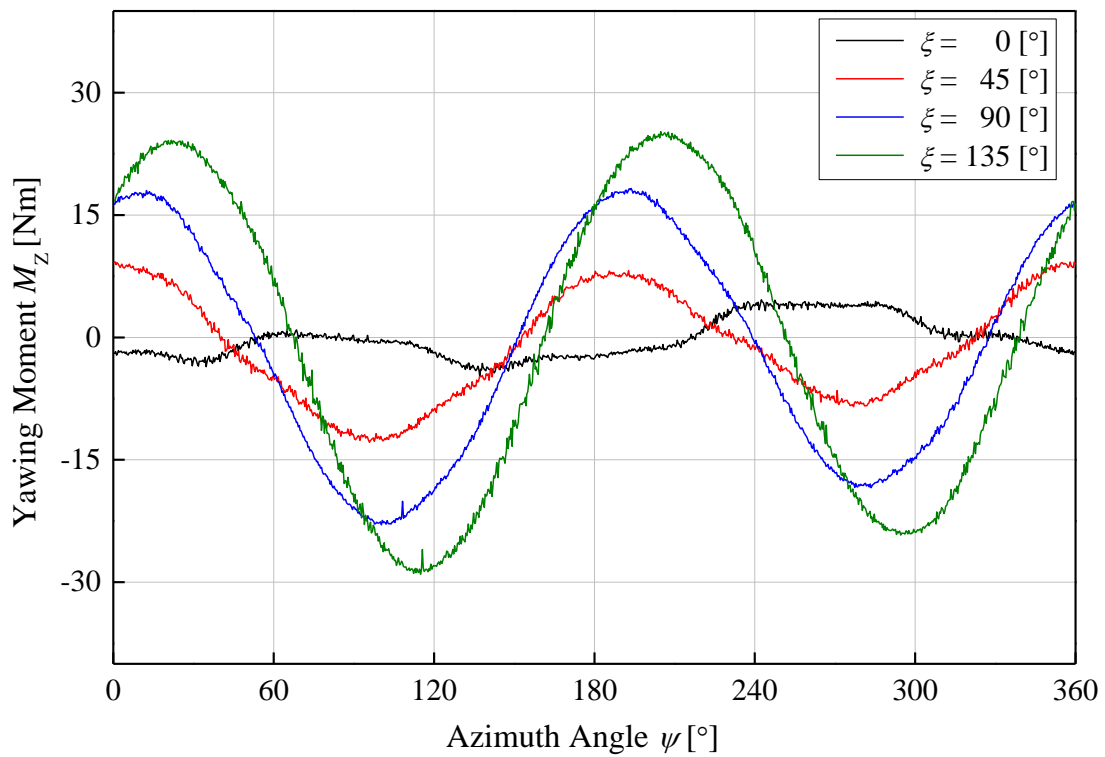


Fig. 6.24 Variation of yawing moment for phase angle change ($a = +1$)

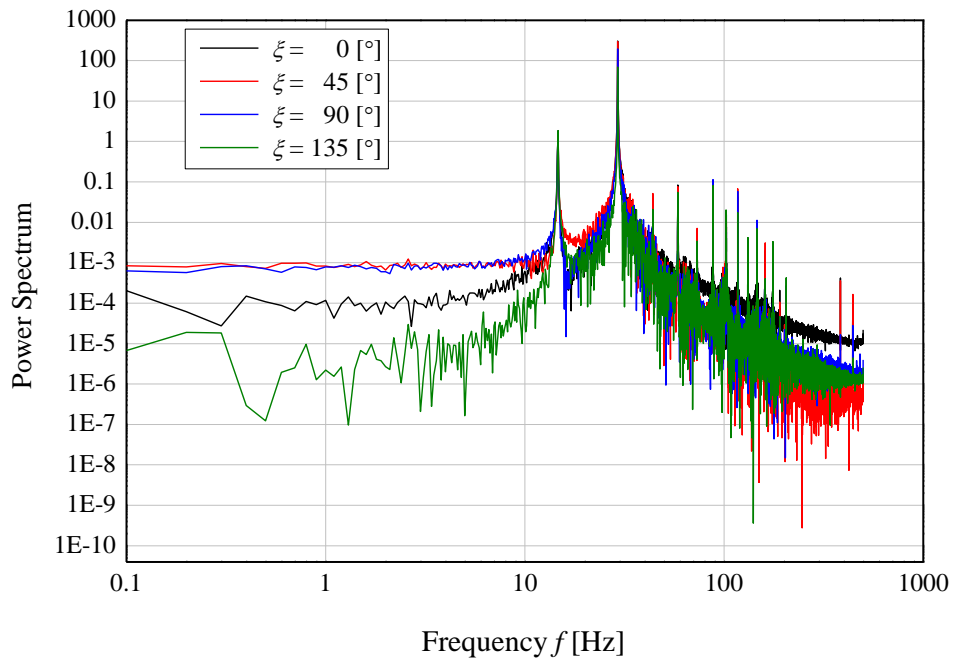


Fig. 6.25 Variations of spectra of the phase angles at the pitch angle amplitude $a = -1$

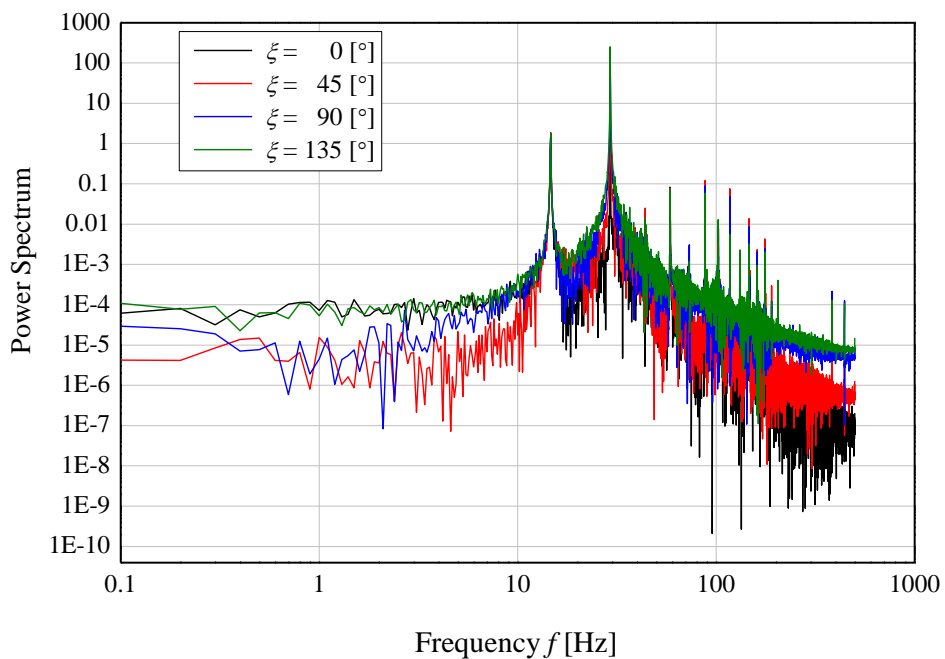


Fig. 6.26 Variations of spectra of the phase angles at the pitch angle amplitude $a = +1$

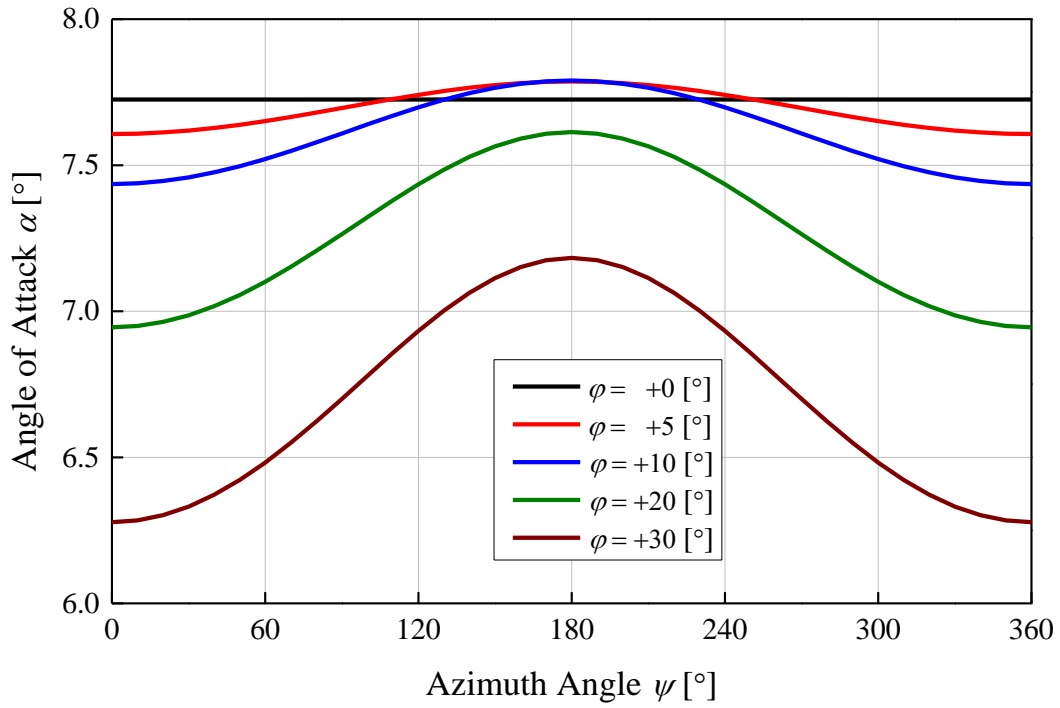


Fig. 6.27 Variation of angle of attack at each yaw angle

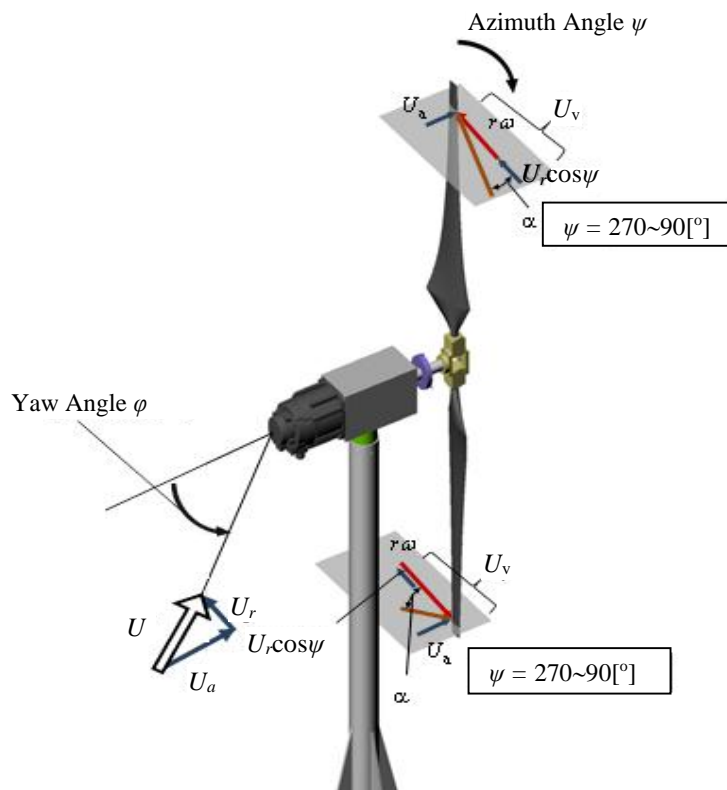


Fig. 6.28 Change angle of attack due to azimuth angle position

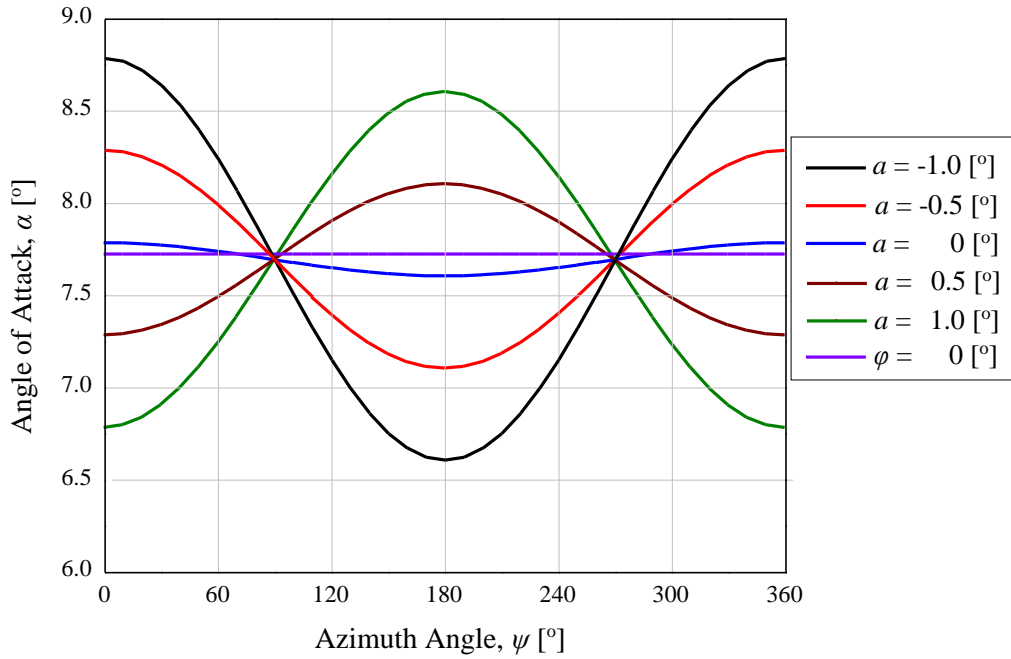
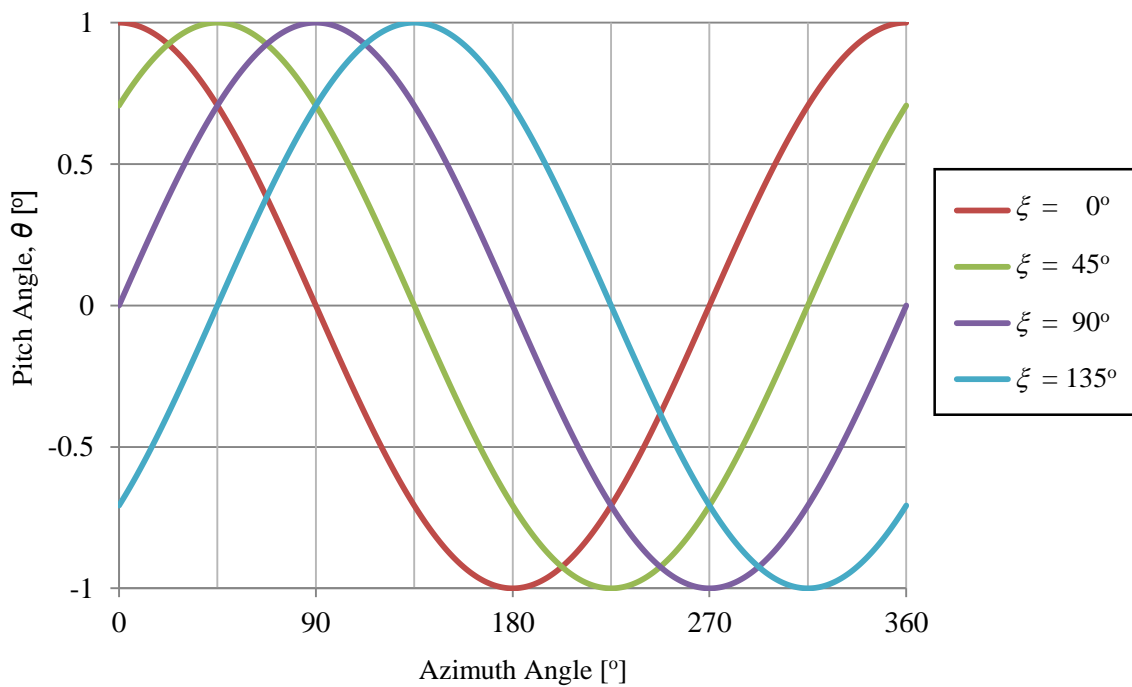
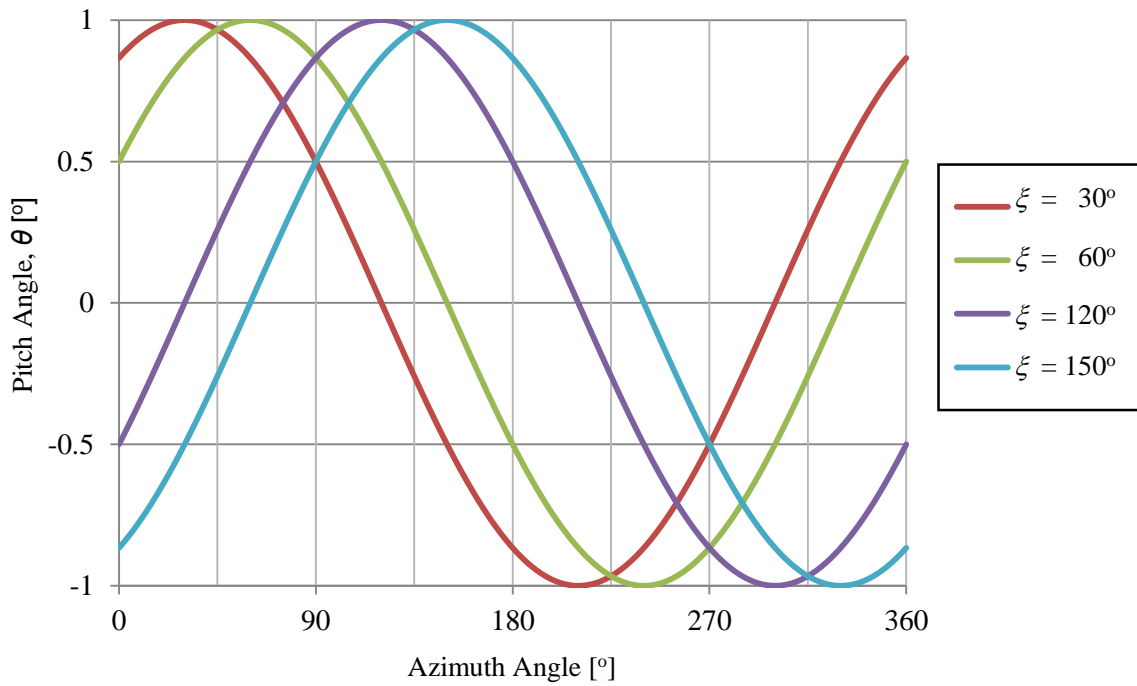


Fig. 6.29 Modification of angle of attack with each pitch angle amplitude at the yaw angle of $\varphi = -5^\circ$ and the pitch angle phase of $\xi = 0^\circ$.



(a) The phase angle of $\xi = 0^\circ, 45^\circ, 90^\circ, 135^\circ$



(b) The phase angle of $\xi = 30^\circ, 60^\circ, 120^\circ, 150^\circ$

Fig. 6.30 Relation between the pitch angle and azimuth angle

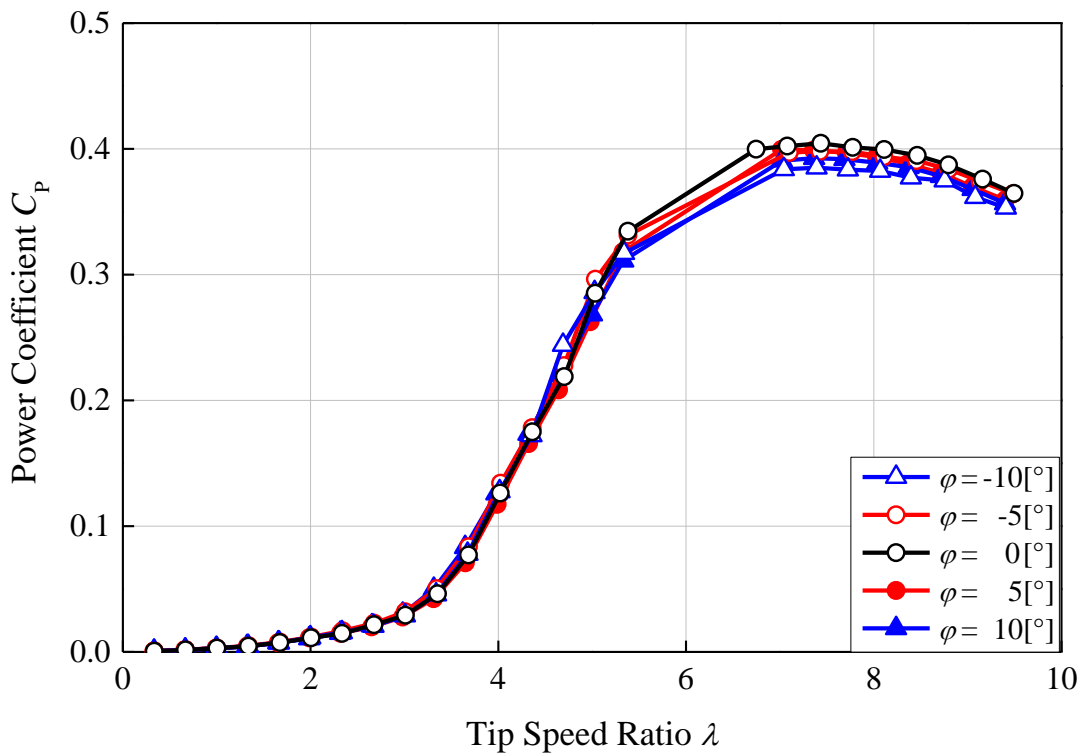


Fig. 6.31 Fluctuation of power coefficient responds to change of yaw angle $\varphi = \pm 10^\circ, \pm 5^\circ$ and 0°

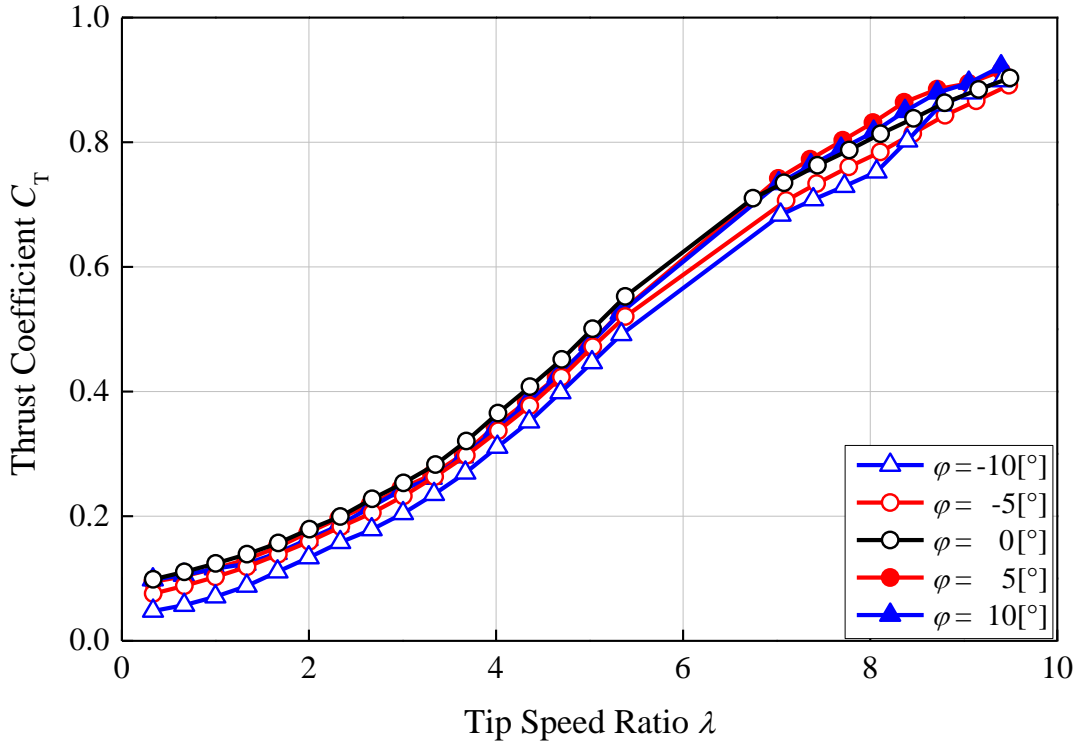


Fig. 6.32 Fluctuation of thrust coefficient responds to change of yaw angle $\varphi = \pm 10^\circ, \pm 5^\circ$ and 0°

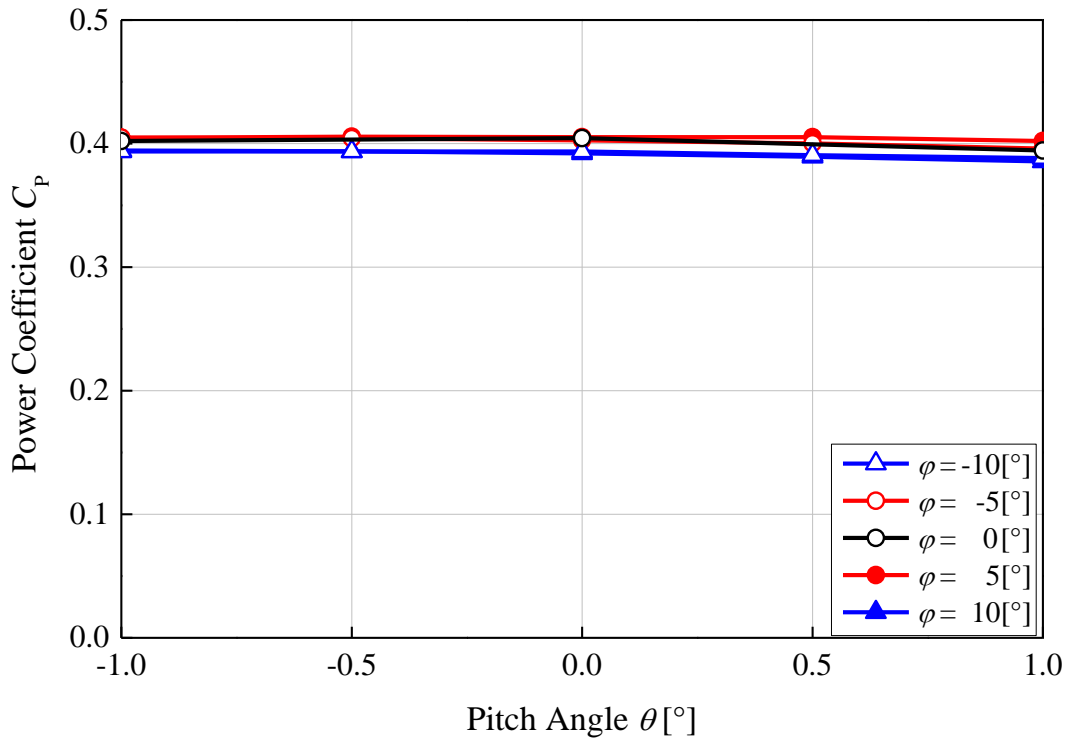


Fig. 6.33 Relationship between power coefficient and the blade pitch angle at the yaw angle $\varphi = \pm 10^\circ, \pm 5^\circ$ and 0°

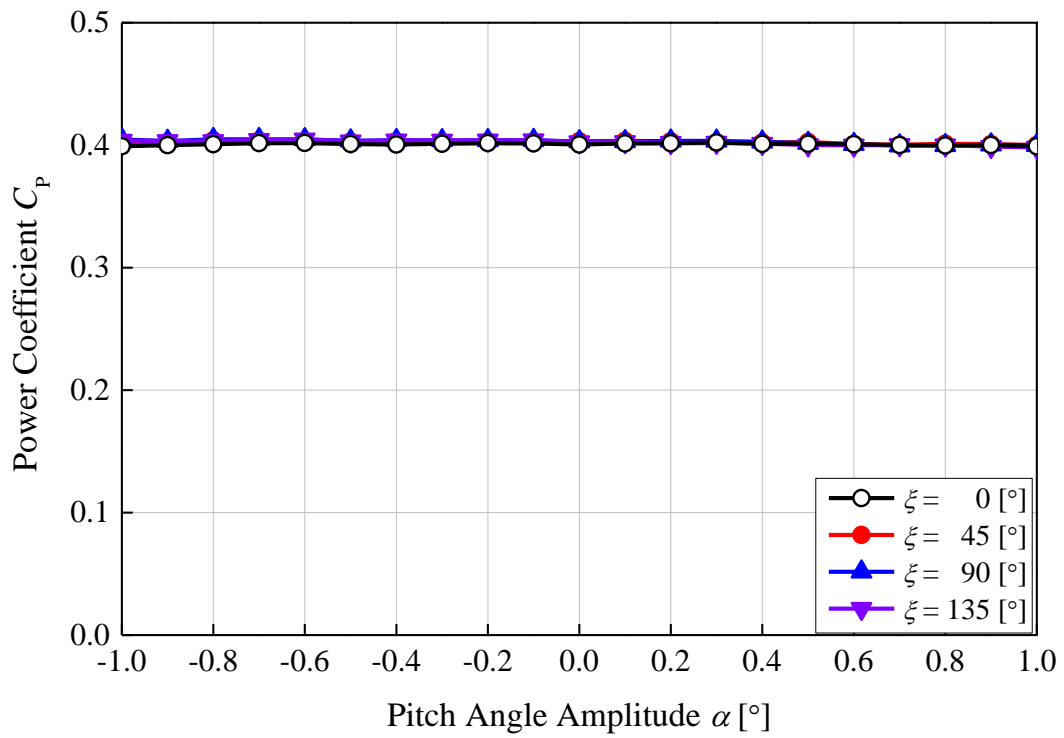


Fig. 6.34 Relationship between the power coefficient and the pitch angle amplitude with the phase $\xi = 0^\circ, 45^\circ, 90^\circ$ and 135°

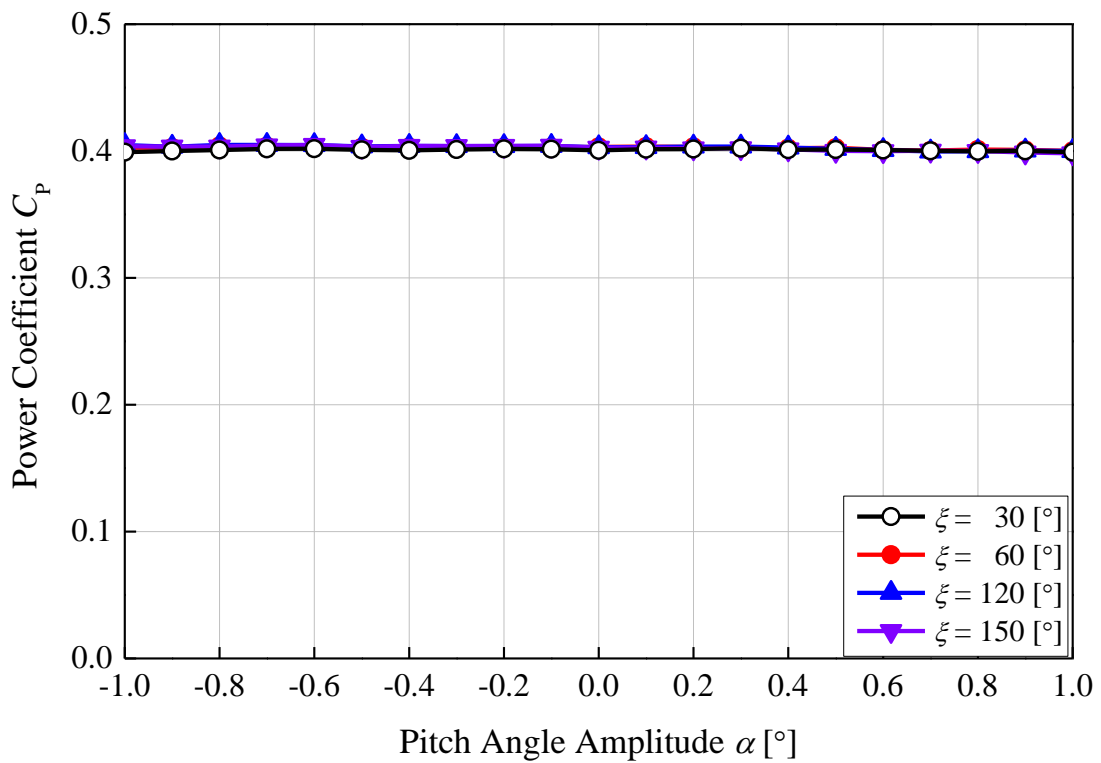


Fig. 6.35 Relationship between the power coefficient and the pitch angle amplitude with the phase $\xi = 30^\circ, 60^\circ, 120^\circ$ and 150°

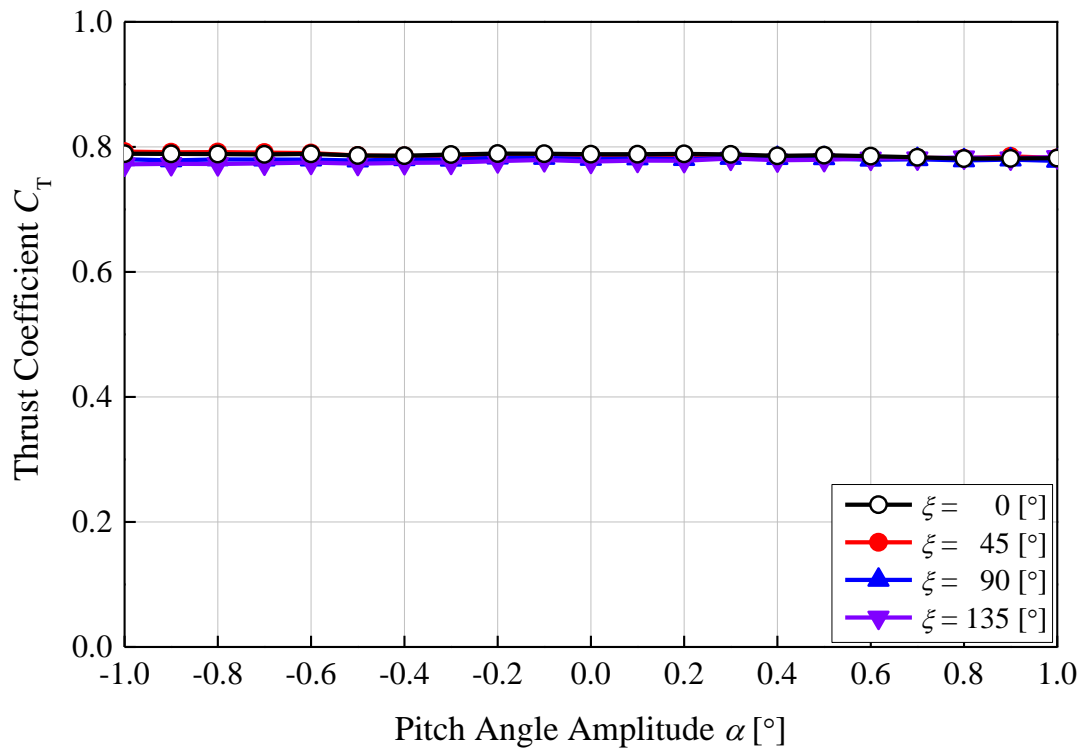


Fig. 6.36 Relationship between the thrust coefficient and the pitch angle amplitude with the phase $\xi = 0^\circ, 45^\circ, 90^\circ$ and 135°

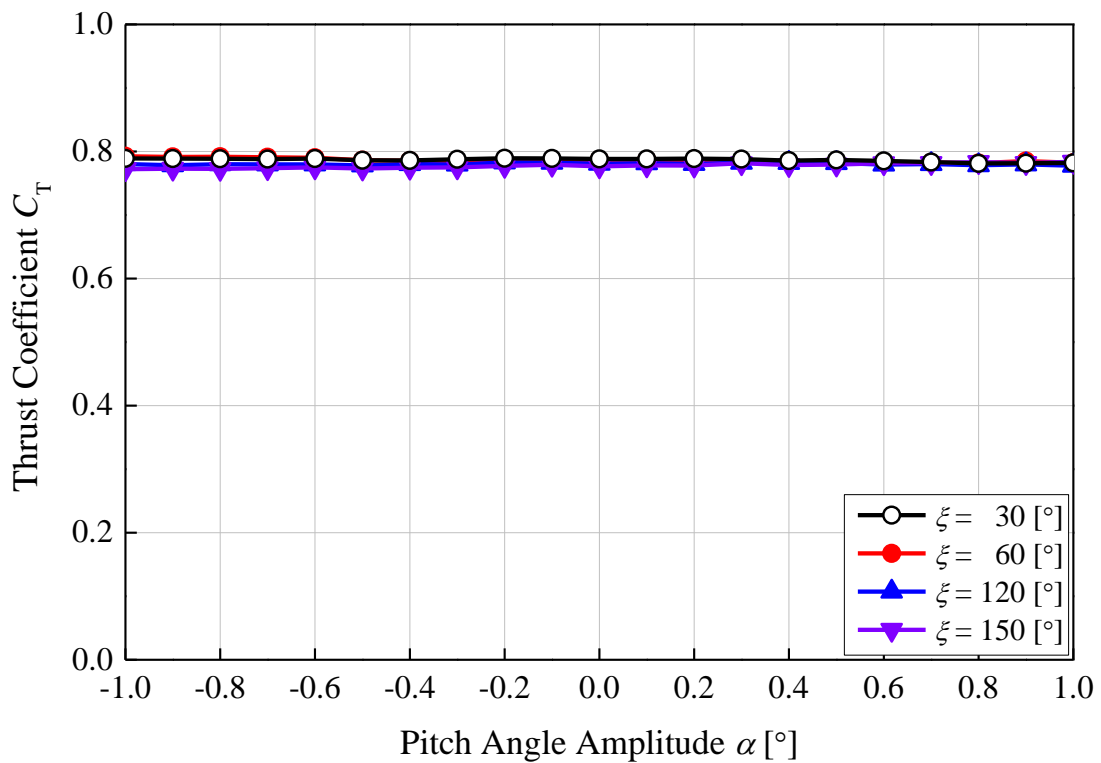


Fig. 6.37 Relationship between the thrust coefficient and the pitch angle amplitude with the phase $\xi = 30^\circ, 60^\circ, 120^\circ$ and 150°

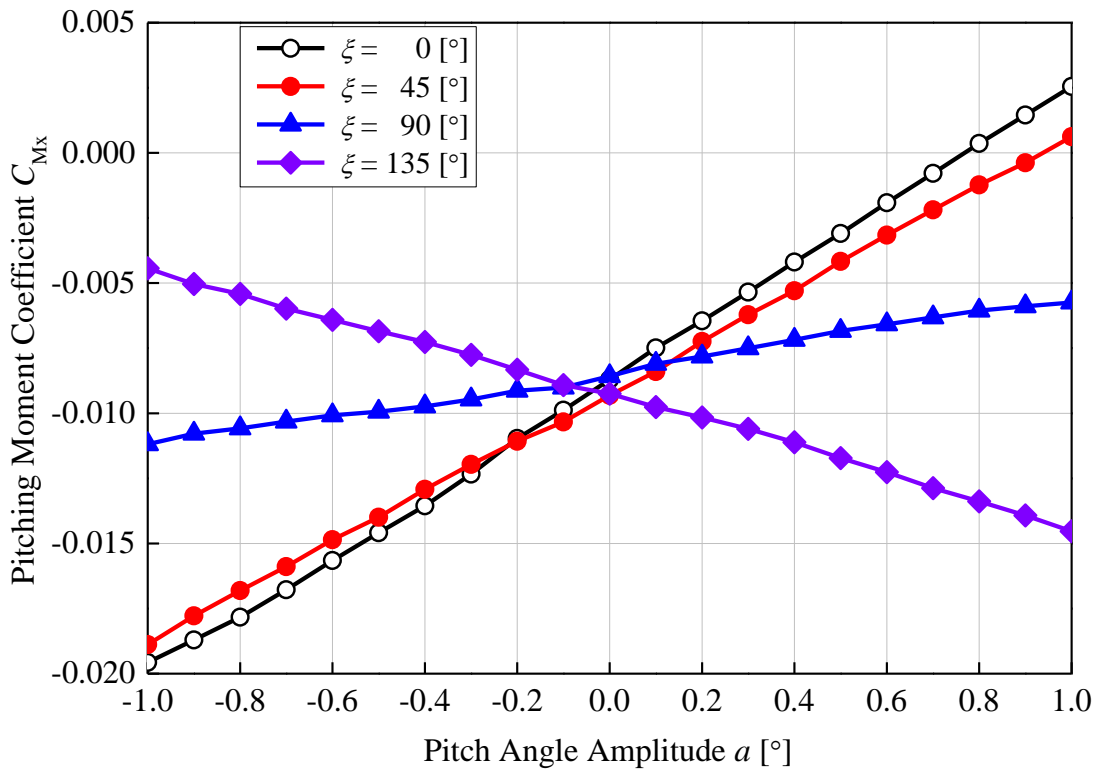


Fig. 6.38 Fluctuation of pitching moment coefficient and the pitch angle amplitude change in the cyclic pitch control with the pitch angle phases of $\xi = 0^\circ, 45^\circ, 90^\circ$ and 135° .

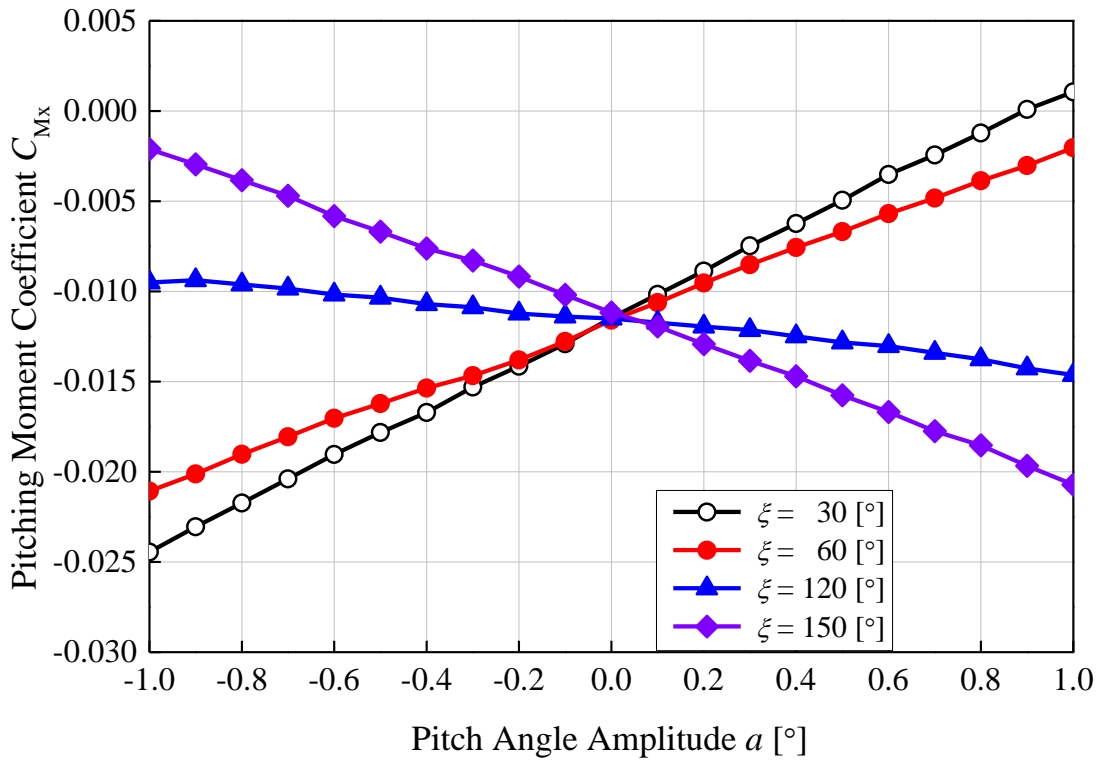


Fig. 6.39 Fluctuation of pitching moment coefficient and the pitch angle amplitude change in the cyclic pitch control with the pitch angle phases of $\xi = 30^\circ, 60^\circ, 120^\circ$ and 150° .

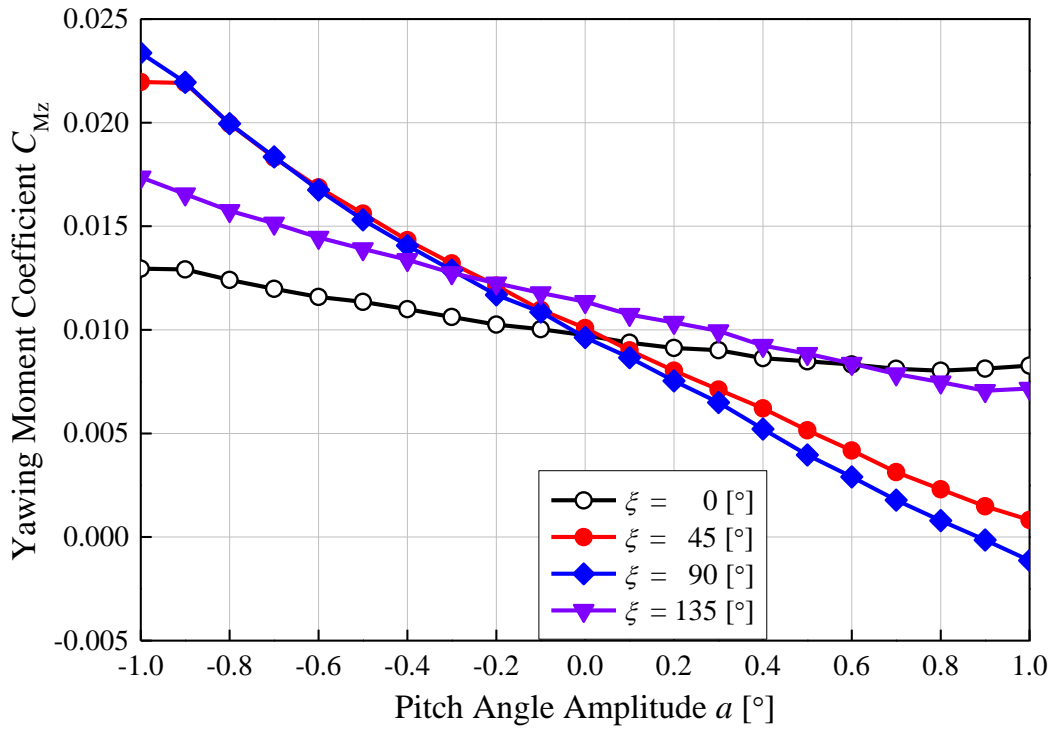


Fig. 6.40 Fluctuation of yawing moment coefficient and the pitch angle amplitude change in the cyclic pitch control with the pitch angle phases of $\xi = 0^\circ, 45^\circ, 90^\circ$ and 135° .

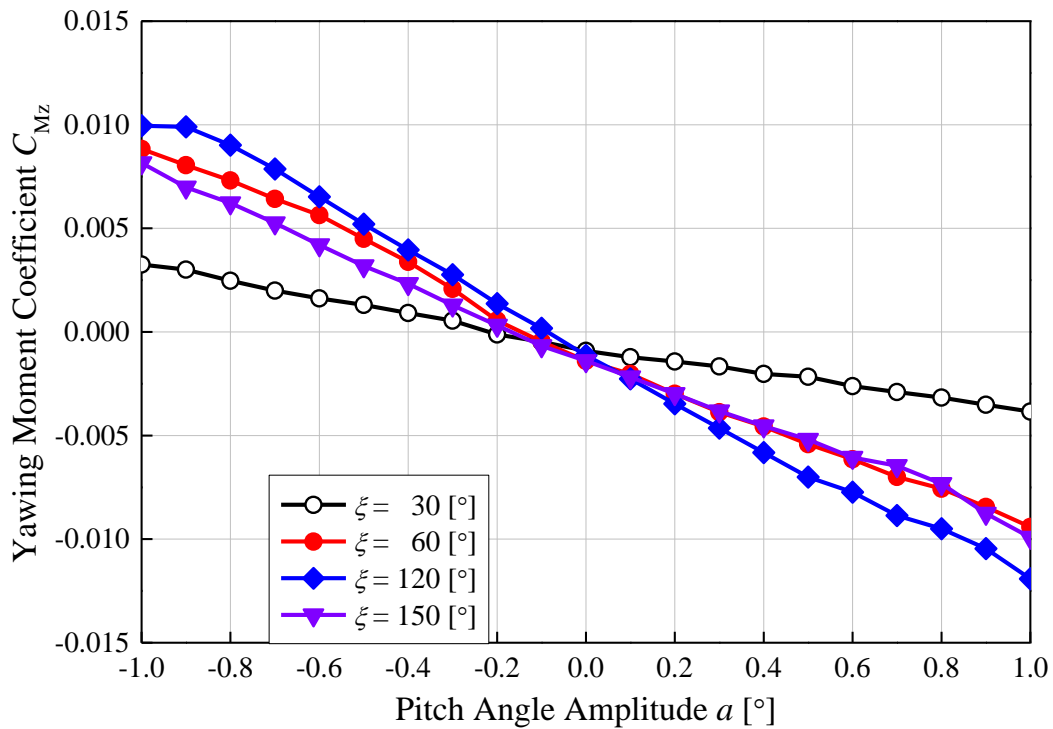


Fig. 6.41 Fluctuation of yawing moment coefficient and the pitch angle amplitude change in the cyclic pitch control with the pitch angle phases of $\xi = 30^\circ, 60^\circ, 120^\circ$ and 150° .

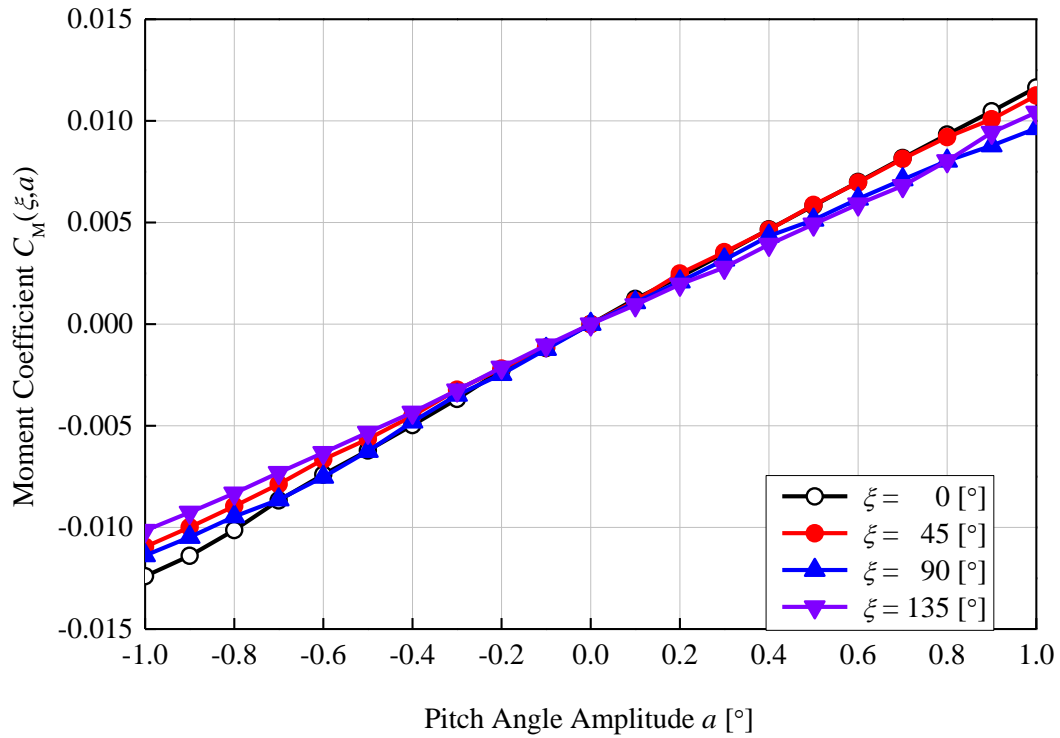


Fig. 6.42 Moment coefficient for cyclic pitch control of $\xi = 0^\circ, 45^\circ, 90^\circ$ and 135° .

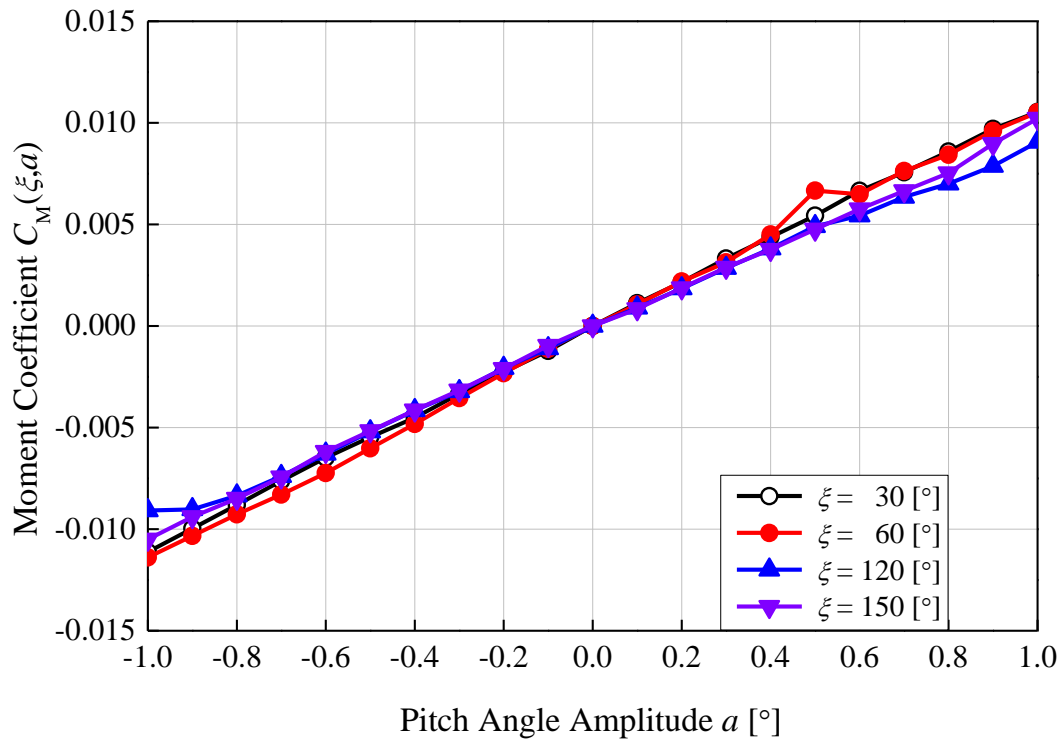


Fig. 6.43 Moment coefficient for cyclic pitch control of $\xi = 30^\circ, 60^\circ, 120^\circ$ and 150° .

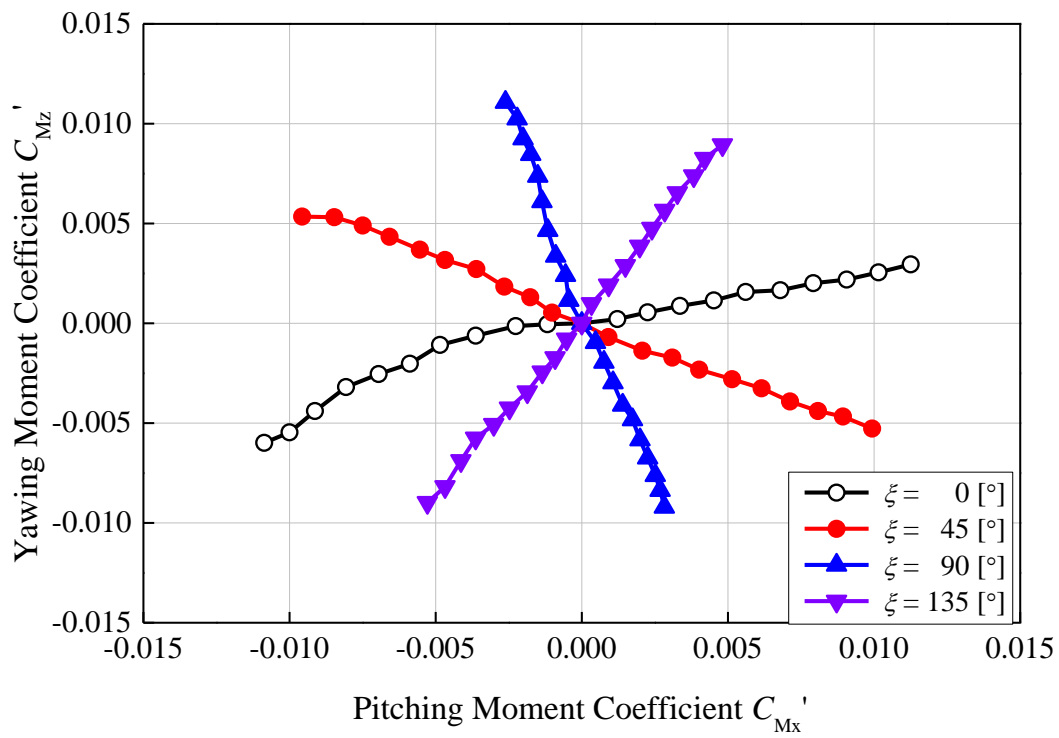


Fig. 6.44 Moment coefficient for cyclic pitch control of $\xi = 0^\circ, 45^\circ, 90^\circ$ and 135° .

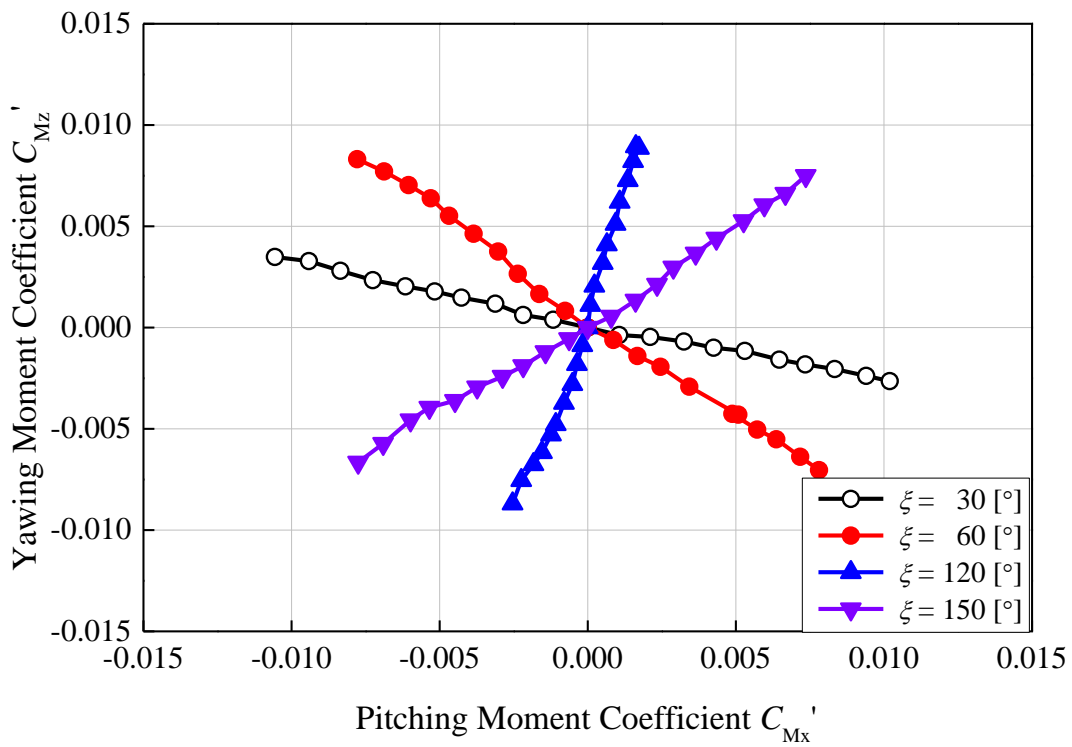


Fig. 6.45 Moment coefficient for cyclic pitch control of $\xi = 30^\circ, 60^\circ, 120^\circ$ and 150° .

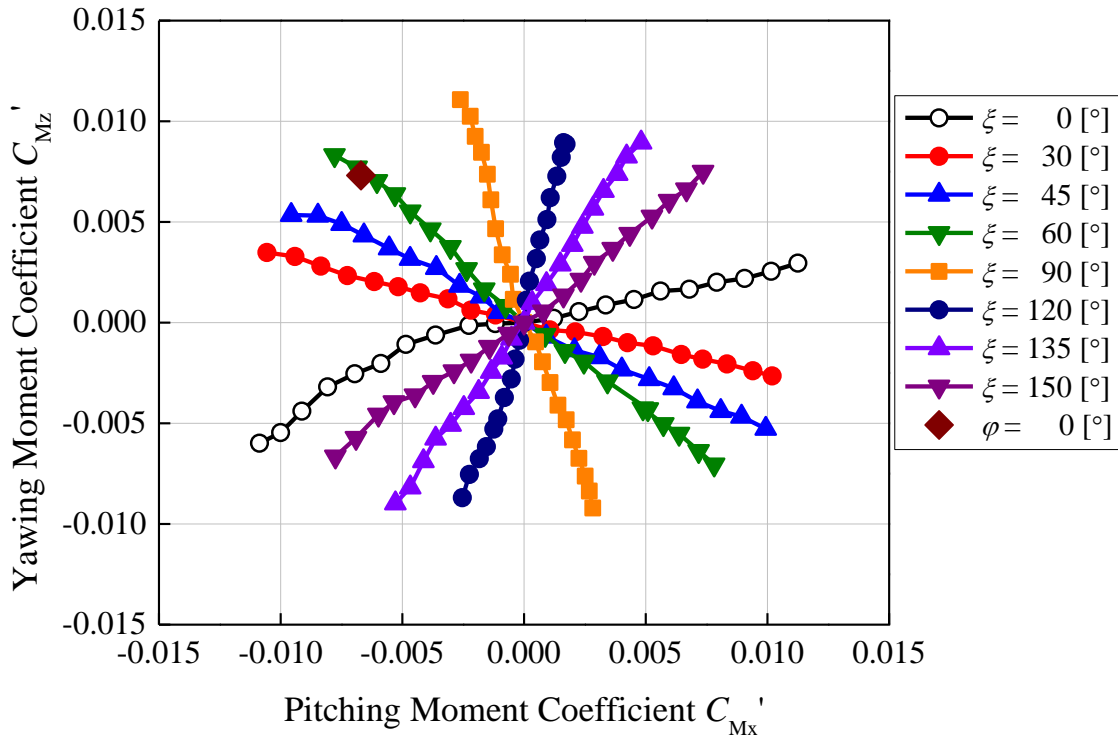


Fig. 6.46 Relationship between corrected yawing moment coefficient and corrected pitching moment coefficient in the cyclic pitch control as the phase angle changes

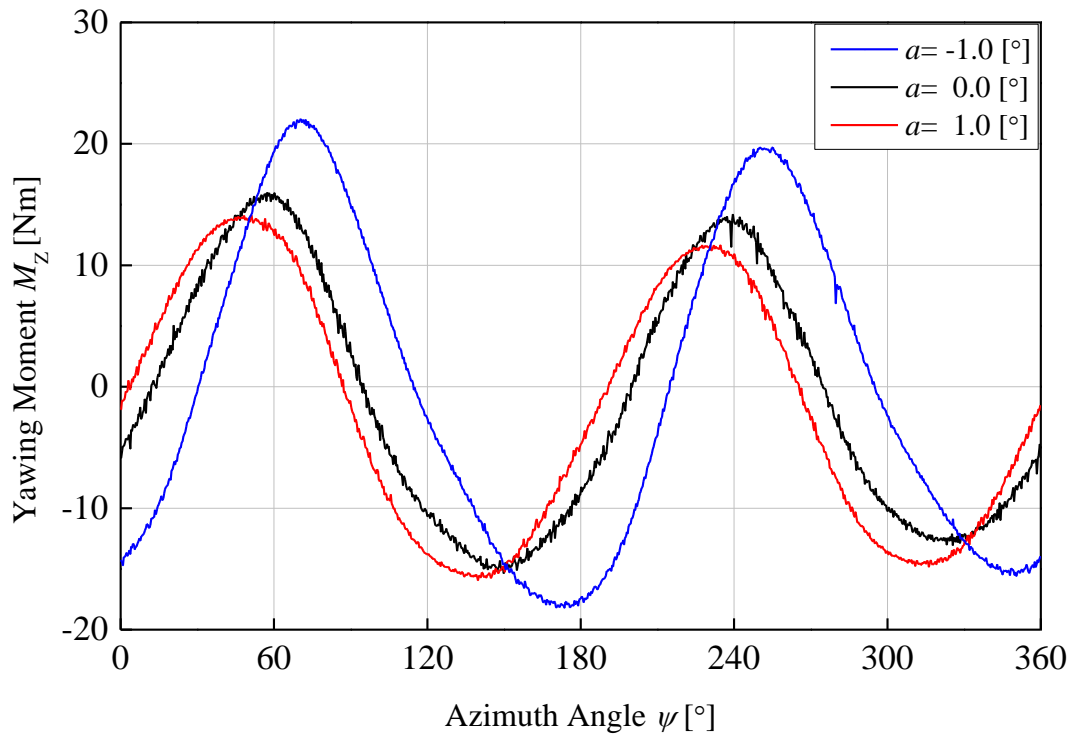


Fig. 6.47 Variation of yawing moment coefficient with respect to azimuth angle at the different pitch angle amplitudes in the cyclic pitch control and the pitch angle phase of $\xi = 45^\circ$.

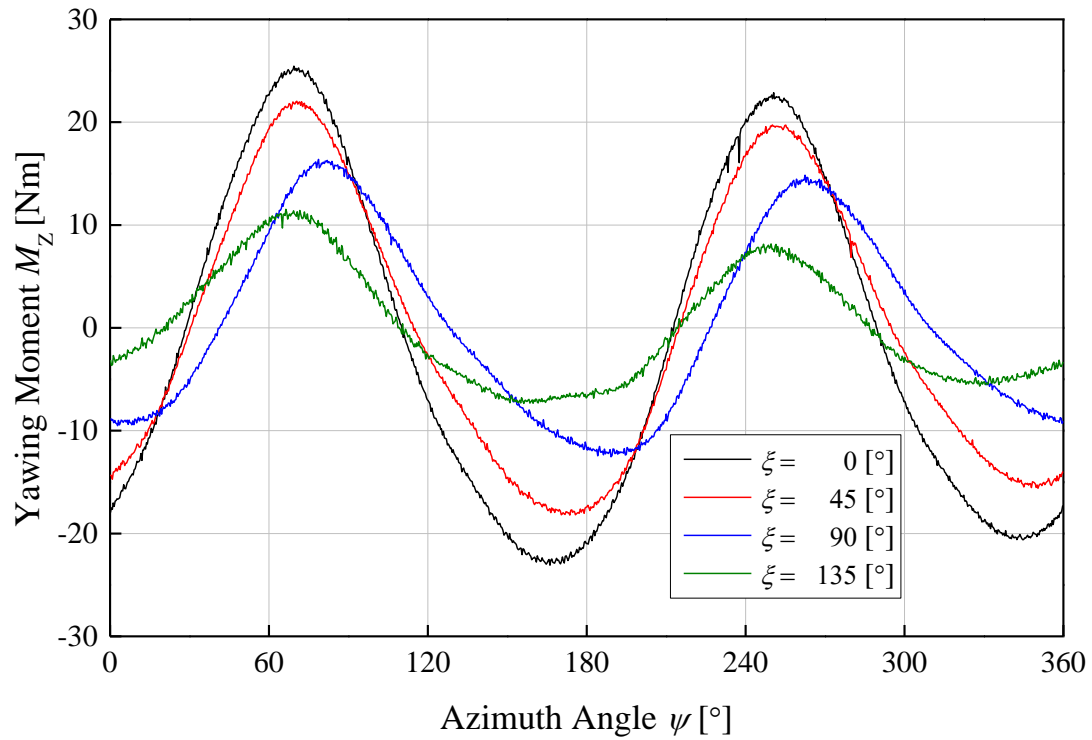


Fig. 6.48 Variation of yawing moment coefficient with respect to azimuth angle in the cyclic pitch control with different pitch angle phases at the pitch angle amplitude of $a = -1^\circ$.

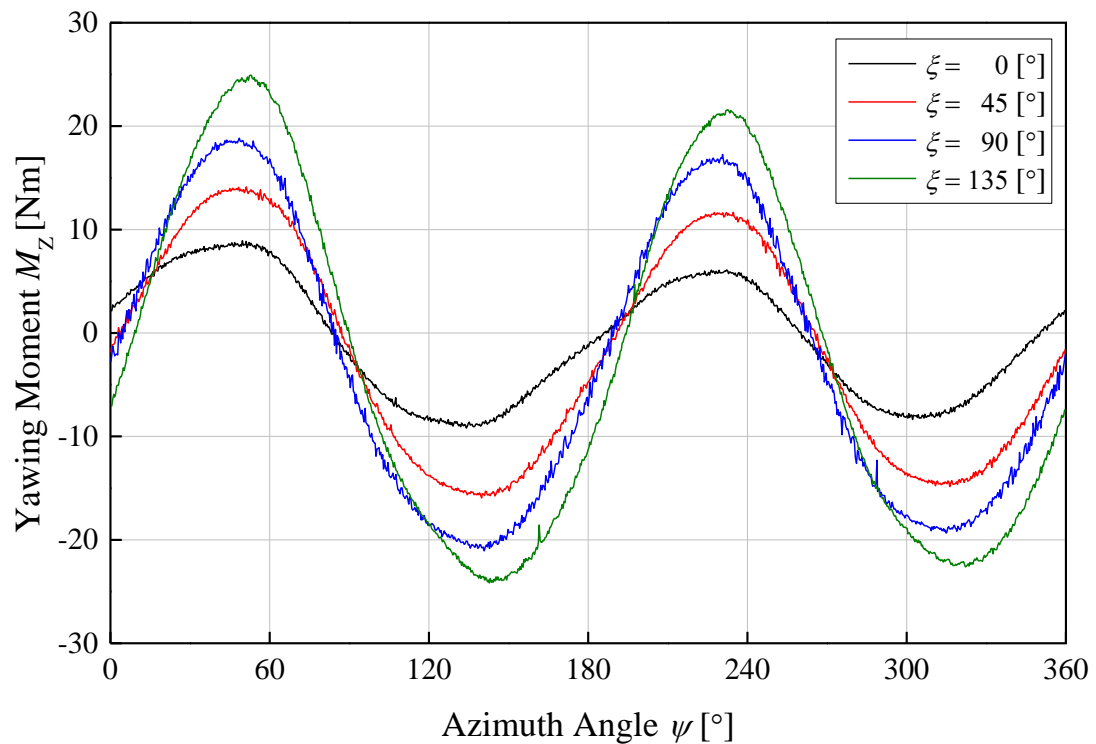


Fig. 6.49 Variation of yawing moment coefficient with respect to azimuth angle in the cyclic pitch control with different pitch angle phases at the pitch angle amplitude of $a = 1^\circ$.

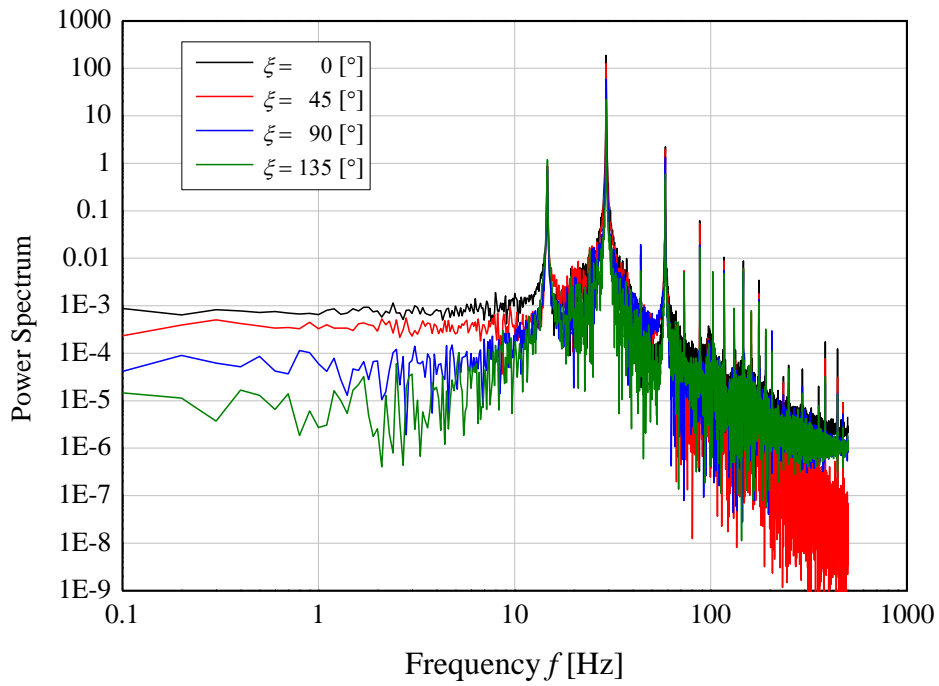


Fig. 6.50 Variations of spectra of the phase angles at the pitch angle amplitude $a = -1$

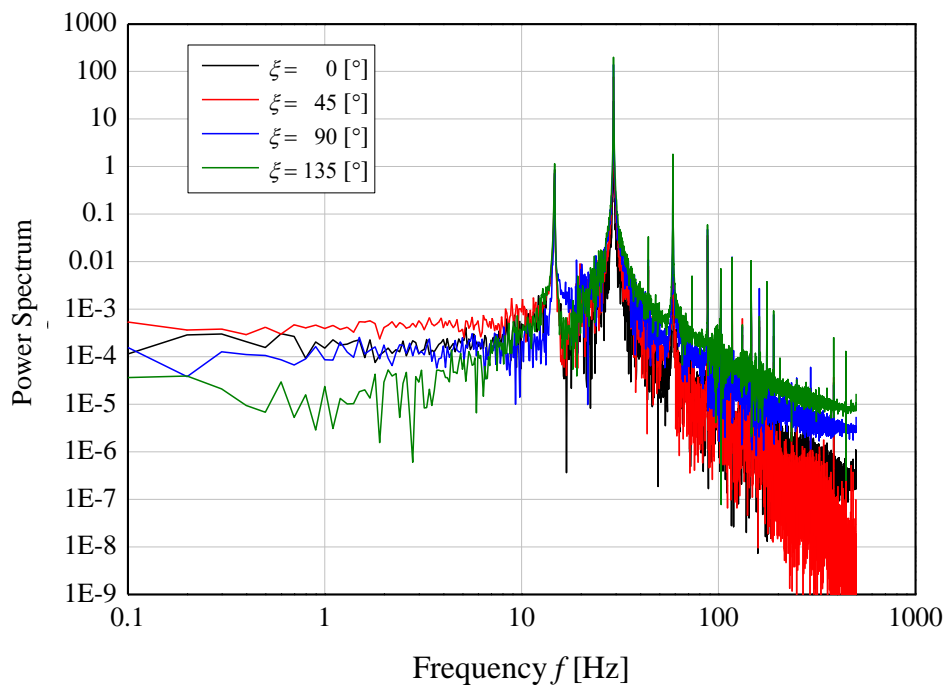


Fig. 6.51 Variations of spectra of the phase angles at the pitch angle amplitude $a = +1$

Table 6.1 Pitch control actuator specifications (DRS42SB2-04MK)

Maximum Thrust	[N]	150
Maximum Acceleration	[m/s ²]	0.4
Maximum Holding Power	[N]	150
Repeat Positioning Accuracy	[mm]	±0.005
Resolution	[mm]	0.002
Stroke	[mm]	40

Table 6.2 Experimental condition of cyclic pitch control experiment

Mainstream Wind Speed U [m/s]	Tip Speed Ratio λ	Pitch Angle θ [°]	Phase of Pitch Angle ξ [°]	Pitch Angle Change Amplitude a [°]	Yaw Angle φ [°]
10	7.4	0	0, 30, 45, 60, 90, 135, 150	-1 ~ 1	-5, 0, +5,

Chapter 7 Simulation results

In order to understand clearly the effect of the cyclic pitch control on the power coefficient, the simulation results are compared with the experimental data. The model wind turbine used in this experiment was simulated by FAST code. The simulation was performed in steady pitch control with the front inflow wind and the yawed inflow wind condition. Therefore, the analysis conditions of FAST were made consistent with each experimental condition. The input parameters in the analysis condition are the wind speed, the rotor rotation speed, the pitch angle, and the yaw angle, etc. The output parameters are C_P , C_T , tip speed ratio, the pitching moment of 2 blades, the yawing moment and so on. In this analysis, vibration analysis and turbulent inflow wind are not considered.

7.1 Input and Output Data of FAST Code

In the FAST Primary file has a format FAST.fst as seen in Fig. 7.1. The input parameters are the control conditions, analysis condition and design data. The design data includes the size of the blade, the nacelle and the tower, the weight, the drive train in the nacelle, and the specifications of the generator. In the FAST Tower file and Blade file, the input includes the rigidity, damping coefficient and mode shape etc. of each structure.

Fig 7.1 shows the main parameters entered in the FAST Primary file. The number of blades was 2, the rotor radius was 0.8 m, the blade root radius was 0.08 m, and the hub height was 1.535 m, which are the same configuration upwind tunnel experiment. The length and weight of the parts inside the nacelle were input based on the design data. In addition, because the mechanical rotor output is the subject of evaluation, no generator setting was made. Fig. 7.2 shows the parameters entered in the AeroDyn Primary file. In this simulation, the dynamic stalling effect and the dynamic meandering of the wake are not consider, and assume that the wake fall was calculated by BEM. The blade tip and blade root loss consider the tip loss coefficient suggested by Prandtl [50]. The influence of the tower is not considered. In addition, the blade shape, the twist angle and the chord length of the blade cross section shape were input. In AeroDyn's Airfoil input file, the Avistar blade performance of the two-dimensional wind tunnel experiment was entered. The Avistar blade performance was described in the Chapter 4. The calculation method of blade performance is a method of calculating from the lift and drag data of the input experiment value using the Viterna method [51]. AirfoilPrep is provided by NREL for creating AeroDyn's Airfoil input file. In the AeroDyn Wind file, the inflow wind was uniform. The inflow wind speed was steady, the wind direction to the wind turbine was set up -5° , 0° , 5° and the wind without horizontal-vertical shear and turbulence wind were assumed. Fig. 7.3 indicates the form of the output data. Depending on purpose of the research, the output data will be selected suitable.

For the steady pitch control simulation, the wind speed and the pitch angle change is kept constant, the rotation speed and the yaw angle were changed. The power and thrust coefficients are selected.

For the cyclic pitch control simulation, the wind speed and the number of revolutions were set, and the pitch angle was periodically changed. Considering the relation of the pitch angle and the azimuth angle. Table 7.1 shows the pitch angle changes following the azimuth angle at the pitch angle amplitude $a = 1$ and the phase $\xi = 45^\circ$. As shown in Fig. 7.4, the process of simulation for cyclic pitch control is performed by FAST. The cyclic pitch change was analyzed assuming a quasi-state state. First, an arbitrary azimuth angle position is set, and the pitch angle of the rotor blade at the azimuth angle position is calculated. The pitch angle of the calculated rotor blades 1 and 2 is input respectively, and steady state analysis is performed. Then, from the output data, the moment acting on the rotor blade at the set azimuth angle position is extracted. By repeating this process every $\psi = 10^\circ$ until the azimuth angle of $\psi = 360^\circ$, the pitch angle variation is simulated when the rotor blades rotate once. Also, the time step of the analysis is 0.001 second, and the azimuth angle resolution of the output data is 5.28° . Therefore, it can be said that the cyclic pitch change in the quasi-steady state is reproducible.

The experimental result is used to compare with FAST analysis results. This simulation analysis is carried out under the same experimental conditions as follow:

- Performance and thrust coefficient:
The wind conditions are the front inflow wind and the yawed inflow wind. In this analysis, the wind speed and pitch angle were set, and the rotation speed and the yaw angle were changed.
- Load characteristic of the cyclic pitch control:
The wind condition is front inflow wind. The wind speed and the number of revolutions were set, and the pitch angle was periodically changed.

7.2 Simulation Results and Experimental Data

Fig. 7.5 and Fig. 7.6 compare the simulation results of the power coefficient and the thrust coefficient with the experimental data in the front inflow wind condition. The horizontal axis is the tip speed ratio, the vertical represents the power coefficient. Comparison is made between the simulation results at the pitch angle of $\theta = -1^\circ$ and 1° and the experimental data of $\theta = -1^\circ$ and 1° . From Fig. 7.5, for the pitch angle $\theta = 1^\circ$, the maximum power coefficient in the simulation result is $C_P = 0.421$ at the tip speed ratio of $\lambda = 7.42$, and for the pitch angle $\theta = -1^\circ$ is $C_P = 0.392$ at $\lambda = 7.42$. Maximum power coefficient in the experiment is $C_P = 0.397$ at $\lambda = 7.76$ and $C_P = 0.404$ at $\lambda = 7.1$ at the pitch angle of $\theta = 1^\circ$ and -1° , respectively. There are some difference between simulation analysis results and experimental data because the simulation is not possible to fully take into account the flow field caused by the separated flow on the blade surface in the simulated analysis. The power coefficient of the simulation analysis results at $\theta = -1^\circ$ is smaller than the experimental data at low tip speed ratio. The power coefficient of the simulation result at the pitch angle $\theta = 1^\circ$ is higher than the experimental value at the optimum tip speed ratio. It is in good agreement in the low tip speed ratio and high tip speed ratio.

The comparison of the simulation analysis results of the thrust coefficient with the experimental value in the front inflow wind condition is shown in Fig. 7.6. The horizontal axis shows the tip speed ratio, the vertical is the thrust coefficient. Similarly with the power coefficient of $\theta = -1^\circ$ and 1° are considered. In this figure, the thrust coefficient in the simulation result at the pitch angle of $\theta = -1^\circ$ is $C_T = 0.839$, that $\theta = 1^\circ$ is $C_T = 0.789$ in $\lambda = 7.42$. The thrust coefficient in the experiment is $C_T = 0.709$ at $\lambda = 7.41$ and $C_T = 0.779$ at $\lambda = 7.1$ at the pitch angle of $\theta = 1^\circ$ and -1° , respectively. The thrust coefficient of the simulation analysis results is in good agreement with the experimental values in the vicinity of the optimum tip speed ratio. Therefore, it can be considered reasonable to predict the wind turbine performance in the front inflow wind by FAST, which was used in this study.

Fig. 7.7 indicates the simulation results of the power coefficient of the wind turbine and the experimental values in the yawed flow wind condition. From this figure, the maximum power coefficient at the yaw angle deviation of $\varphi = -5^\circ$ of the simulation analysis result is $C_P = 0.407$ in $\lambda = 7.42$. The maximum power coefficient of the yaw angle deviation of $\varphi = -5^\circ$ in the experiment is $C_P = 0.398$ in $\lambda = 7.43$. In addition, the maximum power coefficient of the yaw angle deviation of $\varphi = 5^\circ$ in the simulation analysis result is $C_P = 0.369$ in $\lambda = 7.42$. The maximum power coefficient of the yaw angle deviation of $\varphi = 5^\circ$ in the experiment is $C_P = 0.399$ in $\lambda = 7.36$. The simulation analysis results of the power coefficient are largely consistent with the experimental values in the vicinity of the optimum tip speed ratio.

Fig. 7.8 shows the simulation analysis results of the thrust coefficient and the experimental data in the yawed flow condition. The thrust coefficient of the simulation analysis result in the yaw angle deviation of $\varphi = 5^\circ$ and -5° at the optimum tip speed ratio is $C_T = 0.852$ and 0.815 , respectively. The thrust coefficient of the experiment in the yaw angle deviation of $\varphi = 5^\circ$ and -5° at the optimum tip speed ratio is $C_T = 0.773$ and 0.734 , respectively. The simulated analysis results of the thrust coefficient are also largely consistent with the experimental values in the vicinity of the optimum tip speed ratio. In a similar way with in the front inflow wind condition, the wind turbine performance prediction in the yawed flow wind condition by FAST, which was used in this simulation, can be considered reasonable.

Fig. 7.9 and Fig. 7.10 show the simulation results of the validity of pitching moment with respect to the cyclic pitch control for frontal wind. In each figure, the horizontal axis represents the pitch angle change amplitude a , and the vertical axis is the pitching moment M_x . Fig. 7.9 indicates the case when the pitch angle phase is $\xi = 0^\circ$ and 45° . Fig. 7.10 exhibits the pitch angle phase $\xi = 90^\circ$ and 135° . As shown in Fig. 7.9, at the $\xi = 0^\circ$, it can be seen that the analysis values roughly agrees with the experimental value although a slight difference occurs due to increasing or

decreasing of the pitch angle variation amplitude. At the $\xi = 45^\circ$, the analytical values are linearly changed as well as the experimental values, which are in good agreement. From Fig. 7.10, for the $\xi = 90^\circ$, the analytical value takes a nearly constant value, but the experimental value changes linearly. This is considered that it can be a structural error of the pitch angle changing mechanism of the test wind turbine. It is also considered that this is caused by the influence of the tower downstream flowing into the rotor. For the $\xi = 135^\circ$, the analytical value varies linearly like the experimental value, but there is slight difference compared with the experimental data.

Fig. 7.11 and Fig. 7.12 indicate the simulation results of the yawing moment with respect to the pitch angle amplitude in the front inflow wind condition. In each figure, the horizontal axis represents the pitch angle variation amplitude a , and the vertical axis is the yawing moment M_z . Fig. 7.11 exhibits the phase angle of the pitch angle $\xi = 0^\circ$ and 45° , Fig. 7.12 displays the phase angle of the pitch angle $\xi = 90^\circ$ and 135° of the pitch angle. From Fig. 7.11, for the $\xi = 0^\circ$, the experimental values are changing linearly, but the analysis value takes a nearly constant value. In this simulation, the influence of the tower is not considered, so the analysis value is nearly constant. For $\xi = 45^\circ$, the fluctuation of analysis results and the experimental value is larger than in the range where the change amplitude is negative. From Fig. 7.12, the analysis values well agrees with the experimental value at the $\xi = 135^\circ$. At the $\xi = 90^\circ$, in the region where the change amplitude is negative, the fluctuation of analysis results and the experimental value is larger than positive region.

Fig. 7.13 and Fig. 7.14 show the simulation results of the pitching moment with respect to the pitch angle amplitude. Fig. 7.13 exhibits the phase angle of the pitch angle $\xi = 30^\circ$ and 60° , the experimental value is considered changing linearly, however they have a slight wave. It can be seen the influence of the structural error of the pitch angle changing mechanism of the test wind turbine. But the simulation values well agree the experimental value. Fig. 7.14 shows the simulation results near with the experimental value for $\xi = 120^\circ$ and 150° . From this figure, the experimental results are quite linear, they also have a little wave and smaller than the cases of the phase angles $\xi = 30^\circ$ and 60° . These can be seen the impact of the structural error and the phase angle.

Fig. 7.15 and Fig. 7.16 show the simulation results of the yawing moment with respect to the pitch angle amplitude. Fig. 7.15 shows the phase angle of the pitch angle $\xi = 30^\circ$ and 60° , Fig. 7.16 displays the phase angle of the pitch angle $\xi = 120^\circ$ and 150° of the pitch angle. From Fig. 7.15, the experimental values are larger fluctuation than the simulated results because the experimental values is effected by the tower shadow, but the analysis value has trend the same with the experimental data. Fig. 7.16, at the $\xi = 120^\circ$, the simulation value well agrees with the experimental value in the range where the change amplitude is negative. At the $\xi = 150^\circ$, the simulation value is slight difference. This difference is considered that it is caused by the influence of the tower downstream flowing into the rotor. However, the simulation values well agree the experimental value.

```

Avistar.fst - Notepad
File Edit Format View Help
----- FAST INPUT FILE -----
FAST certification Test #01: AWT-27CR2 with many DOFs with fixed yaw error and stey wind.
Compatible with FAST v7.00.00.
----- SIMULATION CONTROL -----
False      Echo      - Echo input data to ""echo.out"" (flag)
1          ADAMSprep - ADAMS preprocessor mode {1: Run FAST, 2: use FAST as a preprocessi
1          AnalMode - Analysis mode {1: Run a time-marching simulation, 2: create a per
2          NumBl   - Number of blades (-)
10.0      TMax     - Total run time (s)
0.001     DT      - Integration time step (s)
----- TURBINE CONTROL -----
0          YCMode   - Yaw control mode {0: none, 1: user-defined from routine UserYawCon
9999.9    TYCON   - Time to enable active yaw control (s) [unused when YCMode=0]
0          PCMode   - Pitch control mode {0: none, 1: user-defined from routine PitchCN
0.0       TPCON   - Time to enable active pitch control (s) [unused when PCMode=0]
0         VSContrl - Variable-speed control mode {0: none, 1: simple VS, 2: user-defin
9999.9    VS_RtGnSp - Rated generator speed for simple variable-speed generator control
9999.9    VS_RTtq  - Rated generator torque/constant generator torque in Region 3 for :
9999.9    VS_Rgn2K - Generator torque constant in Region 2 for simple variable-speed g
9999.9    VS_sIPc  - Rated generator slip percentage in Region 2 1/2 for simple variab
1         GenModel - Generator model {1: simple, 2: Thevenin, 3: user-defined from rou
True      GenTistr - Method to start the generator {T: timed using TimGenOn, F: genera
True      GenTistp - Method to stop the generator {T: timed using TimGenOf, F: when ge
9999.9    SpdGenOn - Generator speed to turn on the generator for a startup (HSS speed)
0.0      TimGenOn - Time to turn on the generator for a startup (s) [used only when G
600      TimGenOf - Time to turn off the generator (s) [used only when GenTistp=True]
1        HSSBrMode - HSS brake model {1: simple, 2: user-defined from routine UserHSSB
9999.9    THSSBrDp - Time to initiate deployment of the HSS brake (s)
9999.9    TIdynBrk - Time to initiate deployment of the dynamic generator brake [CURRE
9999.9    TTPBrDp(1) - Time to initiate deployment of brake 1 (s)
9999.9    TTPBrDp(2) - Time to initiate deployment of tip brake 2 (s)
9999.9    TTPBrDp(3) - Time to initiate deployment of tip brake 3 (s) [unused for 2 blad
9999.9    TBDepISp(1) - Deployment-initiation speed for the tip brake on blade 1 (rpm)
9999.9    TBDepISp(2) - Deployment-initiation speed for the tip brake on blade 2 (rpm)
9999.9    TBDepISp(3) - Deployment-initiation speed for the tip brake on blade 3 (rpm) [u
9999.9    TYawManS - Time to start override yaw maneuver and end standard yaw control
9999.9    TYawManE - Time at which override yaw maneuver reaches final yaw angle (s)
0.0      NacYawF  - Final yaw angle for yaw maneuvers (degrees)
9999.9    TPitManS(1) - Time to start override pitch maneuver for blade 1 and end standar
9999.9    TPitManS(2) - Time to start override pitch maneuver for blade 2 and end standar
9999.9    TPitManS(3) - Time to start override pitch maneuver for blade 3 and end standar
9999.9    TPitManE(1) - Time at which override pitch maneuver for blade 1 reaches final p
9999.9    TPitManE(2) - Time at which override pitch maneuver for blade 2 reaches final p
9999.9    TPitManE(3) - Time at which override pitch maneuver for blade 3 reaches final p
0.0      BlPitch(1) - Blade 1 initial pitch (degrees)
0.0      BlPitch(2) - Blade 2 initial pitch (degrees)
Ln 15, Col 36

```

Fig. 7.1 The input parameters of the FAST Primary file

Load and Power Control of Horizontal Axis Wind Turbine

```

Avistar_AD.ipt - Notepad
File Edit Format View Help
Avistar_AD.ipt aerodynamic parameters for FAST certification test #1.
SI SysUnits - System of units for used for input and out
STEADY StallMod - Dynamic stall included [BEDDOES or STEADY]
NO_CM UseCm - Use aerodynamic pitching moment model? [U]
EQUIL InFModel - Inflow model [DYNIN or EQUIL] (unquoted s
SWIRL InModel - Induction-factor model [NONE or WAKE or SI
0.005 AToler - Induction-factor tolerance (convergence c
PRANDTL TLModel - Tip-loss model (EQUIL only) [PRANDTL, GTE
PRANDTL HLModel - Hub-loss model (EQUIL only) [PRANDTL or N
"D:\2-blade\windfield\10.wnd" windFile - Name of file containing wind data (quoted :
1.600 HH - wind reference (hub) height [TowerHt+Twr2:
0.0 TwrShad - Tower-shadow velocity deficit (-)
9999.9 ShadHwid - Tower-shadow half width (m)
9999.9 T_Shad_Refpt - Tower-shadow reference point (m)
1.205 AirDens - Air density (kg/m^3)
1.512e-5 KinVisc - Kinematic air viscosity (m^2/sec)
0.05 DTAero - Time interval for aerodynamic calculation:
2 NumFoil - Number of airfoil files (-)
"D:\3bladed\avister1.dat" FoilNm - Names of the airfoil files [NumFoil lines] (quoted
"D:\3bladed\RootCircle_Re95E4.dat" PrnElm
10 BldNodes - Number of blade nodes used for analysis
RNodes AeroTwst DRNodes Chord NFOil PrnElm
0.08 0 0.03 0.025 2 PRINT
0.16 16.73 0.13 0.167 1 PRINT
0.26 10.43 0.07 0.126 1 PRINT
0.32 6.93 0.05 0.099 1 PRINT
0.40 4.73 0.11 0.080 1 PRINT
0.48 3.23 0.05 0.067 1 PRINT
0.56 2.13 0.11 0.058 1 PRINT
0.64 1.23 0.05 0.051 1 PRINT
0.72 0.63 0.11 0.045 1 PRINT
0.79 0.13 0.03 0.040 1 PRINT
Ln1, Col1
    
```

Fig. 7.2 The input parameters of the Aerodyn file

```

880.out - Notepad
File Edit Format View Help
These predictions were generated by FAST (v7.01.00a-bjj, 16-Feb-2012) on 29-Sep-2017 at 00:16:51.
The aerodynamic calculations were made by Aerodyn (v13.00.01a-bjj, 16-Feb-2012).
FAST certification Test #01: AWT-27CR2 with many DOFs with fixed yaw error and stey wind.
Time Azimuth uwind PtchPMzC1 PtchPMzC2 RotSpeed TSR RotCq RotCp RotCt RotPwr GenPwr TFinAlpha NacYawP RootFxb1 RootFxb
(s) (deg) (m/s) (deg) (deg) (rpm) (-) (-) (-) (kw) (kw) (deg) (deg) (kn) (kn) (kn) (kn) (kn) (kn)
0.001 0.5280E+03 0.1000E+02 0.0000E+00 0.0000E+00 0.8800E+03 0.7418E+01 0.8087E-01 0.5999E+00 0.8612E+00 0.7358E
0.002 0.1456E+02 0.1000E+02 0.0000E+00 0.0000E+00 0.8800E+03 0.7418E+01 0.8088E-01 0.6000E+00 0.8612E+00 0.7359E
0.003 0.1584E+02 0.1000E+02 0.0000E+00 0.0000E+00 0.8800E+03 0.7418E+01 0.8091E-01 0.6002E+00 0.8612E+00 0.7362E
0.004 0.2112E+02 0.1000E+02 0.0000E+00 0.0000E+00 0.8800E+03 0.7418E+01 0.8088E-01 0.6000E+00 0.8612E+00 0.7359E
0.005 0.2640E+02 0.1000E+02 0.0000E+00 0.0000E+00 0.8800E+03 0.7418E+01 0.8089E-01 0.6000E+00 0.8612E+00 0.7360E
0.006 0.3168E+02 0.1000E+02 0.0000E+00 0.0000E+00 0.8800E+03 0.7418E+01 0.8090E-01 0.6001E+00 0.8612E+00 0.7361E
0.007 0.3696E+02 0.1000E+02 0.0000E+00 0.0000E+00 0.8800E+03 0.7418E+01 0.8087E-01 0.5999E+00 0.8612E+00 0.7359E
0.008 0.4224E+02 0.1000E+02 0.0000E+00 0.0000E+00 0.8800E+03 0.7418E+01 0.8092E-01 0.6003E+00 0.8612E+00 0.7363E
0.009 0.4752E+02 0.1000E+02 0.0000E+00 0.0000E+00 0.8800E+03 0.7418E+01 0.8086E-01 0.5999E+00 0.8612E+00 0.7358E
0.010 0.5280E+02 0.1000E+02 0.0000E+00 0.0000E+00 0.8800E+03 0.7418E+01 0.8080E-01 0.5994E+00 0.8612E+00 0.7352E
0.011 0.5808E+02 0.1000E+02 0.0000E+00 0.0000E+00 0.8800E+03 0.7418E+01 0.8088E-01 0.6000E+00 0.8612E+00 0.7360E
0.012 0.6336E+02 0.1000E+02 0.0000E+00 0.0000E+00 0.8800E+03 0.7418E+01 0.8089E-01 0.6001E+00 0.8612E+00 0.7361E
0.013 0.6864E+02 0.1000E+02 0.0000E+00 0.0000E+00 0.8800E+03 0.7418E+01 0.8086E-01 0.5999E+00 0.8612E+00 0.7358E
0.014 0.7392E+02 0.1000E+02 0.0000E+00 0.0000E+00 0.8800E+03 0.7418E+01 0.8089E-01 0.6000E+00 0.8612E+00 0.7360E
0.015 0.7920E+02 0.1000E+02 0.0000E+00 0.0000E+00 0.8800E+03 0.7418E+01 0.8087E-01 0.5999E+00 0.8612E+00 0.7358E
0.016 0.8448E+02 0.1000E+02 0.0000E+00 0.0000E+00 0.8800E+03 0.7418E+01 0.8088E-01 0.6000E+00 0.8612E+00 0.7359E
0.017 0.8976E+02 0.1000E+02 0.0000E+00 0.0000E+00 0.8800E+03 0.7418E+01 0.8088E-01 0.6000E+00 0.8612E+00 0.7359E
0.018 0.9504E+02 0.1000E+02 0.0000E+00 0.0000E+00 0.8800E+03 0.7418E+01 0.8089E-01 0.6000E+00 0.8612E+00 0.7360E
0.019 0.1003E+03 0.1000E+02 0.0000E+00 0.0000E+00 0.8800E+03 0.7418E+01 0.8085E-01 0.5998E+00 0.8612E+00 0.7357E
0.020 0.1056E+03 0.1000E+02 0.0000E+00 0.0000E+00 0.8800E+03 0.7418E+01 0.8092E-01 0.6003E+00 0.8612E+00 0.7363E
0.021 0.1109E+03 0.1000E+02 0.0000E+00 0.0000E+00 0.8800E+03 0.7418E+01 0.8091E-01 0.6002E+00 0.8612E+00 0.7362E
0.022 0.1162E+03 0.1000E+02 0.0000E+00 0.0000E+00 0.8800E+03 0.7418E+01 0.8085E-01 0.5998E+00 0.8612E+00 0.7357E
0.023 0.1214E+03 0.1000E+02 0.0000E+00 0.0000E+00 0.8800E+03 0.7418E+01 0.8091E-01 0.6002E+00 0.8612E+00 0.7362E
0.024 0.1267E+03 0.1000E+02 0.0000E+00 0.0000E+00 0.8800E+03 0.7418E+01 0.8091E-01 0.6003E+00 0.8612E+00 0.7363E
0.025 0.1320E+03 0.1000E+02 0.0000E+00 0.0000E+00 0.8800E+03 0.7418E+01 0.8088E-01 0.6000E+00 0.8612E+00 0.7359E
0.026 0.1373E+03 0.1000E+02 0.0000E+00 0.0000E+00 0.8800E+03 0.7418E+01 0.8089E-01 0.6000E+00 0.8612E+00 0.7360E
0.027 0.1426E+03 0.1000E+02 0.0000E+00 0.0000E+00 0.8800E+03 0.7418E+01 0.8085E-01 0.5997E+00 0.8612E+00 0.7356E
0.028 0.1478E+03 0.1000E+02 0.0000E+00 0.0000E+00 0.8800E+03 0.7418E+01 0.8093E-01 0.6003E+00 0.8612E+00 0.7364E
0.029 0.1531E+03 0.1000E+02 0.0000E+00 0.0000E+00 0.8800E+03 0.7418E+01 0.8083E-01 0.5997E+00 0.8612E+00 0.7355E
0.030 0.1584E+03 0.1000E+02 0.0000E+00 0.0000E+00 0.8800E+03 0.7418E+01 0.8085E-01 0.5997E+00 0.8612E+00 0.7356E
0.031 0.1637E+03 0.1000E+02 0.0000E+00 0.0000E+00 0.8800E+03 0.7418E+01 0.8085E-01 0.5998E+00 0.8612E+00 0.7357E
0.032 0.1690E+03 0.1000E+02 0.0000E+00 0.0000E+00 0.8800E+03 0.7418E+01 0.8088E-01 0.6000E+00 0.8612E+00 0.7360E
0.033 0.1742E+03 0.1000E+02 0.0000E+00 0.0000E+00 0.8800E+03 0.7418E+01 0.8089E-01 0.6001E+00 0.8612E+00 0.7361E
0.034 0.1795E+03 0.1000E+02 0.0000E+00 0.0000E+00 0.8800E+03 0.7418E+01 0.8088E-01 0.6000E+00 0.8612E+00 0.7359E
0.035 0.1848E+03 0.1000E+02 0.0000E+00 0.0000E+00 0.8800E+03 0.7418E+01 0.8089E-01 0.6000E+00 0.8612E+00 0.7360E
0.036 0.1901E+03 0.1000E+02 0.0000E+00 0.0000E+00 0.8800E+03 0.7418E+01 0.8089E-01 0.6001E+00 0.8612E+00 0.7361E
0.037 0.1954E+03 0.1000E+02 0.0000E+00 0.0000E+00 0.8800E+03 0.7418E+01 0.8088E-01 0.6000E+00 0.8612E+00 0.7359E
0.038 0.2006E+03 0.1000E+02 0.0000E+00 0.0000E+00 0.8800E+03 0.7418E+01 0.8091E-01 0.6003E+00 0.8612E+00 0.7363E
0.039 0.2059E+03 0.1000E+02 0.0000E+00 0.0000E+00 0.8800E+03 0.7418E+01 0.8086E-01 0.5999E+00 0.8612E+00 0.7358E
0.040 0.2112E+03 0.1000E+02 0.0000E+00 0.0000E+00 0.8800E+03 0.7418E+01 0.8085E-01 0.5998E+00 0.8612E+00 0.7357E
0.041 0.2165E+03 0.1000E+02 0.0000E+00 0.0000E+00 0.8800E+03 0.7418E+01 0.8084E-01 0.5997E+00 0.8612E+00 0.7355E
0.042 0.2218E+03 0.1000E+02 0.0000E+00 0.0000E+00 0.8800E+03 0.7418E+01 0.8091E-01 0.6002E+00 0.8612E+00 0.7362E
0.043 0.2270E+03 0.1000E+02 0.0000E+00 0.0000E+00 0.8800E+03 0.7418E+01 0.8085E-01 0.5998E+00 0.8612E+00 0.7357E
0.044 0.2323E+03 0.1000E+02 0.0000E+00 0.0000E+00 0.8800E+03 0.7418E+01 0.8088E-01 0.6000E+00 0.8612E+00 0.7359E
Ln1, Col1
    
```

Fig. 7.3 The output parameters of FAST

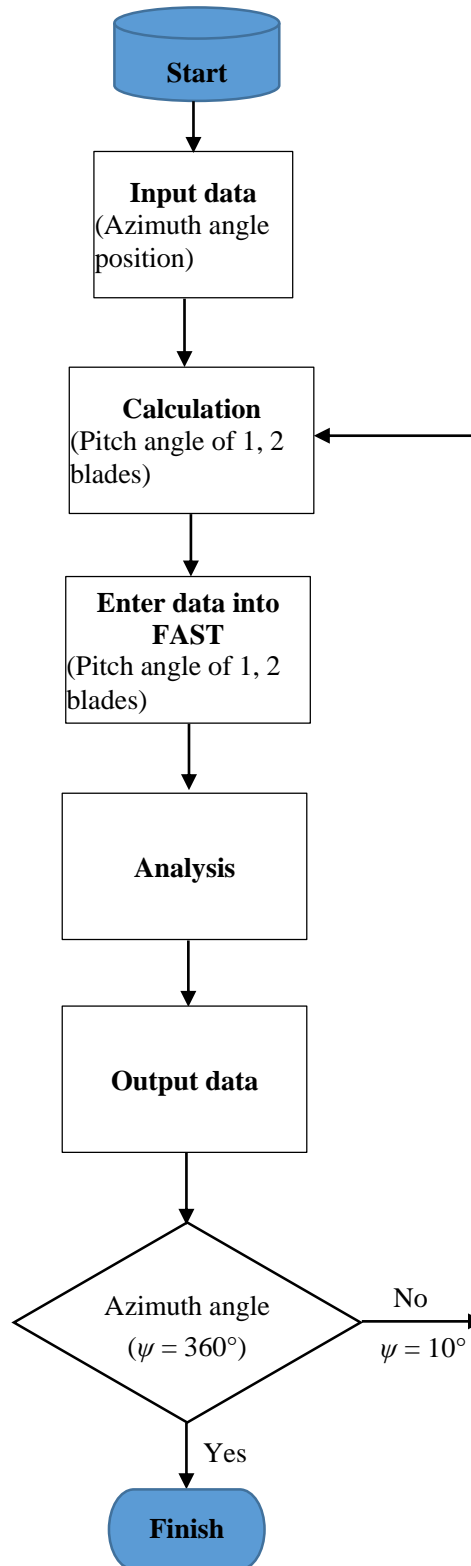


Fig. 7.4 Process of simulation for cyclic pitch control

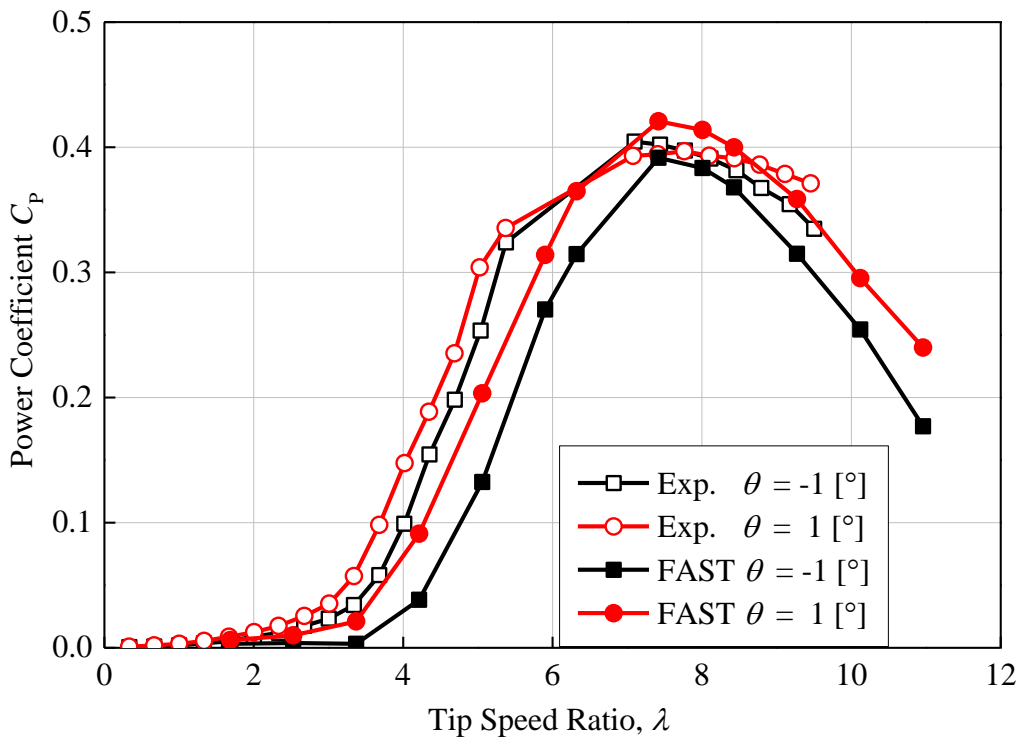


Fig. 7.5 Comparison of simulation results and experimental data of wind turbine power coefficient at the pitch angle $\theta = -1^\circ$ and 1°

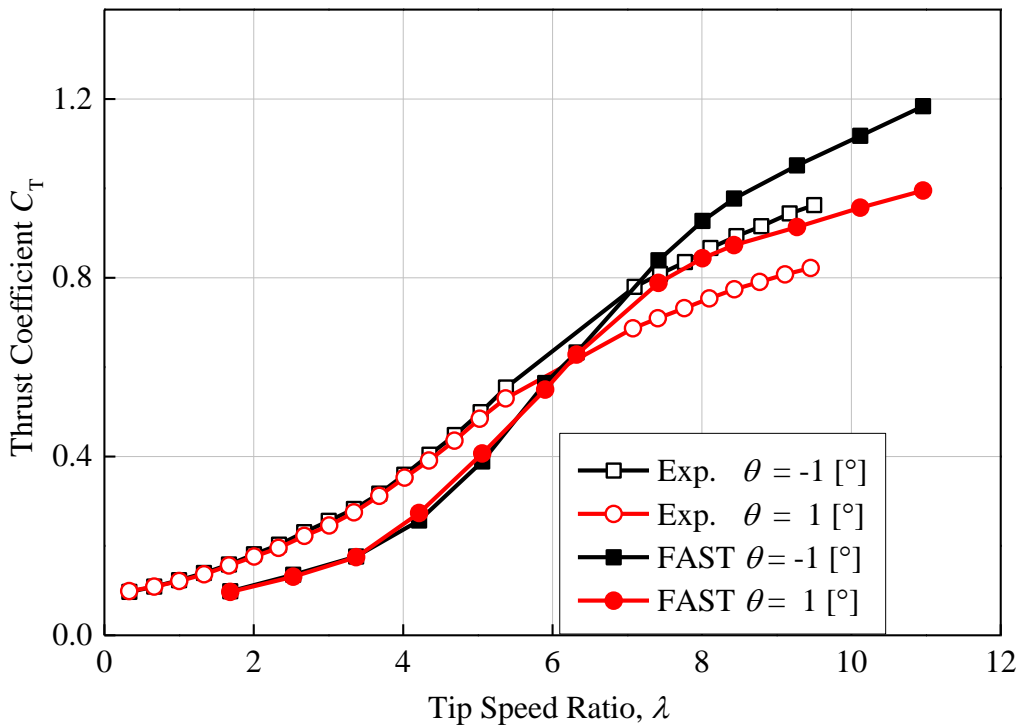


Fig. 7.6 Comparison of simulation results and experimental data of wind turbine thrust coefficient at the pitch angle $\theta = -1^\circ$ and 1°

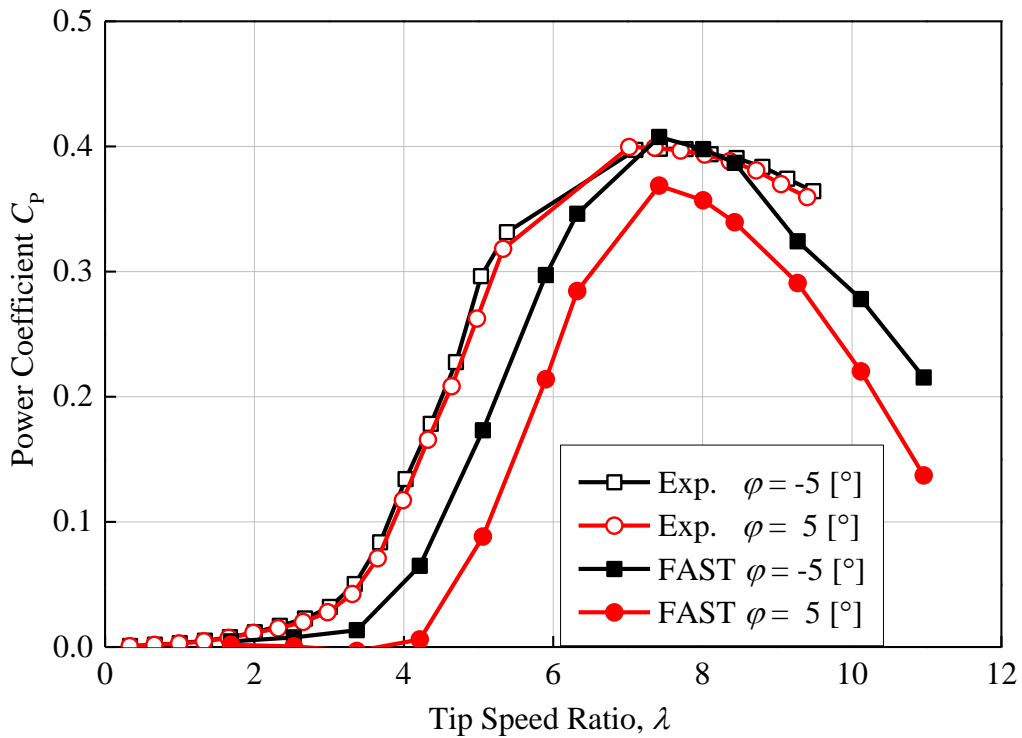


Fig. 7.7 Comparison of simulation results and experimental data of wind turbine power coefficient at the pitch angle $\varphi = -5^\circ$ and 5°

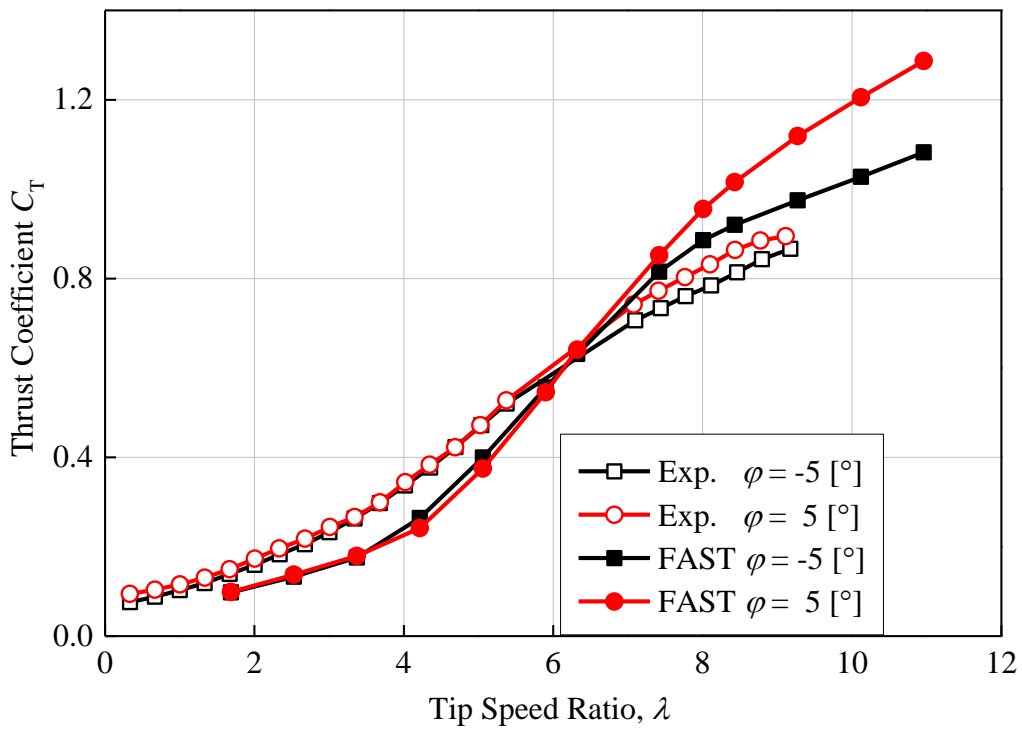


Fig. 7.8 Comparison of simulation results and experimental data of wind turbine thrust coefficient at the pitch angle $\varphi = -5^\circ$ and 5°

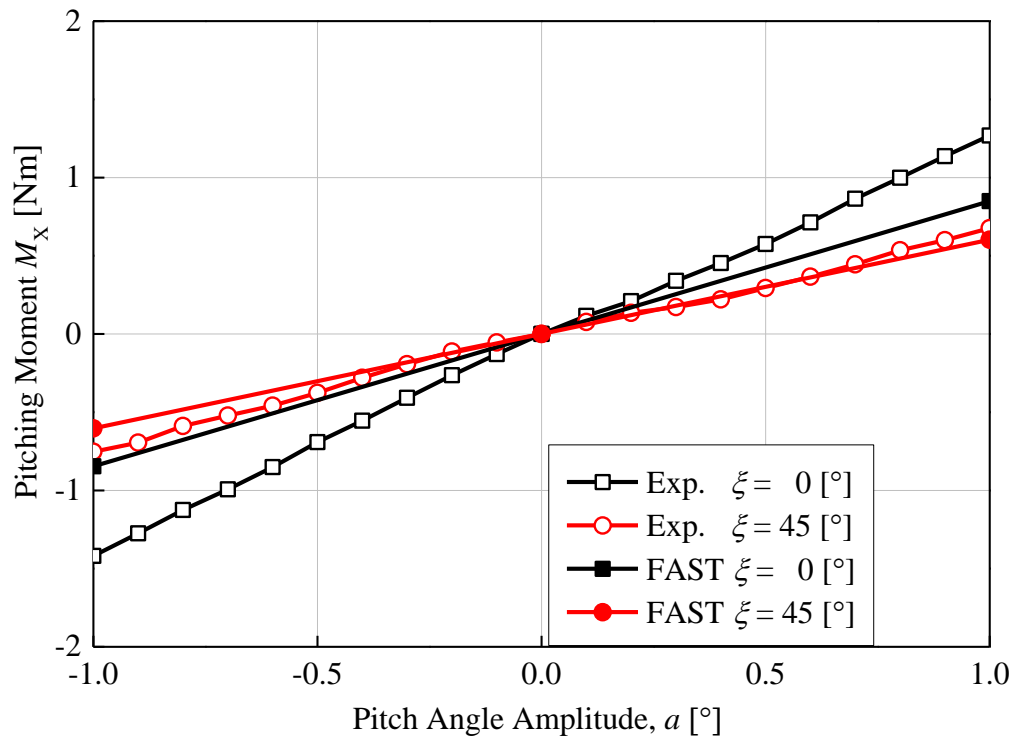


Fig. 7.9 Simulation results of pitching moment in the front inflow wind condition with $\xi = 0^\circ$ and 45°

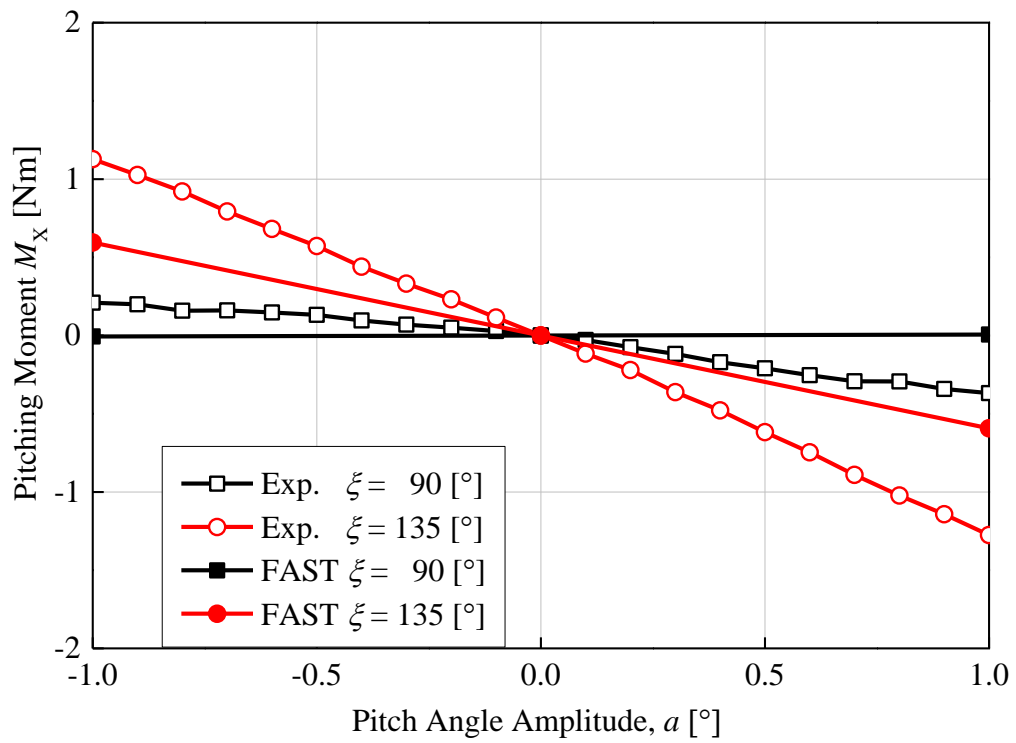


Fig. 7.10 Simulation results of pitching moment in front inflow wind condition with $\xi = 90^\circ$ and 135°

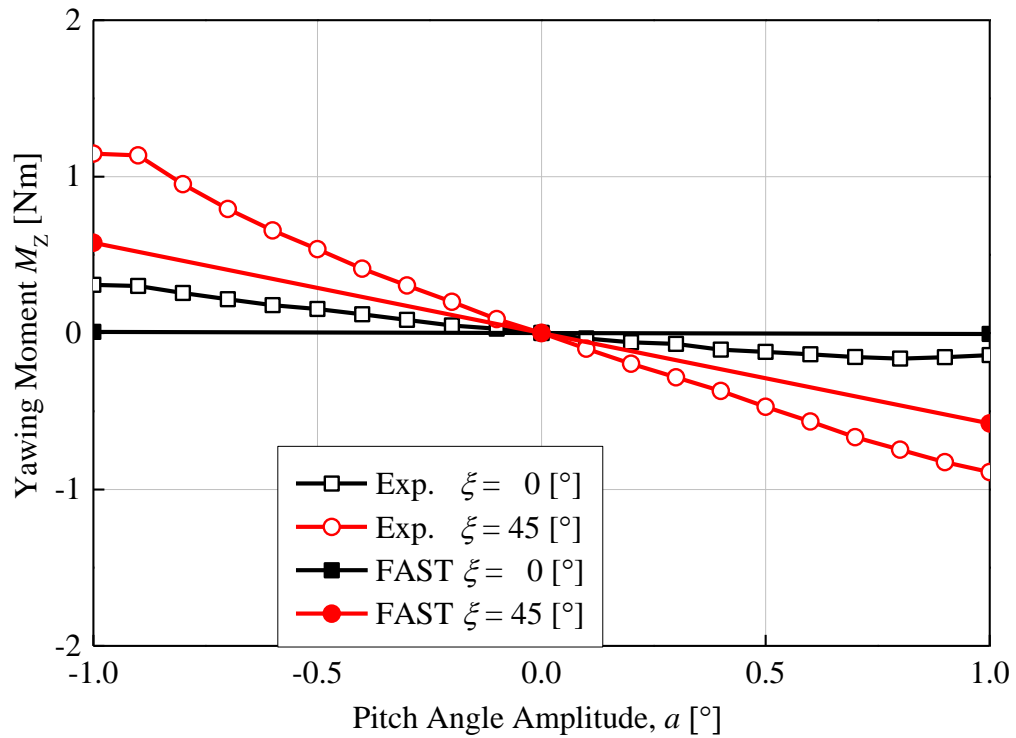


Fig. 7.11 Simulation results of yawing moment in front inflow wind condition with $\xi = 0^\circ$ and 45°

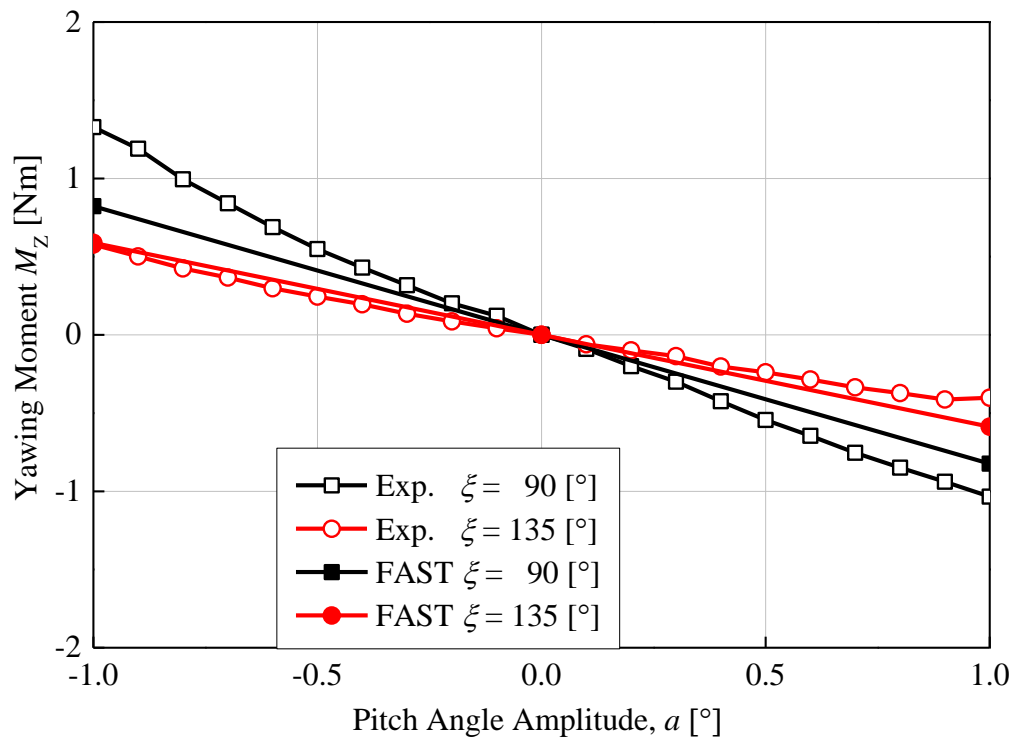


Fig. 7.12 Simulation results of yawing moment in front inflow wind condition with $\xi = 90^\circ$ and 135°

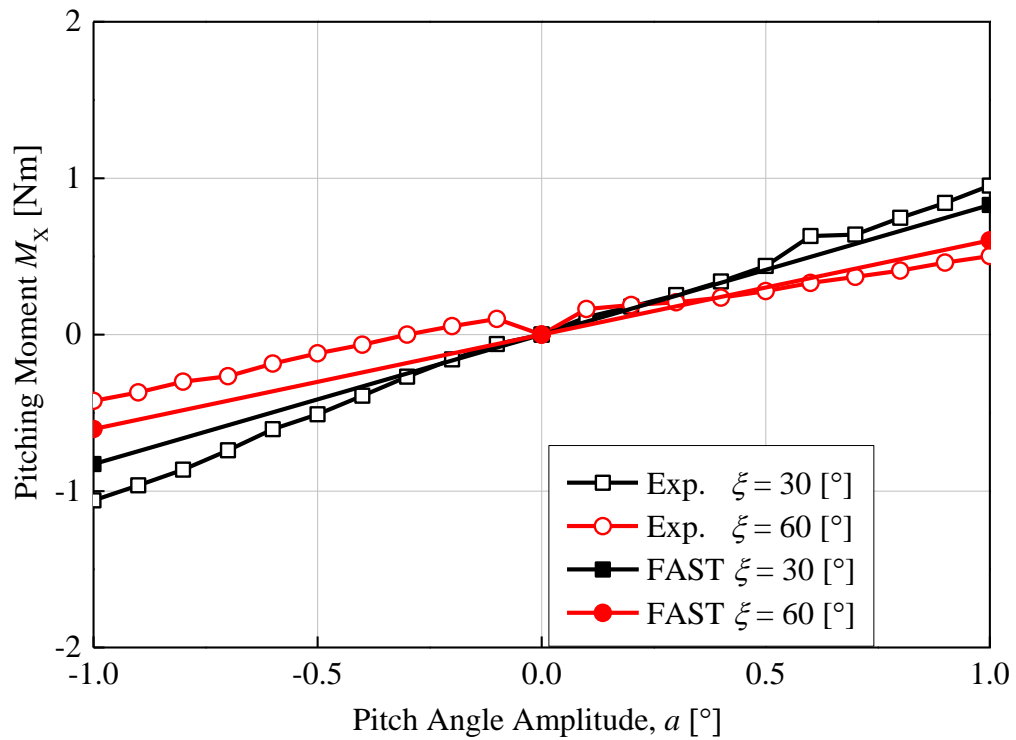


Fig. 7.13 Simulation results of pitching moment in front inflow wind condition with $\xi = 30^\circ$ and 60°

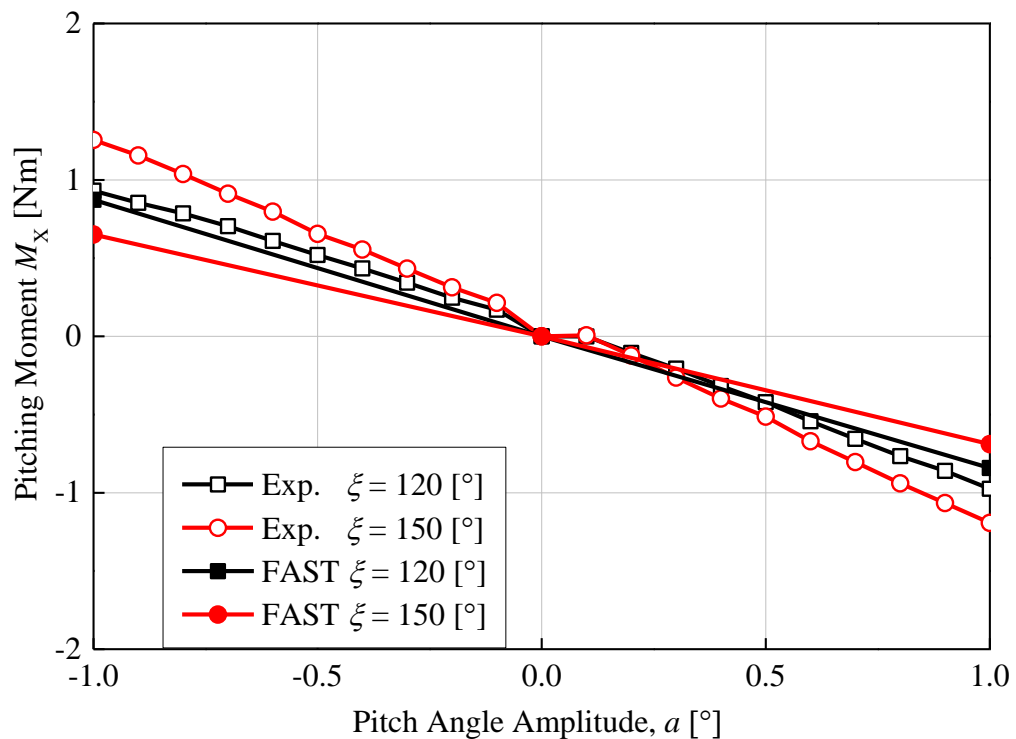


Fig. 7.14 Simulation results of pitching moment in front inflow wind condition with $\xi = 120^\circ$ and 150°

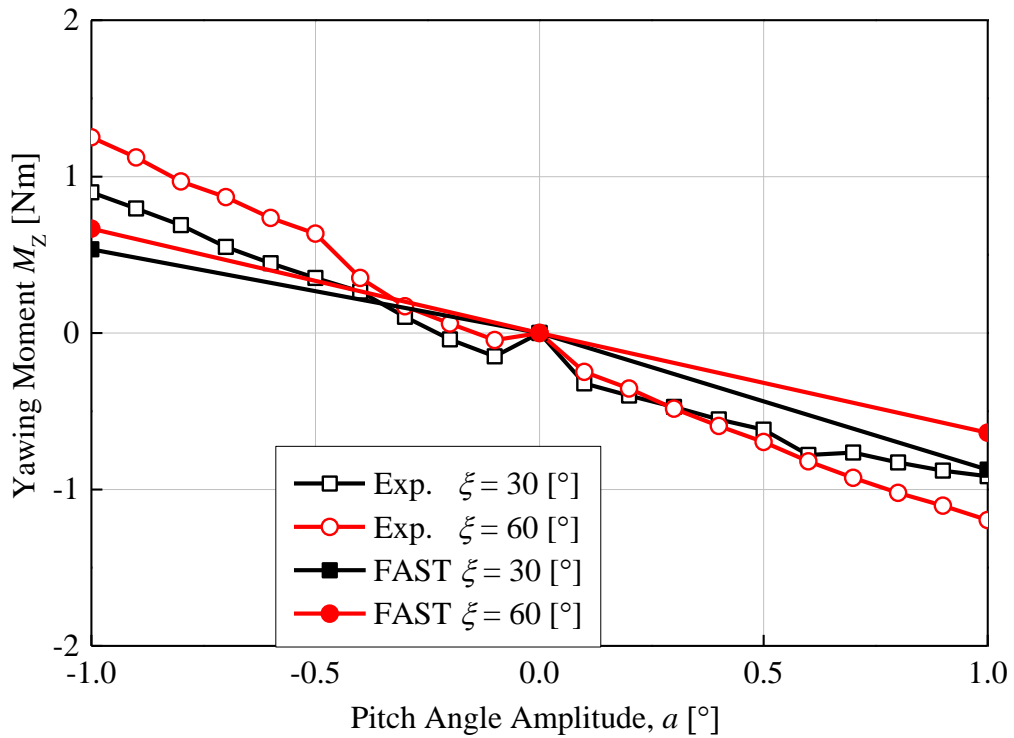


Fig. 7.15 Simulation results of yawing moment in front inflow wind condition with $\xi = 30^\circ$ and 60°

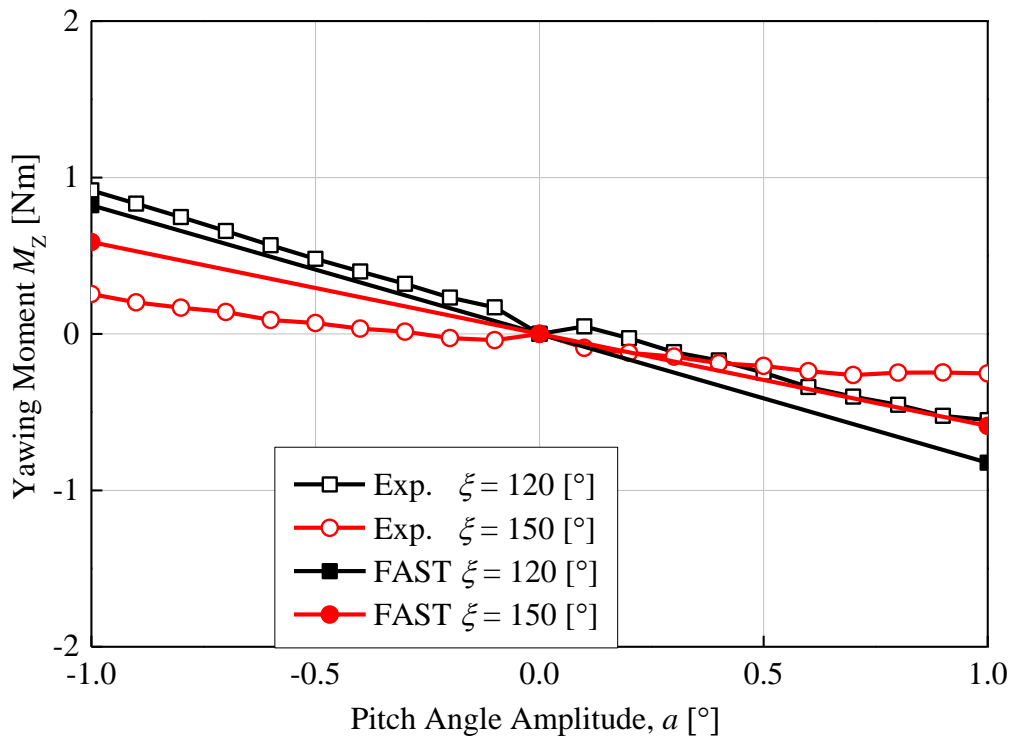


Fig. 7.16 Simulation results of yawing moment in front inflow wind condition with $\xi = 120^\circ$ and 150°

Table 7.1 Calculating pitch angle of blade 1, 2 at the angle phase of $\xi = 45^\circ$ and $\alpha = 1$

Azimuth angle (deg)	Azimuth angle (rad)	Pitch angle of Blade 1 (deg)	Pitch angle of Blade 2 (deg)	Azimuth angle (extraction)
0.0	-0.785	0.707	-0.707	315.0
5.0	-0.698	0.766	-0.766	310.0
10.0	-0.611	0.819	-0.819	305.0
15.0	-0.524	0.866	-0.866	300.0
20.0	-0.436	0.906	-0.906	295.0
25.0	-0.349	0.940	-0.940	290.0
30.0	-0.262	0.966	-0.966	285.0
35.0	-0.175	0.985	-0.985	280.0
40.0	-0.087	0.996	-0.996	275.0
45.0	0.000	1.000	-1.000	270.0
50.0	0.087	0.996	-0.996	265.0
55.0	0.175	0.985	-0.985	260.0
60.0	0.262	0.966	-0.966	255.0
65.0	0.349	0.940	-0.940	250.0
70.0	0.436	0.906	-0.906	245.0
75.0	0.524	0.866	-0.866	240.0
80.0	0.611	0.819	-0.819	235.0
85.0	0.698	0.766	-0.766	230.0
90.0	0.785	0.707	-0.707	225.0
95.0	0.873	0.643	-0.643	220.0
100.0	0.960	0.574	-0.574	215.0
110.0	1.134	0.423	-0.423	205.0
115.0	1.222	0.342	-0.342	200.0
120.0	1.309	0.259	-0.259	195.0
125.0	1.396	0.174	-0.174	190.0
130.0	1.484	0.087	-0.087	185.0
135.0	1.571	0.000	0.000	180.0
140.0	1.658	-0.087	0.087	175.0
145.0	1.745	-0.174	0.174	170.0
150.0	1.833	-0.259	0.259	165.0
155.0	1.920	-0.342	0.342	160.0
160.0	2.007	-0.423	0.423	155.0
165.0	2.094	-0.500	0.500	150.0

Load and Power Control of Horizontal Axis Wind Turbine

170.0	2.182	-0.574	0.574	145.0
175.0	2.269	-0.643	0.643	140.0
180.0	2.356	-0.707	0.707	135.0
185.0	2.443	-0.766	0.766	130.0
190.0	2.531	-0.819	0.819	125.0
195.0	2.618	-0.866	0.866	120.0
200.0	2.705	-0.906	0.906	115.0
210.0	2.880	-0.966	0.966	105.0
215.0	2.967	-0.985	0.985	100.0
220.0	3.054	-0.996	0.996	95.0
225.0	3.142	-1.000	1.000	90.0
230.0	3.229	-0.996	0.996	85.0
235.0	3.316	-0.985	0.985	80.0
240.0	3.403	-0.966	0.966	75.0
245.0	3.491	-0.940	0.940	70.0
250.0	3.578	-0.906	0.906	65.0
255.0	3.665	-0.866	0.866	60.0
260.0	3.752	-0.819	0.819	55.0
265.0	3.840	-0.766	0.766	50.0
270.0	3.927	-0.707	0.707	45.0
275.0	4.014	-0.643	0.643	40.0
280.0	4.102	-0.574	0.574	35.0
285.0	4.189	-0.500	0.500	30.0
290.0	4.276	-0.423	0.423	25.0
295.0	4.363	-0.342	0.342	20.0
300.0	4.451	-0.259	0.259	15.0
310.0	4.625	-0.087	0.087	5.0
315.0	4.712	0.000	0.000	0.0
320.0	4.800	0.087	-0.087	-5.0
325.0	4.887	0.174	-0.174	-10.0
330.0	4.974	0.259	-0.259	-15.0
335.0	5.061	0.342	-0.342	-20.0
340.0	5.149	0.423	-0.423	-25.0
345.0	5.236	0.500	-0.500	-30.0
350.0	5.323	0.574	-0.574	-35.0
355.0	5.411	0.643	-0.643	-40.0
360.0	5.498	0.707	-0.707	-45.0

Chapter 8 Conclusions

In this research, the load and performance of HAWT were estimated under extreme direction change wind, turbulence wind and yawed inflow wind conditions. In addition, the load was decreased by using the cyclic pitch control method. The above contents were carried out the wind tunnel experiment. The model wind turbines as two-bladed, three-bladed upwind and two-bladed downwind wind turbine were used in the experiment. The numerical analysis was also performed to compare with experimental data. FAST code and QBlade software were used to simulate the model wind turbine and turbulence intensity, respectively. There are some main conclusions as follows:

I. Turbulence and extreme direction change wind condition

- (1) The simulation results of Qblade software agree with measurement data. The turbulence level has significant impacts on wind turbine performance.
- (2) Wind direction change was generated by wind direction change equipment in wind tunnel illustrated a good agreement with “Extreme Direction Change (EDC)” of IEC standard.
- (3) For the yawing moment amplitude, the two-bladed wind turbine was higher about 39% than that of the three-bladed one. For three-bladed wind turbine, the fluctuation amplitude of the pitching moment has three periods during rotation for of the three-bladed wind turbine.
- (4) For the pitching moment magnitude with respect to the azimuth angle, the two-bladed wind turbine had two peaks at $\phi_{WDC} = 60^\circ$ and 200° . The three-bladed one was shown with the behavior of the three cycles. With respect to the averaged value of the pitching moment amplitude, there was no significant difference in the two-bladed and three-bladed wind turbines.

II. Front Inflow Wind Condition

- (1) The power coefficient obtained the maximum value at the optimum pitch angle. It decreases in both cases when the pitch angle changed out of the optimum pitch angle. It means that the power coefficient can be controlled by steady pitch control.
- (2) The thrust force acting on the rotor plane also can be controlled by steady pitch control. The magnitude of the thrust force increases when the pitch angle decrease and the tip speed ratio increase.
- (3) The power coefficient and the thrust coefficient at the cyclic pitch control slightly fluctuate as the change amplitude a increases and decreases due to phase ξ . Because the azimuth angle position at which the maximum pitch angle and the minimum pitch angle are reached by the cyclic pitch control differs according to the phase ξ and the inflow wind changes due to the tower wake.
- (4) The pitching moment and yawing moment linearly change with respect to the variation amplitude a in the cyclic pitch control. They are determined by two variables, the phase ξ and the change amplitude a . Therefore, the magnitude and direction of the moment generated on the rotor plane can be arbitrarily controlled by cyclic pitch control.

III. Yawed Inflow Wind

- (1) When the yaw angle increases, the change of the angle of attack becomes larger. In addition, as the absolute value of the change amplitude a increases, the change in the angle of attack becomes larger and departs from the optimum angle of attack at the yaw angle of $\varphi = 0^\circ$.
- (2) The value of the maximum power coefficient decreases as the yaw angle increases or decreases. However, the value of the tip speed ratio indicates the maximum power coefficient is constant regardless of the yaw angle change. The maximum power coefficient also changes depending on each phase angle as the pitch angle amplitude change.

- (3) The pitch angle phase can be arbitrarily set by the cyclic pitch control. The magnitude of the yawing moment coefficient can be adjusted by changing the pitch angle amplitude. Therefore, the yawing moment coefficient changes when modifying the azimuth angle position.
- (4) The cyclic pitch control is possibility of reducing the load fluctuation of the yaw system and reducing the load of the vibration acting on the wind turbine.

IV. Simulation Results

- (1) The power performance and thrust performance of the wind turbine simulated in the front inflow wind and yawed inflow wind condition. The analysis results showed the same trend as the experimental values.
- (2) The analysis code simulated the cyclic pitch control under the quasi-steady state. It can analyze the rotor aerodynamic load corresponding to various pitch control and the various yaw control.
- (3) Because the analysis result shows the same trend with the experimental values, the analysis conditions were not limited compared with the experiment. The analysis conditions can be assume wider range.

V. Future works

This thesis focused on load analysis of the upwind wind turbine on extreme direction change wind condition, effect of turbulence intensity on performance of wind turbine. In addition, the wind turbine control method decreased the load of floating offshore downwind wind turbine in the front inflow wind and the yawed inflow wind conditions was studied. Therefore, the complex wind conditions such as storms (strong waves and high turbulence wind) are not including in this study. These conditions generate maximum and higher load on the wind turbine. Furthermore, they are also effect strongly on the performance and lifetime of wind turbine. Hence, my future works are estimating that effects on load, the performance of wind turbine and study control methods to protect wind turbine in the complex wind condition.

Acknowledgments

Over these years in Mie University, Japan, it has been my good fortune to encounter some people who have given me more of their time, professional and personal help, and above all companionship and true friendship.

From the beginning of my studies, I already knew that I wanted to do a PhD, therefore I wish to particularly acknowledge people who trusted me and gave me the opportunity to do so. Without whom I certainly would not be writing this thesis:

My deepest gratitude goes to my Professor Takao MAEDA, my supervisor, who strongly helped me during my research, who always gave useful advice and expert guidance and who spent much time reading and giving highly valuable comments for my thesis. I have been lucky to have you as my advisor and I consider it an honor working with you. I would like to express my heartfelt thanks to Associate Professor Yasunari KAMADA for invaluable guidance and advices during my experiments. I also would like to thank my Assistant Professor Dr. Junsuke MURATA and Dr. Qingan Li who always provides valuable assistance.

I also would like to thank Prof. Masafumi HIROTA and Prof. Koichi TSUJIMOTO for their kind review of my thesis.

I am very grateful to my group members in the Fluid Engineering Laboratory for Energy and Environment: Yuta OKUMURA, Masahiro MORIMOTO, Atsushi FUJIWARA, Kenshirou MATSUOKA and Shingo KITAGAWA for your helpful assistance during the experiment, for their hospitality, sharing their knowledge and for offering fruitful suggestions. In addition, our secretary, Tomoko TERAGAWA is thanked for her practical assistance about procedures of Mie University and Mie province, which saved me lots of time and many comfortable in my daily life.

I would like to give a thank you to Professor Toru NAGAO who gave me a chance to research in Mie University through Researcher Invitation program.

Most of all, I would like to express to gratitude to my wife and family for their support. Without their patience and encouragement, completion would have never been reached.

Thank you for all you have done for me. I will never forget those who helped me.

Le Quang SANG
March 2018

References

- [1] Sathyajith Mathew, Wind Energy: Fundamentals, Resource Analysis and Economics, Springer-Verlag Berlin Heidelberg (2006).
- [2] Thomas Ackermann, Wind Power in Power Systems, John Wiley & Sons, Ltd (2005).
- [3] Putnam PC, Power from the wind. Van Nostrand, New York (1948).
- [4] Ramler JR, Donovan RM, Wind turbines for electric utilities: Development status and economics. DOE/NASA/1028-79/23, NASA TM-79170, AIAA-79-0965 (1979).
- [5] American Wind Energy Association (AWEA), AWEA U.S. Wind Industry Annual Market Report Year Ending 2016 (Washington, DC: April 2017)
- [6] Canadian Wind Energy Association (CanWEA), “Installed capacity”, <http://canwea.ca/wind-energy/installed-capacity/>, Accessed 2017. 08. 18.
- [7] CanWEA, “Wind energy in Canada”, <http://canwea.ca/windenergy/installed-capacity/>, Accessed 2017. 08. 18.
- [8] WindEurope, Shares of onshore and offshore based on data from GWEC.
- [9] Bundesministerium für Wirtschaft und Energie (BMWi), Zeitreihen zur Entwicklung der erneuerbaren Energien in Deutschland, unter Verwendung von Daten der Arbeitsgruppe Erneuerbare Energien-Statistik (AGEE-Stat) (Stand: Februar 2017), p. 7, <http://www.erneuerbare-energien.de/EE/Redaktion/DE/Downloads/zeitreihen-zur-entwicklung-der-erneuerbarenenergien-in-deutschland-1990-2016.pdf>, Accessed 2017. 08. 18.
- [10] New markets from Steve Sawyer, cited in GWEC, “Wind power chalks up more strong numbers”, press release (Brussels: 10 February 2017)
- [11] GWEC, op. cit. note 1
- [12] REN21, 21 March 2017;
- [13] Government of India, Ministry of Power, Central Electricity Authority, All India Installed Capacity, Monthly Report January 2017 http://www.cea.nic.in/reports/monthly/installedcapacity/2017/installed_capacity-01.pdf, Accessed 2017. 08. 18.
- [14] Financial close for Indonesia’s first utility-scale wind project”, Windpower Monthly, 7 February 2017, <http://www.windpowermonthly.com/article/1423494/financial-closeindonesias-first-utility-scale-wind-project>, Accessed 2017. 08. 18.
- [15] VN green energy gets strong tail wind”, Vietnam Net, 3 December 2016, <http://english.vietnamnet.vn/fms/science-it/167956/vn-green-energygets-strong-tail-wind.html>, Accessed 2017. 08. 18.
- [16] The European Offshore Wind Industry - Key Trends and Statistics 2016, Brussels, January 2017,
- [17] Deutsche WindGuard, Status of Offshore Wind Energy Development in Germany 2016.
- [18] William Steel, “First commercial power achieved from MHI Vestas’ Mammoth 8-MW Turbines”, Renewable Energy World, 20 December 2016, <http://www.renewableenergyworld.com/articles/2016/12/first-commercial-power-achievedfrom-mhi-vestas-mammoth-8-mw-turbines.html>,
- [19] MHI Vestas Offshore Wind, “World’s most powerful wind turbine once again smashes 24 hour power generation record as 9 MW wind turbine is launched”, <http://www.mhivestasoffshore.com/new-24-hour-record/>,
- [20] METI/ANRE, report of the survey of wind energy potentials (FY 2010 basic survey project for accelerating new energy deployment), http://www.meti.go.jp/meti_lib/report/2011fy/E001771.pdf,
- [21] Institute for Sustainable Energy Policies, Renewables 2016 Japan Status Report, Summary, 2016.
- [22] Japan Wind Power Association (JWPA), Offshore Wind Power Development in Japan, 2017.
- [23] Boukhezzar, B.; Houria, S. Nonlinear control with wind estimation of a DFIG variable speed wind turbine for power capture optimization. Energy Convers. Manag. Vol50, pp.885–892, 2009.
- [24] Munteanu I., Cutululis N. A., Bratcu A. I., Ceanga E., Optimization of variable speed wind power systems based on a LQG approach, Control Eng. Pract., Vol. 13, No. 7, pp. 903-912, 2005.
- [25] Muljadi E., Butterfield C.P., Pitch-controlled variable-speed wind turbine generation, IEEE Transactions on Industry Applications; 37: 240–246, 2001.
- [26] Bossanyi E A, Fleming P A and Wright A D. Validation of individual pitch control by field tests on two- and three-bladed wind turbines., IEEE Transactions on Control Systems Technology; 21: 1067–1078, 2013.
- [27] Bottasso C L, Croce A, Riboldi C E D and Salvetti M. Cyclic pitch control for the reduction of ultimate loads on wind turbines. Journal of Physics; 524 012063, 2014.

- [28] Houtzager I, van Wingerden J W, Verhaegen M. Wind turbine load reduction by rejecting the periodic load disturbances. *Wind Energy*; 16(2): 235–256, 2013.
- [29] Menon M and Fernando L P. Dynamic aeroelastic behavior of wind turbine rotors in rapid pitch control actions. *Renewable Energy* 2017, 107: 327-339
- [30] Van Solingen E, Fleming PA, Scholbrock A and van Wingerden J W. Field testing of linear individual pitch control on the two-bladed controls advanced research turbine. *Wind Energy*. 2016; 19:421-436.
- [31] Velte C M, Mikkelsen R, Sørensen J N, Kaloyanov T and Gaunaa M. Closed loop control of a flap exposed to harmonic aerodynamic actuation. *Proceedings of Torque 2012: The science of making torque from wind*, Oldenburg, Germany. 2012.
- [32] Bottasso C L, Croce A, Gualdoni F and Montinari P. Load mitigation for wind turbines by a passive aeroelastic device. *J. Wind Eng. Industrial Aerodynamics*. 2016, 148: 57-69.
- [33] Bossanyi E A. Wind turbine control for load reduction. *Wind Energy*. 2003b; 6:229–244.
- [34] Bossanyi E A. Further load reduction with Individual pitch control. *Wind Energy*. 2005; 8:481–485.
- [35] Bossanyi E A. Individual blade pitch control for load reduction, *Wind Energy*. 2003a; 6:119-128
- [36] Stol K A. Disturbance tracking control and blade load mitigation for variable-speed wind turbines *ASME J. of Sol. Energy Eng*. 2003; 125: 396-401.
- [37] Geyler M and Caselitz P. Robust multivariable pitch control design for load reduction on large wind turbines *ASME J. of Sol. Energy Eng*. 2008; 130: 031014/1–031014/12.
- [38] Bottasso C L, Croce A, Riboldi C E D and Nam Y. Multi-layer control architecture for the reduction of deterministic and non-deterministic loads on wind turbines. *Renew Energy*. 2013; 51: 159-169.
- [39] Larsen T J, Madsen H A, Thomsen K. Active load reduction using individual pitch, based on local blade flow measurements. *Wind Energy*. Vol 8: pp. 67-80, 2005.
- [40] Imran, Raja M., Akbar Hussain D. M., and Mohsen Soltani. "DAC with LQR control design for pitch regulated variable speed wind turbine." *Telecommunications Energy Conference (INTELEC)*, 2014 IEEE 36th International. IEEE, 2014.
- [41] Manwell, James F., Jon G. McGowan, and Anthony L. Rogers. *Wind energy explained: theory, design and application*. John Wiley Sons, 2010.
- [42] Burton, Tony, et al. *Wind energy handbook*. John Wiley Sons, 2001.
- [43] Matha, Denis. *Model Development and Loads Analysis of an Offshore Wind Turbine on a Tension Leg Platform with a Comparison to Other Floating Turbine Concepts*: April 2009. No. NREL/SR-500-45891. National Renewable Energy Laboratory (NREL), Golden, CO., 2010.
- [44] Geyler M. and Caselitz P., Individual blade pitch control design for load reduction on large wind turbines, *Proc. European Wind Energy Conf. (Milano)*, 2007.
- [45] van Engelen T. G. and Kanev S., Exploring the limits in individual pitch control, *Proc. European Wind Energy Conf. (Marseille)*, 2009.
- [46] Stol K. A., Disturbance tracking control and blade load mitigation for variable-speed wind turbines *ASME J. of Sol. Energy Eng*. 125, 396-401, 2003.
- [47] David Marten, *QBlade Guidelines: v0.6 and QBlade Short Manual: v0.8*, 2014.
- [48] Jason M, Jonkman, Marshall L. Buhl Jr, *FAST User's Guide*, 2005.
- [49] Jonkman B.J., Kilcher L., *TurbSim User's Guide: Version 1.06.00*, 2012.
- [50] Glauert, H. 1935. *Airplane Propellers*. *Aerodynamic Theory* (W. F. Durand, ed.), Div. L, Chapter XI. Berlin:Springer Verlag.
- [51] Viterna, L .A., and Janetzke, D. C., "Theoretical and Experimental Power from Large Horizontal-Axis Wind Turbines," *NASA TM-82944*, Sept 1982.